Bifurcations and strange attractors in the Lorenz-84 climate model with seasonal forcing

Broer, H; Simo, C; Vitolo, R

Published in:
Nonlinearity

Publication date:
2002

INSTITUTE OF PHYSICS PUBLISHING NONLINEARITY

Nonlinearity **15** (2002) 1205–1267 PII: S0951-7715(02)29803-5

Bifurcations and strange attractors in the Lorenz-84 climate model with seasonal forcing

Henk Broer[1], **Carles Simó**[2] **and Renato Vitolo**[1]

[1] Department of Mathematics, University of Groningen, PO Box 800, 9700 AV Groningen, The Netherlands
[2] Departament de Matemàtica Aplicada i Anàlisi, Universitat de Barcelona, Gran Via 585, 08007 Barcelona, Spain

Received 17 October 2001
Published 5 June 2002
Online at stacks.iop.org/Non/15/1205

Recommended by M Viana

Abstract

A low-dimensional model of general circulation of the atmosphere is investigated. The differential equations are subject to periodic forcing, where the period is one year. A three-dimensional Poincaré mapping $\mathcal{P}$ depends on three control parameters F, G, and ϵ, the latter being the relative amplitude of the oscillating part of the forcing. This paper provides a coherent inventory of the phenomenology of $\mathcal{P}_{F,G,\epsilon}$. For ϵ small, a Hopf-saddle-node bifurcation $\mathcal{HSN}$ of fixed points and quasi-periodic Hopf bifurcations of invariant circles occur, persisting from the autonomous case $\epsilon = 0$. For $\epsilon = 0.5$, the above bifurcations have disappeared. Different types of strange attractors are found in four regions (chaotic ranges) in $\{F, G\}$ and the related routes to chaos are discussed.

Mathematics Subject Classification: 37D45, 37G35

1. Introduction

1.1. The driven Lorenz-84 system

Weather and climate prediction are difficult tasks, because of the complexity of the atmospheric evolution. Nowadays computer models used for these predictions usually contain a high number of variables and parameters. Therefore, it is practically impossible to perform detailed studies of their dynamical properties. On the other hand, there is experimental evidence [61] that low-dimensional attractors appear in some hydrodynamical flows just after the onset of turbulence. As a consequence, low-dimensional models have attracted the attention of meteorologists, mathematicians and physicists over the last decades. These models are easier to study than the infinite-dimensional Navier–Stokes equations, or than large computer models.

In particular, geometrical, and qualitative methods from bifurcation theory [5, 34, 40] can be applied to clarify the transitions from regular to complicated dynamical behaviour.

In this paper, we examine a model for the long-term atmospheric circulation, proposed by Lorenz [41] in 1984, obtained by a Galerkin projection of an infinite-dimensional model. This is a three-dimensional system given by

$$\begin{aligned} \dot{x} &= -ax - y^2 - z^2 + aF, \\ \dot{y} &= -y + xy - bxz + G, \\ \dot{z} &= -z + bxy + xz, \end{aligned} \tag{1}$$

where the dot represents differentiation with respect to the time t. System (1) has been used in climatological studies, for example by coupling it with a low-dimensional model for ocean dynamics. For related work, see [63] and references therein. On the other hand, the bifurcation diagram of (1) has been analysed in [55]. For other dynamical studies of this system, that we shall refer to as *(autonomous) Lorenz-84*, see [36, 43].

We briefly summarize the meaning of variables, parameters and constants in Lorenz-84. The time unit of t is estimated to be five days. The variable x stands for the strength of the symmetric, globally averaged westerly wind current. The variables y and z are the strength of cosine and sine phases of a chain of superposed waves transporting heat poleward. The terms in b represent displacement of the waves due to interaction with the westerly wind. The coefficient a, if less than 1, allows the westerly wind current to damp less rapidly than the waves. The terms in F and G are thermal forcings: F represents the *symmetric* cross-latitude heating contrast and G accounts for the *asymmetric* heating contrast between oceans and continents. In a later paper [42], Lorenz pointed out that F and G should be allowed to vary periodically during a year. In particular, F should be larger in winter than in summer. However, in his numerical study he kept G fixed, identifying $(F, G) = (6, 1)$, and $(F, G) = (8, 1)$, with summer, respectively winter, conditions. He introduced a periodical variation of the parameter F between summer and winter conditions, by putting $F = 7 + 2\cos(2\pi t/T)$ with T of the order of magnitude of 1 yr, i.e. $T = 73$.

We use a slightly different approach, in order to study seasonal effects. Here F and G are both taken T periodic in time, by using

$$F(1 + \epsilon\cos\omega t) \quad \text{and} \quad G(1 + \epsilon\cos\omega t), \qquad \omega = \frac{2\pi}{T}.$$

Lorenz-84 thereby turns into a parametrically forced system:

$$\begin{aligned} \dot{x} &= -ax - y^2 - z^2 + aF(1 + \epsilon\cos(\omega t)), \\ \dot{y} &= -y + xy - bxz + G(1 + \epsilon\cos(\omega t)), \\ \dot{z} &= -z + bxy + xz. \end{aligned} \tag{2}$$

We refer to this three-dimensional T-periodic model as the *driven Lorenz-84*. As in [36, 41–43, 55], the parameters a and b from now on are set to $a = 1/4$ and $b = 4$, while T is fixed at 73. The value of ϵ used in most of the numerical simulations is 0.5. However, smaller values will be used when investigating the relation between the dynamics of systems (2) and (1). For this reason ϵ is used as a control parameter together with F and G. We indicate the three-dimensional parameter space by $\mathfrak{M} = \{F, G, \epsilon\}$. Fixing a value $\epsilon = \epsilon^*$ means selecting a plane $\mathfrak{M}_{\epsilon^*} = \{F, G\}$ inside $\mathfrak{M}$. Only positive values of G have to be considered, since solutions of (2) for $G = -G_0$ correspond to solutions for $G = G_0$ by changing the sign of y and z. For numerical experiments, we mainly focus on the parameter window

$$(F, G, \epsilon) \in [0, 12] \times [0, 9] \times [0, 0.5],$$

for which (F, G) are centred around summer and winter conditions. However, we will also be concerned with asymptotical properties of (2) for $G \to 0$ and $G \to \infty$. The driven system

will be studied in terms of its Poincaré map[3]

$$\mathcal{P}_{F,G,\epsilon} : \mathbb{R}^3 \to \mathbb{R}^3$$

which is a diffeomorphism depending on the parameters[4] (F, G, ϵ).

Remark 1.1. By 'periodic point' we mean a point $q \in \mathbb{R}^3$ such that $\mathcal{P}^m(q) = q$ for some integer $m \neq 0$. A period m point and an invariant circle of $\mathcal{P}$ correspond to a period $|m|T$ limit cycle, respectively an invariant two-torus, of the flow of (2), see table 2 in section 3.

The dynamics of the family $\mathcal{P}_{F,G,\epsilon}$ is first explored by iteration to an attractor for several values of (F, G), for $\epsilon = 0.5$ fixed. In fact, $\mathcal{P}$ has an attracting bounded subset of $\mathbb{R}^3$ for all values of F, G, and ϵ (see section 2.1). The map $\mathcal{P}$ is computed by numerical integration of equation (2) along a period T. The unusual length of the period causes $\mathcal{P}$ to be quite sensitive to initial conditions. To achieve enough numerical precision we chose a method of integration based on the Taylor expansion of the solution (see appendix A.1). Some preliminary results are examined in the next section.

1.2. Overview of the attractors of $\mathcal{P}_{F,G,\epsilon}$ for $\epsilon = 0.5$

In figure 1 we plotted one-dimensional projections of sequences of attractors of $\mathcal{P}$. In each bifurcation diagram, G varies in a grid with spacing 0.01 on the line $F = F_0$, where F_0 is kept fixed. For each G on the grid, the y-projection of one attractor is plotted. We achieved a sort of continuity in the evolution of the attractors by using the following algorithm. Values $F = F_0$ and $G = 0$ are fixed initially. Starting from the point $q = (x, y, z) = (1, 2, 3)$, a loop of 2000 iterations of $\mathcal{P}_{F_0,0}$ is carried out, of which the last 100 points are plotted. Then the parameter G is increased by 0.01 and the last point is used to start a new loop. Note that no coexistence of attractors (multistability) can be detected in this way.

The attractors plotted in figure 1 belong to three classes: fixed (or periodic) points, invariant circles and strange attractors (SA) [46, 48, 52, 53]. A fixed point $\mathbb{A}$ is the unique attractor occurring for small F, compare figures 1(a) and (b). As G increases, its y-coordinate evolves continuously in the first case and has a jump at $G \simeq 0.5$ in the second. The fixed point $\mathbb{A}$ is also detected for all G larger than a value $G_{\mathbb{A}}$ depending on F. In figures 1(c)–(f) one has respectively[5] $G_{\mathbb{A}} \simeq 0.84, 1.48, 3.9, 7.54$.

At $F = 1.2$ (figure 1(c)) an invariant circle $\mathbb{C}_1$ occurs for G small, instead of $\mathbb{A}$. In the G-interval (0.34, 0.37), pointed by a solid arrow, $\mathbb{C}_1$ is phase-locked to a fixed point attractor[6]. The circle shrinks down as G increases and at $G \simeq 0.78$ (marked by a dashed arrow) the fixed point $\mathbb{A}$ reappears. For G larger, the evolution of $\mathbb{A}$ is similar to figure 1(b): a discontinuity occurs at $G \simeq 0.84$, but $\mathbb{A}$ persists for all larger G.

The circle attractor $\mathbb{C}_1$ also exists for $F = 5$, 7, and 11, for G smaller than a threshold $G_{\mathbb{C}}$ depending on F. One has respectively $G_{\mathbb{C}} \simeq 0.64$, 0.33, and 0.48, marked by arrows in figures 1(d)–(f). A 'doubled' circle $2\mathbb{C}_1$ occurs for $F = 7$ and $0.34 \lessapprox G \lessapprox 0.5$ (see section 4.9.1). A strange attractor is found for most G values in the intervals $0.65 \lessapprox G \lessapprox 1.29$, $0.59 \lessapprox G \lessapprox 1.7$ and $0.5 \lessapprox G \lessapprox 2.04$ respectively, but for G larger the fixed point $\mathbb{A}$ reappears. For $F = 7$ and $F = 11$, $\mathbb{A}$ is again replaced by a circle attractor $\mathbb{C}_2$ in the intervals $2.15 \lessapprox G \lessapprox 3.89$ and $2.36 \lessapprox G \lessapprox 7.53$, respectively. This corresponds to the 'cigar'-like sequences $\mathbb{C}_2(7, G)$ in figure 1(e) and $\mathbb{C}_2(11, G)$ in (f).

[3] Also called stroboscopic, first return or period mapping.
[4] We often suppress some or all parameters in the notation, writing $\mathcal{P}_{F,G}$ or $\mathcal{P}$
[5] When giving approximate numerical values we shall use the symbols $\lessapprox$, $\gtrapprox$, and $\simeq$ instead of $<$, $>$, and $=$.
[6] This corresponds to an Arnol'd tongue $\mathfrak{A}_1$ of rotation number zero [3, 25, 52].

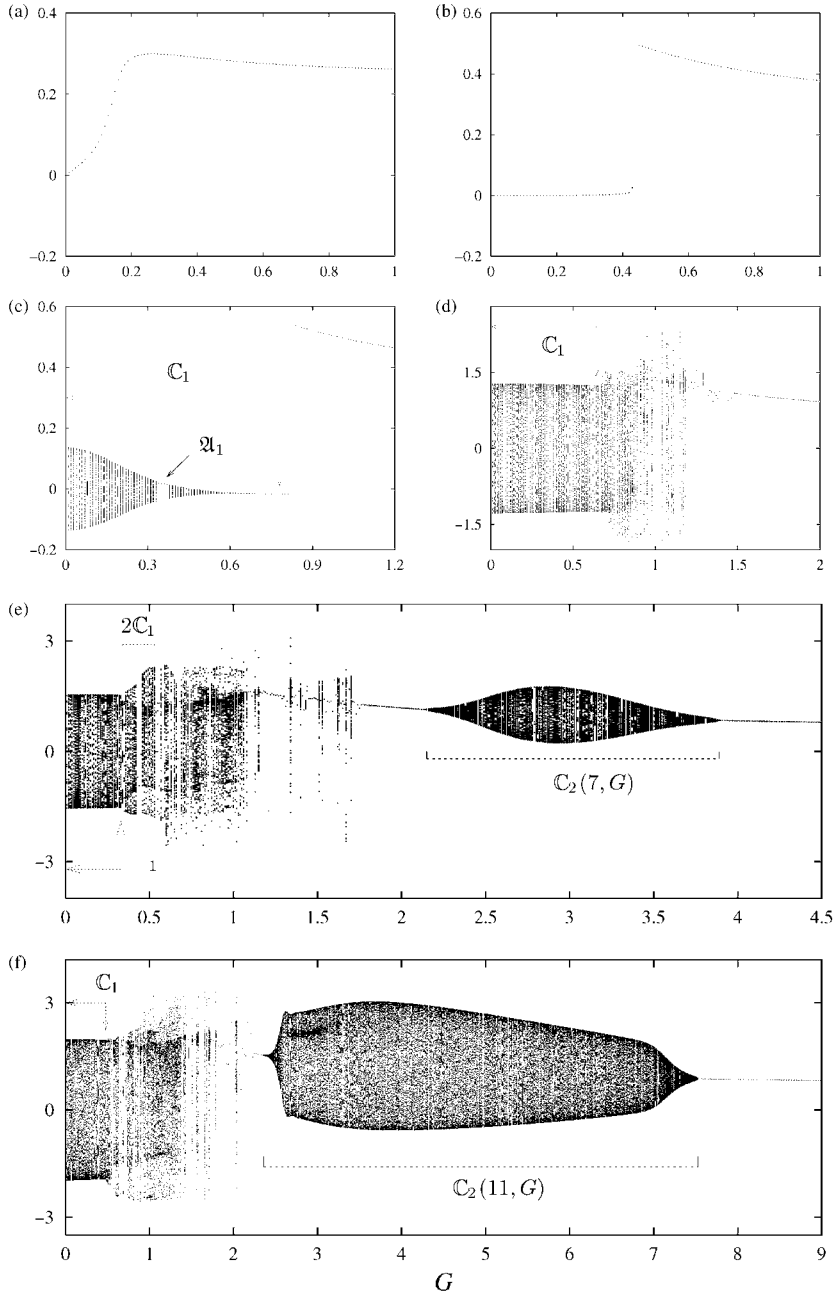

Figure 1. Projections on y of sequences of $\mathcal{P}$-attractors as a function of G, for $\epsilon = 0.5$. In each picture F is fixed: (*a*) $F = 0.2$, (*b*) $F = 0.7$, (*c*) $F = 1.2$, (*d*) $F = 5$, (*e*) $F = 7$, (*f*) $F = 11$. Only the last 100 points of each iteration loop are plotted (see text for explanation).

Several transitions of the attractors are detected by this procedure. Then the following questions arise: what is the exact subdivision of the parameter plane $\mathfrak{M}_{0.5}$? Can we characterize the transitions in terms of bifurcations? Which bifurcations lead to strange attractors? What are the dynamical properties of these SAs and the implications for the (un)predictability of the

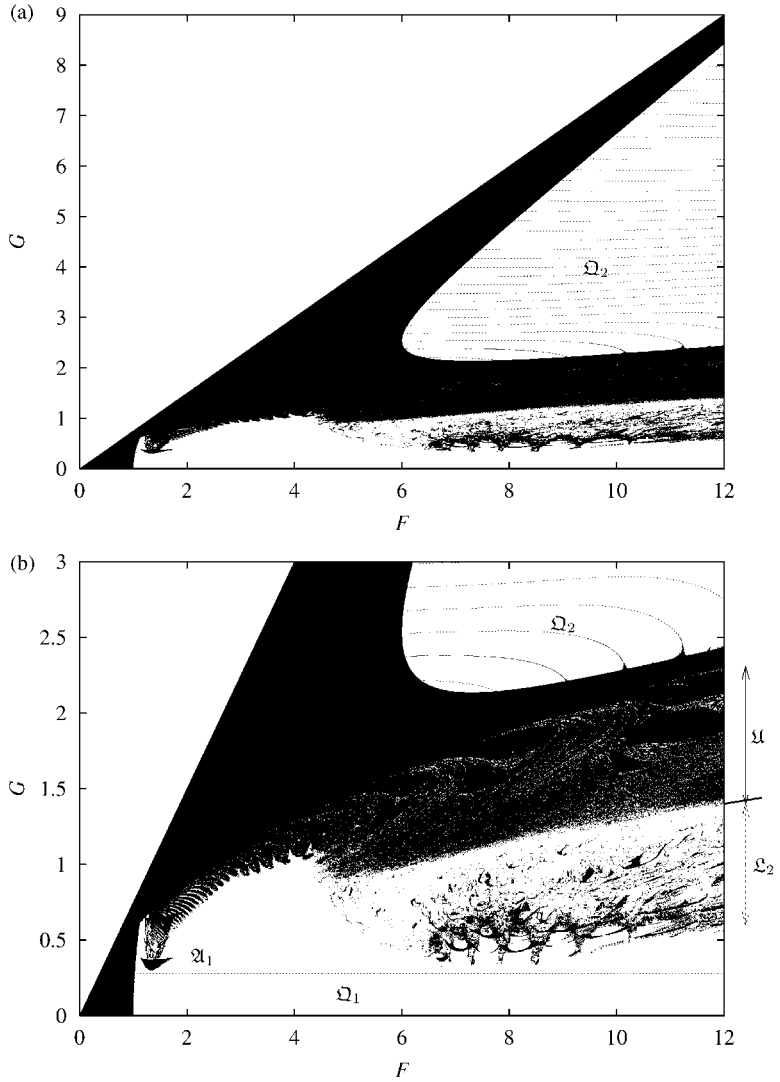

Figure 2. (*a*) Points in the parameter plane $\mathfrak{M}_{0.5}$ with a fixed or periodic point attractor are indicated by a black dot. (*b*) Magnification of part of figure 2(*a*). The dashed line $G = 0.28$ bounds strip $\mathfrak{Q}_1$. Two chaotic ranges $\mathfrak{L}_2$ and $\mathfrak{U}$ are labelled at the margin of figure 2(*b*), see text for explanation.

driven model? This paper is intended to provide a coherent inventory of the phenomenology and to give an answer, whenever possible, to the above questions.

1.3. Setting of the problem and sketch of results

A first sketch of the organization of $\mathfrak{M}_{0.5}$ again is obtained by brute force iteration. In figure 2 we plotted a black dot for all (F, G)-values such that a fixed or periodic point attractor occurs[7]. Therefore, white spots correspond either to a quasi-periodic invariant circle or to a SA. A grid with spacing $1/200$ is fixed inside $\mathfrak{M}_{0.5}$. For all (F, G) on the grid, N iterations of the map

[7] To simplify the picture, no dots are plotted above the straight line $G = 3/4\,F$.

$\mathcal{P}$ are computed, starting each time from the point $q = (x, y, z) = (1, 2, 3)$. The condition checked in the algorithm for a period k point is that the maximum of

$$\mathrm{dist}(\mathcal{P}^n(q), \mathcal{P}^{n-k}(q)), \quad \mathrm{dist}(\mathcal{P}^n(q), \mathcal{P}^{n-2k}(q)), \quad \mathrm{dist}(\mathcal{P}^n(q), \mathcal{P}^{n-3k}(q))$$

be less than 10^{-12}. Usually, N is set to 200, but for a few parameter values it was necessary to take up to $N = 10^5$ iterates to get convergence.

It turns out that a fixed point $\mathbb{A}$ is the unique attractor for G large (see section 2.2 for a proof). A circle attractor $\mathbb{C}_2$ exists in region $\mathfrak{Q}_2$. The cigar-like sequences of attractors $\mathbb{C}_2(7, G)$ and $\mathbb{C}_2(11, G)$ in figures 1(*e*) and (*f*) correspond to sections of $\mathfrak{Q}_2$ by a vertical line $F = 7$ and $F = 11$, respectively. The dashed lines in figure 2 are Arnol'd tongues with zero rotation number. These tongues are rather narrow and open up only at the lower boundary of $\mathfrak{Q}_2$, at some small black spikes visible in figure 2(*b*) (see section 4.1). Quasi-periodicity appears thus to be prevalent in $\mathfrak{Q}_2$, in the sense that it occurs with large relative measure in the parameter space (see, e.g. [48]). A circle attractor $\mathbb{C}_1$ occurs for $F > 1$ and G smaller than a certain value $G_{\mathbb{C}}(F)$, compare again figures 1(*c*)–(*f*). We guess that $\mathbb{C}_1$ persists for all parameter values inside the strip $\mathfrak{Q}_1$ in figure 2(*b*), bounded above by the line $G = 0.28$. As G increases, $\mathbb{C}_1$ may undergo different fates, depending on the value of F. For $1.25 \lessapprox F \lessapprox 1.7$, $\mathbb{C}_1$ crosses a period-one Arnol'd tongue $\mathfrak{A}_1$ (cf figure 2(*b*)) and then breaks (section 4.8). Indeed, a chaotic range $\mathfrak{L}_1$ occurs just above $\mathfrak{A}_1$ (figure 5). Several windows of periodicity occur and outside them, SA's occur like in figure 6(*B*).

For $F \gtrsim 5$, there is a different, wide region inside $\mathfrak{M}_{0.5}$ where SAs are found. In figure 2(*b*) one can see that this chaotic range becomes wider as F increases and is roughly divided into two parts, labelled by $\mathfrak{U}$ and $\mathfrak{L}_2$. In the latter, SAs are prevalent: periodic points occur only in small windows. Inside $\mathfrak{U}$, fixed point attractors seem to be prevalent, (cf the large wave-like black regions in figure 2(*b*)) and SAs now and then appear (also see figure 12). Region $\mathfrak{Q}_2$ is separated from $\mathfrak{U}$ by a thin solid black strip where a unique fixed point attractor is detected.

Most of the above transitions of the attractors are explained by bifurcation theory (see [23, 34, 40, 52] for a general presentation). The simplest bifurcation of $\mathcal{P}_{F,G}$ is the loss of stability of a fixed point when one of the eigenvalues of $D\mathcal{P}_{F,G}$ crosses the unit circle. To this group belong the saddle-node, period doubling and the Hopf bifurcation [25, 46], all of which are found in the family $\mathcal{P}_{F,G}$. A framework of bifurcation curves of fixed points is shown in figure 3 and figure 5 (left). Saddle-node bifurcations occur on the curves $\mathcal{SN}_0$, $\mathcal{SN}_0^{\mathrm{sub}}$, and $\mathcal{SN}_1$. The two branches $\mathcal{SN}_0$ and $\mathcal{SN}_1$ of supercritical saddle-node bifurcations meet tangentially at a cusp $\mathcal{C}$. The Arnol'd tongue $\mathfrak{A}_1$ is bounded by two curves of supercritical saddle-node bifurcations.

Supercritical Hopf bifurcations of fixed points[8] occur on curves $\mathcal{H}_1$, $\mathcal{H}_1^{\mathrm{sub}}$, and $\mathcal{H}_2$. The attracting invariant circle $\mathbb{C}_1$ is born from the attracting fixed point $\mathbb{A}$ as (F, G) cross $\mathcal{H}_1$ from left to right. This explains the change from the fixed point $\mathbb{A}$ in figure 1(*b*) to the circle $\mathbb{C}_1$ in figure 1(*c*). So the curve $\mathcal{H}_1$ is the boundary at the left of strip $\mathfrak{Q}_1$ in figure 2(*b*). Similarly, the circle attractor $\mathbb{C}_2$ is born from the attracting fixed point $\mathbb{A}$ for (F, G) crossing $\mathcal{H}_2$ and entering region $\mathfrak{Q}_2$. A good part of the phenomena in figures 1 and 2 can be explained by the previous results. This yields a subdivision of the parameter plane in regions with the same dynamics, figure 4. There we also sketch the four chaotic ranges $\mathfrak{L}_1$, $\mathfrak{L}_2$, $\mathfrak{U}$, $\mathfrak{U}'$ (see below). The dashed curves $\mathcal{B}$ and $\mathcal{SH}$, as well as the boundary of $\mathfrak{L}_1$, are not bifurcation curves of $\mathcal{P}_{F,G}$. $\mathcal{B}$ roughly indicates the breakdown of the circle $\mathbb{C}_1$ and $\mathcal{SH}$ denotes the boundary between $\mathfrak{L}_2$ and $\mathfrak{U}$. For details, see sections 4 and 5.

[8] We recall that a Hopf bifurcation [25] of a fixed point of $\mathcal{P}$ corresponds to a Naimark–Sacker [34, 40] bifurcation of a limit cycle of the flow of system (2).

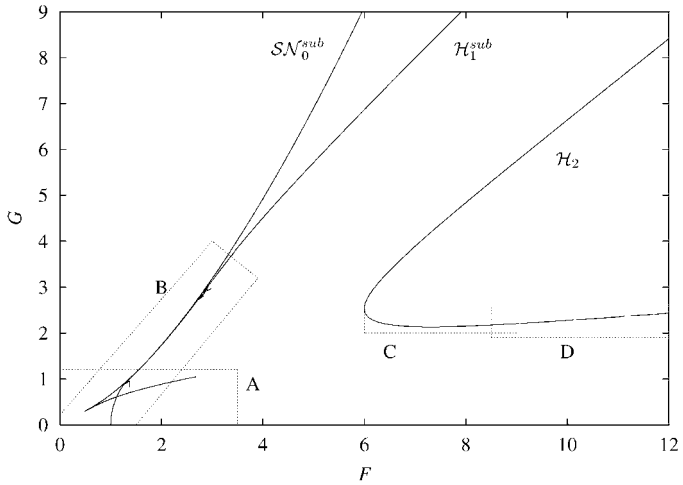

Figure 3. Bifurcation diagram of fixed points of the map $\mathcal{P}_{F,G}$ for $\epsilon = 0.5$. Boxes labelled by A, B, C, D are enlarged, respectively in figure 5 (left), figure 18, figures 22(*a*) and (*b*).

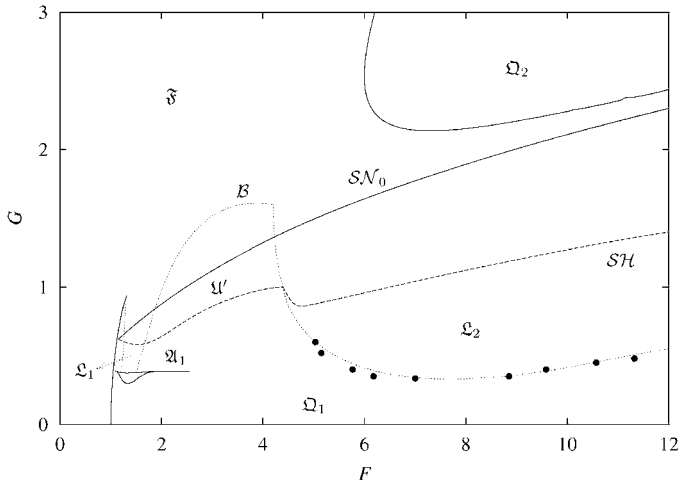

Figure 4. Sketch of the regions with same kind of dynamics in the window $[0, 12] \times [0, 3]$ in the parameter plane $\mathfrak{M}_{0.5}$. Thick dots indicate the occurrence of a quasi-periodic period doubling, where a doubled circle attractor $2\mathbb{C}_1$ appears (see section 4.9.1).

One of the main points of interest is the relation between the dynamics of systems (1) and (2). This is at first analysed as a perturbation problem from $\epsilon = 0$ (see section 3). Assuming that both the perturbative *ansatz* [4, 34] and genericity [52] hold, bifurcations of the autonomous system persist inside $\mathfrak{M}_\epsilon$, at least for ϵ small enough. It turns out that the bifurcations sketched in figure 3 for $\epsilon = 0.5$ are indeed 'inherited' from the autonomous system $\epsilon = 0$. Moreover, other bifurcations are found to persist for $\epsilon = 0.01$ (sections 3.2.1 and 3.2.2). An important case is a codimension two Hopf-saddle-node bifurcation of fixed point, which is an organizing centre of the bifurcation diagram of the autonomous case [55].

However, in spite of all similarities, even for ϵ positive and small the planes $\mathfrak{M}_\epsilon$ and $\mathfrak{M}_0$ present a number of differences. Arnol'd resonance tongues [3, 5, 16], attached to curves of

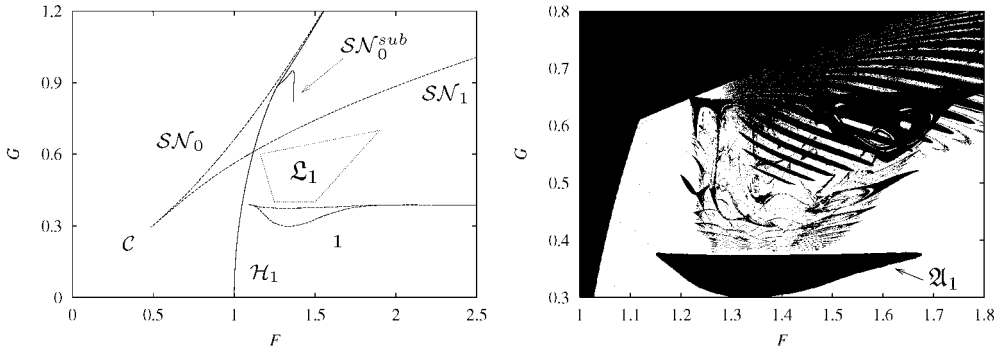

Figure 5. Left: magnification of box A in figure 3. The cusp $\mathcal{C}$ terminates two curves of saddle-node bifurcations. Right: magnification of a part of figure 2. The grid on the right figure is 10^{-3} in both F and G.

Hopf bifurcations, appear in $\mathfrak{M}_\epsilon$ (this is the case of $\mathfrak{A}_1$, figure 5). Homoclinic connections[9] of the flow of system (1) generically are broken and replaced by homoclinic intersections and bifurcations for the map $\mathcal{P}$ (see section 3.2.1). In this sense, $\epsilon = 0$ already is a bifurcation value[10]. Apart from this, codimension three bifurcations may occur in the parameter space $\mathfrak{M}$, changing the global organization of $\mathfrak{M}_\epsilon$. Indeed, a codimension three bifurcation causes the disappearance of the Hopf-saddle-node point at ϵ smaller than 0.5. These differences between $\mathfrak{M}_{0.5}$ and $\mathfrak{M}_0$ are further discussed in sections 4 and 5.1.3.

It is of special interest to determine which routes lead from simple to complicated dynamical behaviour, both for ϵ fixed or not. Two scenarios for the birth of SAs are theoretically understood: cascades of period doubling bifurcations [16,25,28,52] and homoclinic tangency bifurcations [16, 48, 52]. The former is a gradual process where the complexity of the attractor increases stepwise as the parameter varies. Well-known model maps displaying SAs originating from cascades of period doubling are the logistic [25,28] and the Hénon map [6,56]. On the other hand, homoclinic bifurcations may lead to a SA *at once*. Unfoldings of homoclinic tangencies for one-parameter families of diffeomorphisms generically yield a large variety of dynamical phenomena. Hénon-like SAs or repellors occur with positive Lebesgue measure in the parameter space [26, 44, 64] (we recall that Hénon-like SAs coincide with the closure of the unstable manifold of some hyperbolic saddle point and their dimension is usually not much larger than one). Close to a homoclinic tangency, cascades of homoclinic tangencies accumulate, as well as cascades of period doubling bifurcations of periodic attractors [68]. Infinitely many periodic attractors can coexist close to a diffeomorphism with a homoclinic tangency, this is the Newhouse phenomenon [45, 49].

Several other phenomena are found close to homoclinic tangencies in concrete models. Cascades of cusps and accumulation of Arnol'd tongues on curves of homoclinic bifurcations have been reported in [16]. There it was conjectured that accumulation of Arnol'd tongues might be a mechanism for the creation of infinitely many sinks in the Newhouse phenomenon.

The basic dynamical property of a SA is the sensitive dependence with respect to initial conditions. Computation of the spectrum of the Lyapunov exponents [7] is one of the standard ways to detect chaotic behaviour, since a positive Lyapunov exponent implies sensitivity with respect to initial conditions [27,52,56,61]. Moreover, knowledge of the Lyapunov spectrum of

[9] Also called saddle connections [34, 52].

[10] Of infinite codimension, in the sense that adding time dependence can require infinitely many parameters for the unfolding.

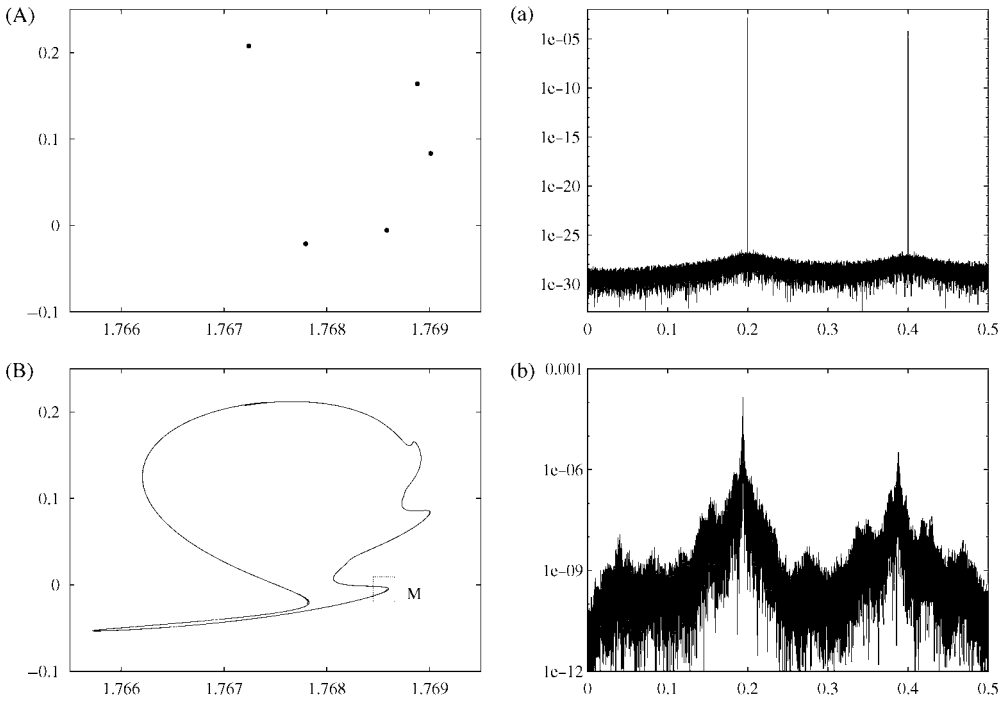

Figure 6. (*A*) Projection on the (x, z) plane of a period-five attractor of $\mathcal{P}$, for $G = 0.4107$ and $F = 1.25$. (*B*) Same as (*A*) for the SA $\mathbb{L}_1$, with $G = 0.4106$ (box M is magnified in figure 8 left). (*a*), (*b*) Power spectra for (*A*), resp. (*B*).

an attractor allows to compute its Lyapunov dimension [32,38], considered an upper bound of the Hausdorff dimension under general assumptions. In what follows, the Lyapunov exponents will be denoted by λ_1, λ_2, and λ_3, with $\lambda_1 \geqslant \lambda_2 \geqslant \lambda_3$. The Lyapunov dimension is defined by

$$\mathrm{D_L} = k + \frac{\sum_{j=1}^{k} \lambda_j}{|\lambda_{k+1}|},$$

where k is the unique index such that $\sum_{j=1}^{k} \lambda_j \geqslant 0$ and $\sum_{j=1}^{k+1} \lambda_j < 0$. Another indicator of the dynamics is the power spectrum [17, 51]. In all power spectra we plot the square of the moduli of the Fourier coefficients against the frequency, where the latter is limited to the interval $[0, 1/2]$ (see appendix A.3 for details).

The numerical results in section 4 suggest that the SAs in the family $\mathcal{P}_{F,G,\epsilon}$ usually appear due to homoclinic tangencies. Period doubling cascades are sometimes observed and, in fact, the two scenario's are not independent, see, e.g. [48, 56]. SAs were found in the four regions $\mathfrak{L}_1$, $\mathfrak{L}_2$, $\mathfrak{U}$, and $\mathfrak{U}'$ in figure 4. The birth of SA in $\mathfrak{L}_k$ is caused by different phenomena than in $\mathfrak{U}$ and $\mathfrak{U}'$.

The SA $\mathbb{L}_1$ in figure 6(*B*) occurs in $\mathfrak{L}_1$, right after the breakdown of an invariant circle[11]. For nearby parameter values, a period-five attractor is found (figure 7(*A*)), inside an Arnol'd tongue $\mathfrak{A}_{1/5}$. The highest peak in its power spectrum (figure 7(*a*)) occurs—as it should—at frequency $f_1 = 0.2$, with one harmonic at $f_2 = 2f_1$. Note that the power spectrum of $\mathbb{L}_1$ (figure 7(*b*)) still has dominant frequency components at $\tilde{f}_1 = 0.1939$ and $\tilde{f}_2 = 0.3878 \simeq 2\tilde{f}_1$, respectively close to f_1 and f_2. This persistence of the peaks is due to intermittency of type I [50]. Indeed,

[11] The notation $\mathbb{L}$ stands for large, see section 4.11.

a large number of iterates tends to stay close to the five regions inside $\mathbb{L}_1$ where the periodic attractor has just disappeared through a saddle-node bifurcation. The attractor $\mathbb{L}_1$ appears as a consequence of the destruction of the circle $\mathbb{C}_1$, caused by a homoclinic tangency inside $\mathfrak{A}_{1/5}$ (for more details on this route, see section 4.7). As a result, $\mathbb{L}_1$ has the properties of a folded circle: its dimension is close to one ($D_L(\mathbb{L}_1) \simeq 1.056$), its folded geometric structure is illustrated in figure 8(*a*).

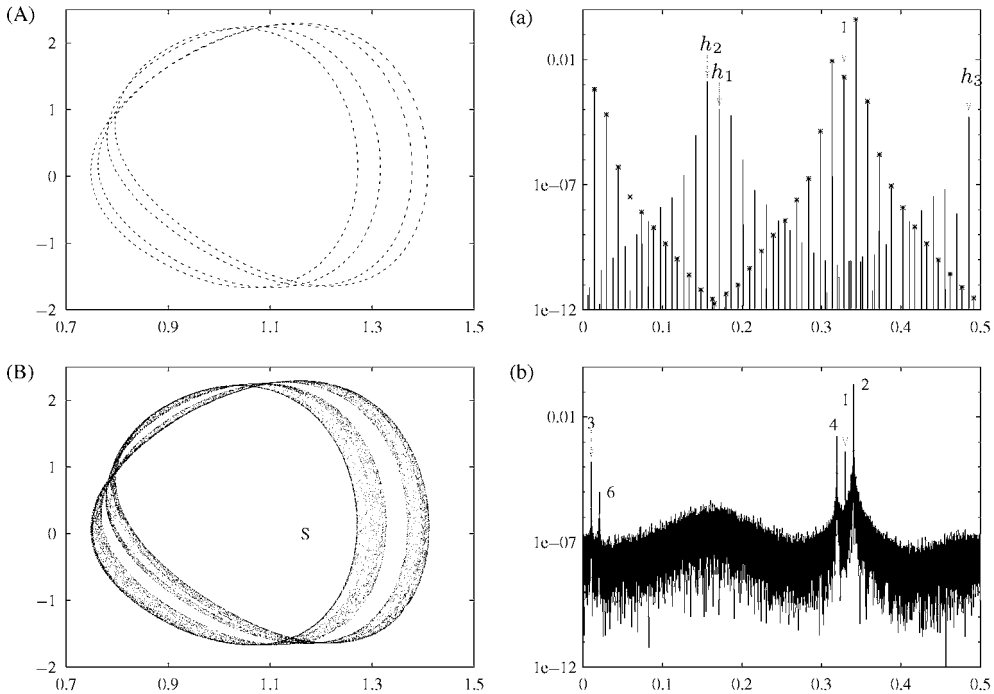

Figure 7. (*A*) Projection on (x, z) of the $\mathcal{P}$-attractor $4\mathbb{C}_1$, occurring at $(F, G) = (11, 0.4969)$. (*B*) Same as (*A*) for the SA $\mathbb{Q}_1$, with $G = 0.4972$. The section S is enlarged in figure 8 right. (*a*), (*b*) Power spectra for (*A*), resp. (*B*).

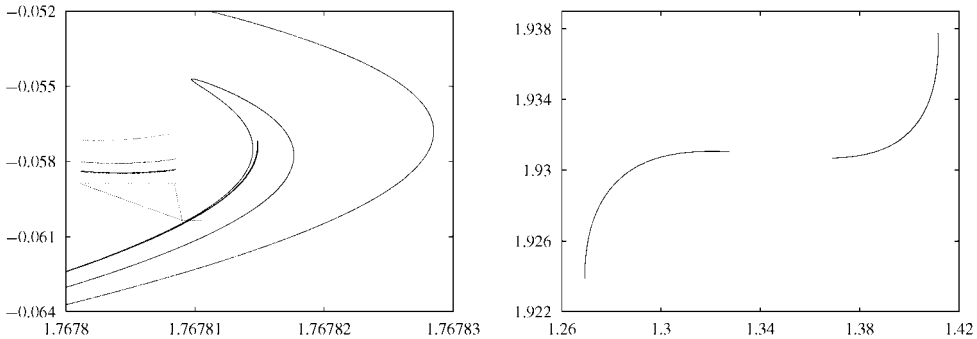

Figure 8. Left: magnification of box M in figure 6(*B*), projection on (x, y). A further magnification shows that the vertical line $x = 1.7678$ crosses the attractor in at least five layers. A new magnification (not displayed) reveals at least nine layers. To go beyond that value requires higher accuracy in the integration. Right: a section of $\mathbb{Q}_1$ contained in a layer of thickness 2×10^{-3} around the plane $z = 0$, projected on $(x, \tilde{y})$, where $\tilde{y} = y - 0.135 \times z$.

Table 1. Lyapunov dimension and exponents of $4\mathbb{C}_1$ (A) and of the SA $\mathbb{Q}_1$ (B) in figure 7. The e_i are estimates for the error in λ_i (see appendix A.2).

	D_L	λ_1	λ_2	λ_3	e_1	e_2	e_3
A	1	$1.1 \cdot e{-}5$	-0.18	-14.5	$1 \cdot e{-}6$	$1 \cdot e{-}4$	$1 \cdot e{-}4$
B	2.016	0.24	$2.6 \cdot e{-}4$	-14.9	$1 \cdot e{-}4$	$1 \cdot e{-}4$	$2 \cdot e{-}4$

Quasi-periodic bifurcations (section 3.2.2) play an important role in the birth of SAs and repellors of dimension higher than two (sections 4.9.3 and 5.1.3). Attractors such as $4\mathbb{C}_1$ in figure 7(*A*) are created by two consecutive quasi-periodic period doublings, compare section 4.9.1. The attractor $4\mathbb{C}_1$ is the union of two curves, each invariant under $\mathcal{P}^2$. We call this type of invariant set a period-two invariant curve, also see sections 4.9.1 and 5.1.3. For close parameter values, the SA $\mathbb{Q}_1$ in figure 7(*B*) is found[12].

However, a whole quasi-periodic period doubling cascade does not occur, since $4\mathbb{C}_1$ is destroyed by a homoclinic tangency inside an Arnol'd tongue (see section 4.9.3). The fact that $\lambda_2 \simeq 0$ (table 1) suggests that the dynamics on $\mathbb{Q}_1$ still preserves a quasi-periodic component, inherited from $4\mathbb{C}_1$. The power spectra of the two attractors, displayed in figures 7(*a*) and (*b*), confirm this idea. The period-two curve $4\mathbb{C}_1$ has two fundamental frequencies, one of which is of course 0.5. The other frequency $g_1 = 0.32839$ (labelled by 1 in figure 7(*a*)) is given by $j/2$, where j is the frequency of $\mathcal{P}^2$ on any of the two invariant curves. All harmonics $g_k = kg_1$ up to order 35 are identified by crosses on the corresponding peak in figure 7(*a*). The remaining peaks occur on frequencies $h_k = 0.5 - g_k$, which are integer combinations of 0.5 and g_k (the unique such combinations in the interval $[0, 0.5]$). For reference, h_1, h_2, and h_3 are labelled in figure 7(*a*).

The first four and the sixth harmonic of g_1 (labelled in figure 7(*b*)) persist in the spectrum of $\mathbb{Q}_1$, but all other harmonics have turned into broad band. This persistence of the harmonics can be again explained in terms of intermittency. Power spectra like in figure 6(*b*) or figure 7(*b*) are of mixed type [17]: they contain marked peaks (atoms of the spectral density) but also have a broad band component (locally continuous density).

The attractor $\mathbb{Q}_1$ is essentially three-dimensional, contained inside a 'fattened' Möbius strip. In reality, the fattening is rather thin, due to the size of the negative Lyapunov exponent λ_3 (table 1). Indeed, this causes strong contraction in the normal direction and therefore the Lyapunov dimension is too close to 2. This is illustrated in figure 8 right, where we plotted a section S of $\mathbb{Q}_1$ obtained by cutting it with a layer of thickness 2×10^{-3}, centred around the plane $z = 0$. For a better visualization of the thinness in the normal direction, S is 'rotated' by using transformed coordinates. This projection is less than 2.5×10^{-6} wide in $\tilde{y}$, so that a Hénon-like structure in the normal direction cannot be distinguished. Values of x are limited in (1.1, 1.5), corresponding to segment S in figure 7(*B*). We had to compute 10^8 iterates to achieve the 13 005 points inside S plotted in the picture.

The above scenarios are quite common for the family $\mathcal{P}_{F,G,0.5}$, close to the breakdown of an invariant circle in $\mathfrak{L}_1$ or $\mathfrak{L}_2$. However, intermittency disappears as the parameters are shifted deeper inside $\mathfrak{L}_k$. The Lyapunov dimension increases, as well as the total power contained in the broad band component of the power spectra (sections 4.8 and 4.9).

SAs of a different type occur in $\mathfrak{U}$ (figures 9(*A*) and 10(*A*)). The geometrical and dynamical structure of broken invariant circles is no longer present: the power spectra look like white noise, indicating that the iterates of $\mathcal{P}$ are uncorrelated (see remark A.1 in appendix A.3). We call these attractors 'Shil'nikov-like' because their shape is similar to that of Shil'nikov repellors

[12] The notation $\mathbb{Q}$ stands for quasi-periodic Hénon-like, see section 4.9.3

found in the autonomous Lorenz-84 system $\epsilon = 0$. In [55], the presence of such repellors was put in relationship with the occurrence of two curves of Shil'nikov bifurcations [34, 40], corresponding to homoclinic loops of a saddle-focus equilibrium. For nearby parameter values, limit cycles like in figure 11 were detected. Because of oscillations followed by long excursions,

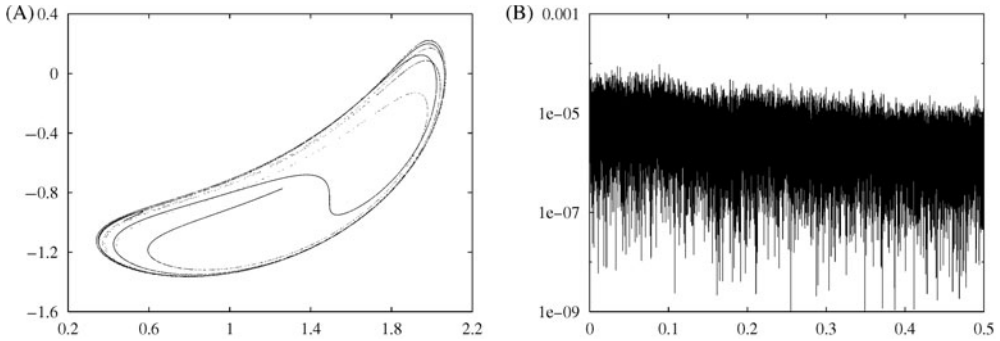

Figure 9. (*A*) Projection on (y, z) of the Shil'nikov-like strange $\mathcal{P}$-attractor $\mathbb{S}_1$, occurring at $(F, G) = (7, 1.7545)$. (*B*) Power spectrum of $\mathbb{S}_1$.

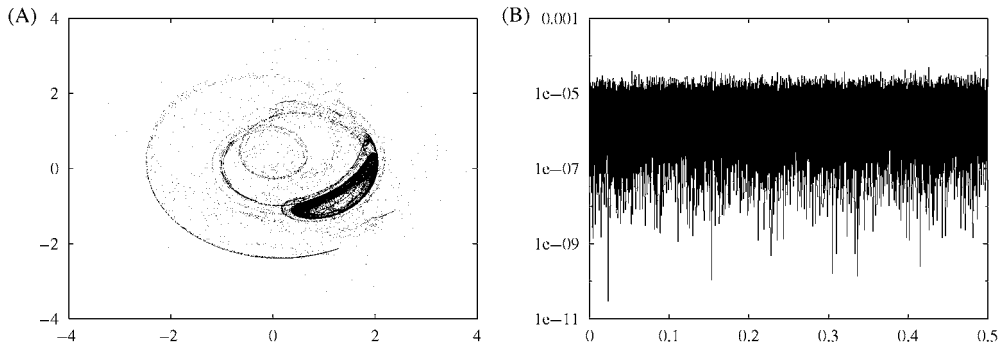

Figure 10. (*A*) Projection on (y, z) of the Shil'nikov-like strange $\mathcal{P}$-attractor $\mathbb{S}_2$, occurring at $(F, G) = (7, 1.7)$. (*B*) Power spectrum of $\mathbb{S}_2$.

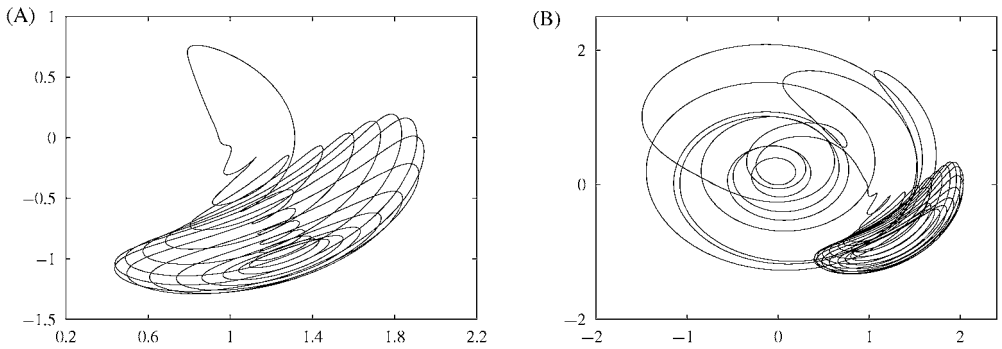

Figure 11. (*A*) Projection on (y, z) of 'spiral' limit cycle of (2), occurring at $(F, G) = (7, 1.754\,66)$. (*B*) Same as (*A*) for $G = 1.7015$.

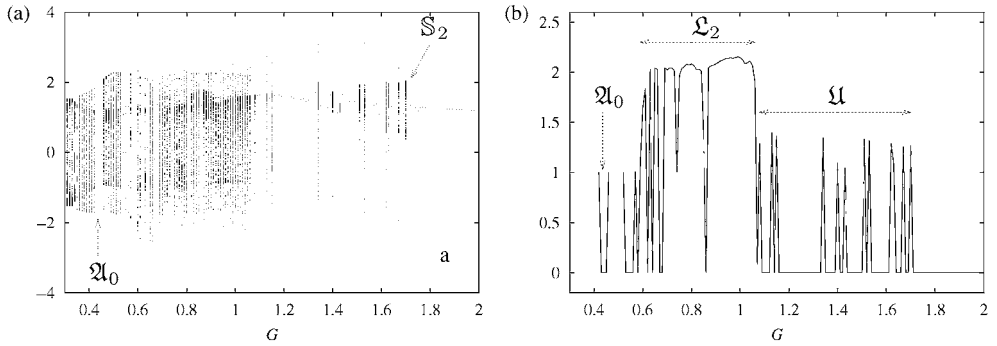

Figure 12. (*a*) Projection on the y-axis of sequences of $\mathcal{P}$-attractors as a function of G for $F = 7$ fixed. The step in G is 0.01. An Arnol'd tongue $\mathfrak{A}_0$ of rotation number 0 is pointed by an arrow. The attractor pointed by an arrow is plotted in figure 10(*A*). (*b*) Lyapunov dimension of the attractors in (*a*).

such limit cycles are called spiral attractors [55]. In the driven Lorenz-84, spiral limit cycles occur for most parameter values in $\mathfrak{U}$ and $\mathfrak{U}'$. Only narrow Hénon-like attractors seem to occur in $\mathfrak{U}'$ (see figures 38(*a*) and 51(*a*)). Similar attractors are found also in $\mathfrak{U}$.

The differences between $\mathfrak{U}$ and $\mathfrak{L}_2$ are illustrated by means of the Lyapunov dimension. In figure 12(*a*) we plotted a magnification of figure 1(*e*). On the left of the picture, the circle $\mathbb{C}_1$ occurs: the Lyapunov dimension (figure 12(*b*)) is one, since the maximal Lyapunov exponent is zero. After crossing an Arnol'd tongue $\mathfrak{A}_0$ of rotation number zero, $\mathbb{C}_1$ locks again to a periodic point on a small interval and then breaks down. The Lyapunov dimension grows almost immediately up to $\sim$2.1. Except for a few narrow Arnol'd tongues (where the dimension drops to zero), SAs are prevalent in the chaotic range $\mathfrak{L}_2$. Then, at $G \simeq 1.08$, some bifurcation occurs[13], after which the evolution of the attractors changes significantly. For most parameter values in $\mathfrak{U}$ an attracting fixed point is found (in the intervals of zero Lyapunov dimension in figure 12(*d*)). The corresponding T-periodic limit cycles of system (2) are of spiral type. Shil'nikov–like SAs as in figure 10(*A*) occur for a few parameter values, individuated by the peaks in the Lyapunov dimension (figure 12(*d*)) and by some fuzzy vertical lines in figure 12(*a*). Further discussion on the classification of the SAs of $\mathcal{P}$ for $\epsilon = 0.5$ is to be found in section 4.11.

We now list some more points of interest of the family $\mathcal{P}_{F,G,\epsilon}$. Since the autonomous system (for $\epsilon = 0$) exhibits Shil'nikov bifurcations, we may well expect three-dimensional homoclinic tangencies of a saddle focus fixed point of a diffeomorphism. For analogy with the autonomous case, we shall call this multidimensional homoclinic bifurcation 'Shil'nikov tangency bifurcation' (section 3.2.1).

A large variety of SAs can be found for $\mathcal{P}_{F,G,\epsilon}$ Some of these are essentially three-dimensional[14] and have dimension d with $2 < d \leqslant 3$. The theory for this class of attractors has not yet completely been developed: only partial results have been proven so far (see, e.g. [62, 65]). Also the Newhouse–Ruelle–Takens scenario [46, 53] may occur, since for small ϵ the map $\mathcal{P}_{F,G,\epsilon}$ has a repelling invariant two-torus $\mathbb{T}$ inherited from the autonomous system (section 3.2.2).

As we have seen, the driven Lorenz-84 model displays a rich dynamics, with various bifurcations of the attractors. The chaotic ranges in the parameter plane are wide. It is a challenge to understand the corresponding bifurcation patterns of this model. The present paper

[13] This happens on the 'curve' labelled by $\mathcal{SH}$ in figure 4.

[14] By this we mean that they are no suspension of a two-dimensional attractor.

aims at giving a rough inventory of the dynamics and an analysis of some of the bifurcations at hand.

2. Analytical results on $\mathcal{P}$

In this section, we prove the following properties of the family $\mathcal{P}_{F,G,\epsilon}$:

1. For all F, G, ϵ the map $\mathcal{P}_{F,G,\epsilon}$ has an attractor (section 2.1).
2. For G large, $\mathcal{P}_{F,G,\epsilon}$ has a unique attracting fixed point $\mathbb{A}$ (section 2.2).
3. For $G = 0$ $\mathcal{P}_{F,G,\epsilon}$ has a unique fixed point, which is attracting for $F \leqslant 1$ and undergoes a supercritical Hopf bifurcation at $F = 1$.

The results are formulated in terms of the following system:

$$\begin{aligned} \dot{x} &= -ax - y^2 - z^2 + aFf(t), \\ \dot{y} &= -y + xy - bxz + Gg(t), \\ \dot{z} &= -z + bxy + xz, \end{aligned} \tag{3}$$

with T-periodic continuous functions $f, g : \mathbb{R} \to \mathbb{R}$. System (2) is a particular case of (3), where $f(t) = g(t) = 1 + \epsilon\cos(\omega t)$. At the end of each section, we describe the implications for the map $\mathcal{P}_{F,G,\epsilon}$.

2.1. Existence of attractors

For the autonomous Lorenz-84, there exists a bounded set in the phase space $\mathbb{R}^3 = \{x, y, z\}$, depending on the parameters F, G, which attracts all trajectories [42]. A similar property holds for system (3). Let $\|f\|_\infty \stackrel{\text{def}}{=} \sup_{t\in\mathbb{R}} |f(t)|$.

Proposition 2.1. *For $a > 0$ and every b, F, G, there exists a sphere $\mathfrak{S} \subset \mathbb{R}^3$ centred at $(x, y, z) = (0, 0, 0)$ with radius R_0 depending on $a, F, G, \|f\|_\infty, \|g\|_\infty$, such that all integral curves of (3) ultimately penetrate $\mathfrak{S}$ and then remain inside.*

Proof. We denote the Euclidean norm on $\mathbb{R}^2$ or $\mathbb{R}^3$ by $\|\ \|$. Consider a solution $(x, y, z)(t)$ of equation (3) and define $R(t) = \|(x, y, z)\|$. Using (3), we have

$$\frac{1}{2}\frac{\mathrm{d}}{\mathrm{d}t}(R^2) = -ax^2 - y^2 - z^2 + xaFf(t) + yGg(t) \leqslant -\tilde{a}R^2 + R\sqrt{a^2F^2\|f\|_\infty^2 + G^2\|g\|_\infty^2},$$

where $\tilde{a} \stackrel{\text{def}}{=} \min\{a, 1\}$. We have used the Schwartz inequality: $xaFf(t) + yGg(t) = (aFf(t), Gg(t)) \cdot (x, y) \leqslant \|(aFf(t), Gg(t))\|\|(x, y)\|$. For R large enough, namely,

$$R > \tilde{a}^{-1}\sqrt{a^2F^2\|f\|_\infty^2 + G^2\|g\|_\infty^2} \stackrel{\text{def}}{=} R_0,$$

the function $R(t)$ is decreasing. Notice that it is sufficient to require that $f(t)$ and $g(t)$ be bounded on $\mathbb{R}$. □

Since $f(t) = g(t) = 1 + \epsilon\cos(\omega t)$ and $a < 1$ in system (2), the radius of the attracting sphere $\mathfrak{S}$ for the map $\mathcal{P}_{F,G,\epsilon}$ is $R_0 = (1 + \epsilon)\sqrt{F^2 + G^2/a^2}$.

2.2. Occurrence of a unique fixed point attractor of $\mathcal{P}_{F,G,\epsilon}$ for G large

Proposition 2.2. *For all $a > 0$ and every b, F there exists a G_0 such that for all $G > G_0$, system (3) has a unique attracting periodic solution p^G.*

Proof. We scale the variables x, y, z of (3) as follows:

$$u = \delta^2 x, \quad v = \delta y, \quad w = \delta z, \qquad \text{with } \delta = G^{-1/3},$$

so obtaining

$$\begin{aligned} \dot{u} &= -au - v^2 - w^2 + aF\delta^2 f(t), \\ \delta^2 \dot{v} &= -\delta^2 v + uv - buw + g(t), \\ \delta^2 \dot{w} &= -\delta^2 w + buv + uw. \end{aligned} \tag{4}$$

As G tends to infinity, δ approaches zero and (4) becomes a singularly perturbed system. For $\delta = 0$ we obtain the degenerate system

$$\dot{u} = -au - v^2 - w^2, \qquad u(v - bw) + g(t) = 0, \qquad u(bv + w) = 0.$$

The latter two equations yield

$$w = -bv, \qquad v = -\frac{g(t)}{(1 + b^2)u}. \tag{5}$$

Substituting (5) in (4), we get the one-dimensional equation

$$\dot{u} = -au - \frac{g^2(t)}{(1 + b^2)u^2}. \tag{6}$$

With the change of variables $p = u^3$, we obtain the linear differential equation

$$\frac{1}{3}\dot{p} = -ap - \frac{g^2(t)}{1 + b^2}. \tag{7}$$

The solution of the Cauchy problem given by (7) with initial condition p_0 is

$$p(t) = \mathrm{e}^{-3at}\left(p_0 - \frac{3}{1 + b^2}\int_0^t \mathrm{e}^{3as} g^2(s)\,\mathrm{d}s\right).$$

The initial condition $p_0 = 3(1 + b^2)^{-1}(1 - \mathrm{e}^{3aT})^{-1}\int_0^T \mathrm{e}^{3as} g^2(s)\,\mathrm{d}s$ belongs to a T-periodic solution $p_T(t)$, asymptotically stable and negative for all t. Given a solution $p(t)$ with initial condition $p_1 \in \mathbb{R}$, we have indeed $p(t) - p_T(t) = \mathrm{e}^{-3at}(p_1 - p_0)$ which tends to zero as $t \to +\infty$, since $a > 0$.

Thus for $\delta = 0$, system (4) has a globally attracting periodic solution $s^0(t) = (u_T, v_T, w_T)$, where $u_T = (p_T)^{1/3}$ and v_T, w_T are obtained from u_T according to (5). We now prove that for δ small, that is, for G large, system (4) has a period T solution $s^\delta(t) = (u(t), v(t), w(t))$ such that $s^\delta(t) \to s^0(t)$ uniformly in $t \in [0, T]$ as $\delta \to 0$. The variational equation associated to (6) and to u_T is

$$\dot{V} = \left(-a + 2\frac{g^2(t)}{(1 + b^2)u_T^3}\right)V, \qquad V(0) = 1, \qquad V = \frac{\partial u_T}{\partial u_0}. \tag{8}$$

According to [29], it is sufficient to show that the unique T-periodic solution of (8) is identically zero. Since $p_T = u_T^3$ is solution of (7), we have

$$\frac{g^2(t)}{(1 + b^2)u_T^3(t)} = \frac{g^2(t)}{(1 + b^2)p_T(t)} = -a - \frac{1}{3}\frac{\mathrm{d}}{\mathrm{d}t}\log(p_T(t)).$$

Hence (8) becomes

$$\frac{\mathrm{d}}{\mathrm{d}t}\log(V(t)) = -3a - \frac{2}{3}\frac{\mathrm{d}}{\mathrm{d}t}\log(p_T(t)).$$

Therefore, the solution of (8) is

$$V(t) = \mathrm{e}^{-3at}\left(\frac{p_T(t)}{p_0}\right)^{-2/3},$$

which tends to zero as $t \to +\infty$. In the original coordinates (x, y, z), s^δ corresponds to a unique attracting T-periodic solution p^G of (3), existing for G large. □

The occurrence of a unique attracting periodic orbit p^G was suggested by numerical experiments with system (2). In that case, p^G corresponds to the $\mathcal{P}$-fixed point $\mathbb{A}$ occurring for G large (region $\mathfrak{F}$ in figure 4).

2.3. Invariant circles for $G = 0$

Numerical experiments with the map $\mathcal{P}_{F,G,\epsilon}$ suggest that for $G = 0$, $F > 1$, and $0 \leqslant \epsilon < 1$ (and possibly for a small range beyond $\epsilon = 1$), the map has an invariant circle $\mathbb{C}_1$, born at $F = 1$ at a Hopf bifurcation of a fixed point. We here prove that for $G = 0$ and all F, the map $\mathcal{P}_{F,\epsilon} = \mathcal{P}_{F,0,\epsilon}$ has a fixed point undergoing a Hopf bifurcation at $F = 1$. Existence of the invariant circle for all $F > 1$ will be proved for ϵ small.

We now consider the periodic orbits of system (3). Given a function $h : \mathbb{R} \to \mathbb{R}$, denote by $\bar{h}$ the average of h over the interval $[0, T]$, i.e. $\bar{h} \stackrel{\text{def}}{=} (1/T) \int_0^T h(s)\,\mathrm{d}s$.

Proposition 2.3. *Suppose $\bar{f} \neq 0$. For all F system (3) has a unique T-periodic orbit $p^F(t)$, which is stable for $F \leqslant \bar{f}^{-1}$ and undergoes a Hopf bifurcation at $F = \bar{f}^{-1}$.*

Proof. For $G = 0$ system (3) has a symmetry and its dimension can be reduced. Indeed, the Cauchy problem given by (3) with initial condition (x_0, y_0, z_0) is equivalent to the reduced system

$$\begin{aligned} \dot{u} &= -au - r - a + aFf(t), \qquad u(0) = u_0, \\ \dot{r} &= 2ur, \qquad\quad r(0) = r_0, \end{aligned} \tag{9}$$

where $r = y^2 + z^2$ and $u = x - 1$. The u-axis is invariant under the flow of (9). Putting $r = 0$, the first equation of (9) can be solved, giving

$$u(t) = \mathrm{e}^{-at}\left(u_0 + 1 - \mathrm{e}^{at} + aF\int_0^t \mathrm{e}^{as} f(s)\,\mathrm{d}s\right).$$

A unique periodic solution $u_T(t)$ exists, with initial condition

$$u_0 = \frac{1}{\mathrm{e}^{aT} - 1}\left(1 - \mathrm{e}^{aT} + aF\int_0^T \mathrm{e}^{as} f(s)\,\mathrm{d}s\right).$$

This implies that system (3) has a unique periodic solution $p^F(t) = (u_T(t)+1, 0, 0)$ for $r_0 = 0$. We now prove that system (9) has no periodic solutions other than $p^F(t)$. Since we shall use the following fact again, we state it in a remark. □

Remark 2.1. Consider a T-periodic solution $(u, r)(t)$ of (9). Then, either $r(t) = 0$ or $\bar{u} = 0$. Indeed, from the second equation in (9), one has

$$r(t) = r_0 \exp\left(2\int_0^t u(s)\,\mathrm{d}s\right).$$

From $r(T) = r(0) = r_0$, it follows that either $r_0 = 0$, or $\int_0^T u(s)\,\mathrm{d}s = 0$.

Continuing the proof, suppose that $(x, y, z)(t)$ is a T-periodic solution of (3) and take the corresponding solution $(u, r)(t)$ of (9). Averaging the first of the equations (9) over $[0, T]$ yields

$$\bar{u} = F\bar{f} - 1 - \bar{r}/a.$$

If $F\bar{f} - 1 \leqslant 0$, remark 2.1 implies that $r = y^2 + z^2$ must be zero. Therefore, $(x, y, z)(t)$ coincides with $p^F(t)$ (up to a time shift). If $F\bar{f} - 1 > 0$, then the functions y and z have the form

$$y(t) = r(t)\cos(-bt + \theta_0), \qquad z(t) = r(t)\sin(-bt + \theta_0), \tag{10}$$

and they are not periodic[15] unless $r = 0$.

To determine stability, we integrate the variational equation associated to (9) and $p^F(t) = (u_T(t) + 1, 0, 0)$:

$$\dot{V} = \begin{pmatrix} -a & 0 & 0 \\ 0 & u_T(t) & -b(u_T(t)+1) \\ 0 & b(u_T(t)+1) & u_T(t) \end{pmatrix} V, \qquad V(0) = \begin{pmatrix} 1 & 0 & 0 \\ 0 & 1 & 0, \\ 0 & 0 & 1 \end{pmatrix} \tag{11}$$

where V is the derivative of the flow of (9) with respect to initial conditions (x_0, y_0, z_0). Since $\dot{V}_{1k} = -aV_{1k}, k = 1, 2, 3$, the first row of the monodromy matrix $V(T)$ is $(V_{11}, V_{12}, V_{13})(T) = (\mathrm{e}^{-aT}, 0, 0)$. Therefore, one eigenvalue of $V(T)$ is e^{-aT} and the other two do not depend on V_{21} and V_{31}. On the other hand, it is easy to see that

$$V_{32} = -V_{23} \qquad \text{and} \qquad V_{22} = V_{33}. \tag{12}$$

Indeed, define $W_1 = V_{22} - V_{33}$ and $W_2 = V_{23} + V_{32}$. Using (11), one gets a linear homogeneous Cauchy problem for W_1 and W_2, with initial conditions $W_1^{(0)} = W_2^{(0)} = 0$, which implies that $W_1(t) = W_2(t) = 0$. So it is sufficient to solve the problem

$$\begin{aligned} \dot{V}_{22} &= u_T V_{22} + b(u_T + 1)V_{23}, & V_{22}^{(0)} &= 1, \\ \dot{V}_{23} &= -b(u_T + 1)V_{22} + u_T V_{23}, & V_{23}^{(0)} &= 0. \end{aligned} \tag{13}$$

We put (13) in complex form:

$$\dot{Z} = A(t)Z, \qquad \text{where } Z = V_{22} + \mathrm{i}V_{23}, \quad A = u_T - \mathrm{i}b(u_T + 1).$$

Integration of the previous equation yields

$$(V_{22} + \mathrm{i}V_{23})(T) = \exp\left(\int_0^T u_T(s)\,\mathrm{d}s\right)\exp\left(-\mathrm{i}b\int_0^T (u_T(s) + 1))\,\mathrm{d}s\right).$$

Using (12), one gets that the other two eigenvalues μ_2 and μ_3 of $V(T)$ are complex conjugated. Since their modulus is

$$\exp\left(\int_0^T u_T(s)\,\mathrm{d}s\right) = \exp(T(F\bar{f} - 1)),$$

then $p^F(t)$ is stable for $F\bar{f} - 1 < 0$ and it loses stability as F increases through $1/\bar{f}$, because μ_2 and μ_3 cross the unit circle. Furthermore, we have

$$\arg(\mu_2) = -b\int_0^T (u_T(s) + 1))\,\mathrm{d}s = -bTF\bar{f},$$

which is equal to $-bT$ at the moment of the bifurcation. Since $-bT/2\pi$ is irrational[15], a Hopf bifurcation takes place. □

We now show that in the autonomous case equation (9) has a unique global attractor for $F > 1$.

[15] This holds with the choice $b = 4$ and $T = 73$, for which $bT/2\pi = 146/\pi$ is irrational.

Proposition 2.4. *Consider system (9), with $F > 1$ and $f(t) = 1$ for all t. The equilibrium $B = (0, a(F-1))$ is the unique global attractor of (9).*

Proof. For $F > 1$, the vector field $\mathcal{V}$ in (9) has two equilibria, B, which is stable, and the saddle $A = (F-1, 0)$. By the Poincaré–Bendixson theorem, an attractor of the flow of (9) can be an equilibrium or a periodic orbit. We now show that the flow of (9) has no periodic orbits. The divergence $\mathrm{div}\mathcal{V} = -a + 2u$ of $\mathcal{V}$ is negative for all (u, r) at the left of the line Z of zero divergence (figure13). We distinguish two cases. Suppose first that the saddle A lies at the left of line Z, that is, $1 < F < 1 + a/2$. Since the vector field $\mathcal{V}$ points leftward on all points of the vertical line K given by $(u = F - 1)$, any periodic orbit must lie at the left of K. But no periodic orbit can exist there, because the divergence is negative at the left of Z.

Take now an arbitrary F. If $\mathcal{V}$ has a periodic orbit, the former must be born at a saddle-node bifurcation of periodic orbits. Indeed, no Hopf bifurcation of equilibria occurs for $\mathcal{V}$, since the two equilibria never change stability type. Consider thus a saddle-node periodic orbit $\mathbb{O}$ of period M, parametrized by $(u(s), r(s))$ for $s \in [0, M]$. Take a Poincaré map $\mathcal{S}$, defined in a suitable local section of $\mathbb{O}$. The eigenvalue μ of the derivative $D\mathcal{S}$ at the fixed point of $\mathcal{S}$ corresponding to $\mathbb{O}$ is one. On the other hand, remark 2.1 yields that $\bar{u} = 0$ and therefore

$$\log(\mu) = \int_0^M \mathrm{div}\mathcal{V}(u(s), r(s))\,\mathrm{d}s = \int_0^M (-a + 2u(s))\,\mathrm{d}s = -aM < 0,$$

which gives a contradiction. □

We now discuss the consequences of the above propositions for the family $\mathcal{P}_{F,G,\epsilon}$. Here we have $f(t) = 1 + \epsilon\cos(\omega t)$, therefore $\bar{f} = 1$. The map $\mathcal{P}_{F,G,\epsilon}$ has a unique fixed point for $G = 0$ and all F, ϵ, which is stable for $F < 1$ and undergoes a Hopf bifurcation at $F = 1$. A circle attractor $\mathbb{C}_1$ is created there, but its persistence in F is guaranteed only for $F \approx 1$, by the theory of the Hopf bifurcation. On the other hand, hyperbolicity of the stable equilibrium B in proposition 2.4 implies that system (9) has an attracting T-periodic orbit when applying a small T-periodic perturbation $f(t)$ (small in the sense that $\|f - 1\|_\infty$ is small). For the map $\mathcal{P}_{F,G,\epsilon}$, this implies the existence of the circle attractor $\mathbb{C}_1$ for all F and for small G and ϵ.

A remarkable consequence of (10) is that for *all* $F > 1$ the rotation number ϱ is the constant on $\mathbb{C}_1$, namely $-bT/2\pi$. This situation is not generic in a family of circle mappings. Indeed, given the physical meaning of G (section 1.1), the system for $G = 0$ seems to have too much symmetry and to be degenerate.

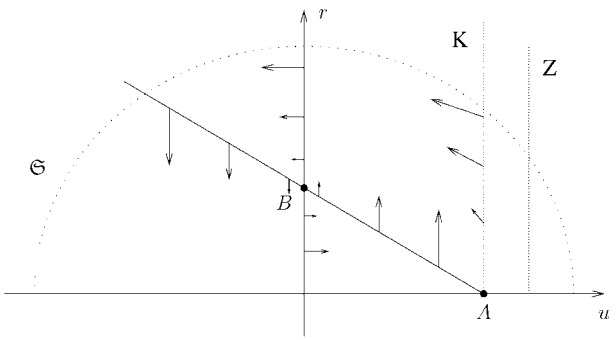

Figure 13. Phase portrait of the vector field $\mathcal{V}$. The dashed half circle represents the attracting sphere $\mathfrak{S}$ obtained in section 2.1. The case $1 < F < 1 + a/2$ is sketched, for which the line Z $(u = a/2)$ of zero divergence lies at the right of the saddle A.

Table 2. Equivalences for $\epsilon = 0$ between invariant dynamical objects of the flow $\Phi_{F,G}$ of system (1) (left), of the flow $\Psi_{F,G,\epsilon}$ of system (2) (centre), and of the Poincaré map $\mathcal{P}_{F,G,\epsilon}$. Centre and right column items are equivalent also for $\epsilon > 0$.

$\Phi_{F,G}$		$\Psi_{F,G,\epsilon}$		$\mathcal{P}_{F,G,\epsilon}$
equilibrium	$\leftrightarrow$	period-T limit cycle	$\leftrightarrow$	fixed point
limit cycle	$\leftrightarrow$	two-torus	$\leftrightarrow$	invariant circle
two-torus	$\leftrightarrow$	three-torus	$\leftrightarrow$	two-torus

3. The driven system as a perturbation from $\epsilon = 0$

We now investigate the relations between the dynamics of the driven and the autonomous Lorenz-84, first introducing some notation. The flows of system (1) and (2) will be denoted by $\Phi_{F,G}$ and $\Psi_{F,G,\epsilon}$ respectively, where

$$\Phi_{F,G} : \mathbb{R}^3 \times \mathbb{R} \to \mathbb{R}^3, \qquad (x, y, z; s) \mapsto \Phi^s_{F,G}(x, y, z),$$

$$\Psi_{F,G,\epsilon} : \mathbb{R}^4 \times \mathbb{R} \to \mathbb{R}^4, \qquad (x, y, z, t; s) \mapsto (\Psi^s_{F,G,\epsilon}(x, y, z, t), t + s).$$

The two flows are equivalent when $\epsilon = 0$. More precisely, one has

$$\Psi^s_{F,G,0}(x, y, z, 0) = \Phi^s_{F,G}(x, y, z) \qquad \text{for every } (x, y, z, s) \in \mathbb{R}^4.$$

Therefore, $\Phi_{F,G}$-invariant dynamical objects are also $\Psi_{F,G,0}$-invariant. On the other hand, any dynamical property of $\Psi_{F,G,\epsilon}$ can be expressed in terms of the Poincaré map $\mathcal{P}_{F,G,\epsilon}$, see table 2. Notice that the flow $\Psi_{F,G,0}$ does not have equilibria, since $\dot{t} = 1$ in system (2). A hyperbolic equilibrium $q = (x, y, z)$ of Φ is said to be of type (m, n), with $m + n = 3$, if m eigenvalues of the linear part of the vector field (1) at q have negative real part, while n have positive real part. Similarly, a hyperbolic fixed point q of the map $\mathcal{P}$ is of type (m, n) if m eigenvalues of the derivative $D\mathcal{P}$ have modulus less than one and the remaining n lie outside the unit circle in the complex plane. At least one of the eigenvalues of $D\mathcal{P}_{F,G,\epsilon}$ at a fixed point is real.

We use the term Hopf bifurcation in each of the following cases.

1. Two complex conjugate eigenvalues of the linear part of the vector field (1) at an equilibrium cross the imaginary axis and a limit cycle of the three-dimensional flow Φ is born.
2. Two complex conjugate Floquet multipliers $\gamma \exp(\pm 2\pi \mathrm{i}\varrho)$ of a limit cycle of $\Phi_{F,G}$ or $\Psi_{F,G,\epsilon}$ cross the unit circle[16] and an invariant two-torus is born.
3. Two complex conjugate eigenvalues $\gamma \exp(\pm 2\pi \mathrm{i}\varrho)$ of a fixed point of the map $\mathcal{P}$ cross the unit circle[16] and an invariant circle is born.

Notice that no limit cycle of the four-dimensional flow Ψ can be born in a standard Hopf bifurcation, since Ψ has no equilibria. Case 2 is often called Naimark–Sacker or torus bifurcation, also see footnote 8.

3.1. The autonomous system

We present some results on the autonomous Lorenz-84 system, mainly due to Shil'nikov *et al* [55]. The discussion begins by the bifurcation diagram of the flow $\Phi_{F,G}$ (figure 14). For background on bifurcation theory and the relevant terminology see [16,34,40]. The organizing centres are the following codimension two bifurcation points: a cusp $\mathcal{C}$, a Hopf-saddle-node

[16] With $\varrho \neq \pm 1/k$, for $k = 1, \ldots, 4$. These are codimension two bifurcations, called strong resonances [34,40].

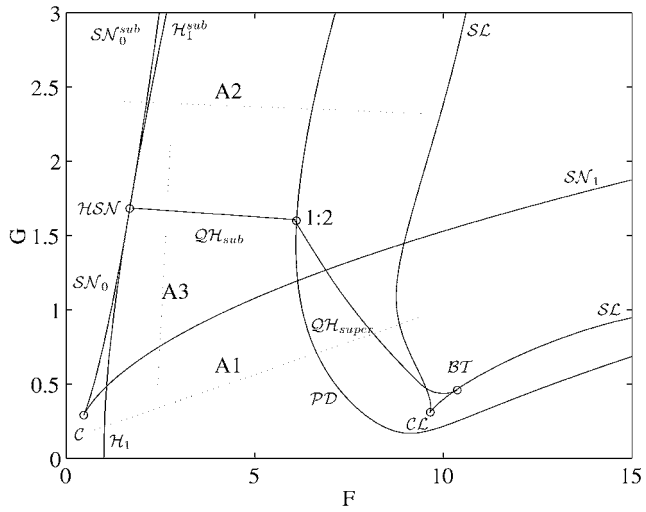

Figure 14. Bifurcation diagram of the autonomous system (1), from [36].

point $\mathcal{HSN}$, both bifurcations of equilibria; a $1:2$ resonance point, a Bogdanov–Takens point[17] $\mathcal{BT}$ and a cusp $\mathcal{CL}$, all bifurcations of limit cycles. Two branches of saddle-node curves of equilibria $\mathcal{SN}_0$ and $\mathcal{SN}_1$ meet tangentially at $\mathcal{C}$, forming a tongue-shaped region. In the neighbourhood of $\mathcal{C}$, three equilibria (two sinks and one saddle) coexist inside this tongue and only one sink $\mathbb{A}$ occurs outside.

A curve $\mathcal{H}_1$ of Hopf bifurcations of equilibria emanates from $(F, G) = (1, 0)$. The curves $\mathcal{SN}_0$ and $\mathcal{H}_1$ are tangent at the point $\mathcal{HSN}$. Above $\mathcal{HSN}$, both curves become subcritical and are denoted by $\mathcal{SN}_0^{\text{sub}}$ and $\mathcal{H}_1^{\text{sub}}$. A second curve $\mathcal{H}_2$ of supercritical Hopf bifurcations of equilibria (not reported in figure 14) has been numerically computed in [55].

A curve of period doubling of limit cycles is marked by $\mathcal{PD}$. It is split by a $1:2$ resonance point into a subcritical and a supercritical part, where the former lies above the $1:2$ point. This point is connected to $\mathcal{HSN}$ by a curve $\mathcal{QH}_{\text{sub}}$ of subcritical Hopf bifurcations of limit cycles. The Bogdanov–Takens point $\mathcal{BT}$ is connected to $1:2$ by a curve $\mathcal{QH}_{\text{super}}$ of supercritical Hopf bifurcations of limit cycles. The two curves indicated by $\mathcal{SL}$ (meeting at a cusp $\mathcal{CL}$) are saddle-node bifurcations of limit cycles.

We now explain how the dynamics varies with the parameters. A unique stable focus $\mathbb{A}$ exists for small F, to the left of curve $\mathcal{H}_1$ and outside the tongue with tip at $\mathcal{C}$. Following dashed segment A1 in figure 14, from left to right: at the Hopf curve $\mathcal{H}_1$, below $\mathcal{HSN}$, $\mathbb{A}$ splits into an attracting limit cycle $\mathbb{M}$ and a saddle $\mathbb{B}_1$ of type $(1, 2)$. At $\mathcal{PD}$, below the $1:2$ point, $\mathbb{M}$ loses stability and an attracting limit cycle $2\mathbb{M}$ is created. Crossing the curve $\mathcal{QH}_{\text{super}}$, $2\mathbb{M}$ loses stability and an attracting two-torus is created. Following segment A2 from left to right: the saddle focus $\mathbb{B}_1$ and a repelling equilibrium are generated in a subcritical saddle-node bifurcation at the curve $\mathcal{SN}_0$. Crossing $\mathcal{H}$, the repellor turns into a saddle focus $\mathbb{B}_2$ of type $(2, 1)$ and a repelling limit cycle $\mathbb{M}$ is created. Then $\mathbb{M}$ undergoes a subcritical period doubling at the curve $\mathcal{PD}$. Following segment A3 from top to bottom: crossing the curve $\mathcal{QH}_{\text{sub}}$ downwards, $\mathbb{M}$ becomes attracting and a two-torus repellor is created. At $\mathcal{SN}_1$ the saddle $\mathbb{B}_2$ collides with the attractor $\mathbb{A}$.

It is known [19,34,40] that the bifurcation diagram near a Hopf-saddle-node point of three-dimensional vector field generically shows subordinate Shil'nikov bifurcations of equilibria.

[17] Synonymous for the $1:1$ generic strong resonance.

The latter is a complicated homoclinic phenomenon which may cause the birth of Shil'nikov SAs. Two curves of Shil'nikov homoclinic bifurcations (not reported in figure 14) were computed numerically in [55]. Some other routes to chaos in Lorenz-84, such as cascades of period doublings, have been described in [43, 55].

Remark 3.1. It seems that some features of the above bifurcation diagram are rather common among low-dimensional systems with two parameters (cf [67]). Main ingredients are one Hopf-saddle-node point, a 1 : 2 strong resonance and a Bogdanov–Takens point, connected by bifurcation curves of limit cycles. These global configurations are likely to be caused by a higher codimension bifurcation, 'hidden in the background' because of the lack of a sufficient number of active control parameters. A similar idea is expressed in the work of Carcassès *et al* [21] (see also [16] and references therein), who show that semi-global patterns formed by curves of period doubling and saddle-node bifurcation are confined to a certain number of configurations due to geometrical reasons.

One of the goals of the present work is to investigate which parts of the diagram in figure 14 persist for the map $\mathcal{P}_{F,G,\epsilon}$ with $\epsilon > 0$ and to find out which bifurcations play a role in the changes.

3.2. Persistent dynamical properties

We here summarize which dynamical properties of the autonomous Lorenz-84 system persist in the driven system for ϵ small.

Starting point is the bifurcation diagram in figure 14. Assuming the correspondences in table 2, all bifurcations of equilibria for $\Psi_{F,G}$ turn into bifurcations of fixed points for $\mathcal{P}_{F,G,0}$. Similarly, bifurcations of limit cycles of $\Psi_{F,G}$ turn into bifurcations of invariant circles $\mathcal{P}_{F,G,0}$. According to classical perturbation theory [4, 23, 34], hyperbolic [35, 52] fixed or periodic points, normally hyperbolic invariant circles and quasi-periodic tori of $\mathcal{P}_{F,G,0}$ persist for $\mathcal{P}_{F,G,\epsilon}$, if the size ϵ of the perturbation is small. In the next section, we make a stronger statement, namely that for small ϵ the local bifurcation diagram of fixed points of $\mathcal{P}_{F,G,\epsilon}$ is a continuous deformation of that for $\epsilon = 0$. The situation is more complicated for global (homoclinic) bifurcations, or for bifurcation of invariant circles (see section 3.2.2 for the latter).

3.2.1. Bifurcations of fixed points. Consider a local bifurcation $\mathcal{B} \in \mathbb{R}^m$ of fixed points of a $\mathcal{C}^\infty$ map $P : \mathbb{R}^m \to \mathbb{R}^m$, where $\mathcal{B}$ has finite codimension. $\mathcal{B}$ is generic [34, 52] when the linear part and some higher-order jet of P at the point $\mathcal{B}$ satisfy appropriate transversality conditions. If genericity holds, the implicit function theorem implies that $\mathcal{B}$ persists under small perturbations of the map P.

Remark 3.2. Often, it is possible to formulate the above transversality conditions in terms of a normal form of P. One usually requires that a suitable combination $\mathcal{N}$ of the normal form coefficients of P be non-vanishing at $\mathcal{B}$. In this case, a small perturbation will not change the sign of $\mathcal{N}$, nor the local bifurcation diagram around $\mathcal{B}$. Non-vanishing of $\mathcal{N}$ is usually checked by symbolic manipulation of the Taylor series, possibly in combination with numerical methods such as integration of differential equations.

The above conclusion can be applied to the family $\mathcal{P}_{F,G,\epsilon}$, assuming genericity of the bifurcations at $\epsilon = 0$. In fact, genericity holds with the exceptions mentioned in remark 3.3. All saddle-node curves are persistent in ϵ without changes and so is the cusp $\mathcal{C}$. As for the Hopf curves, an important modification introduced by the forcing is the creation of Arnol'd

tongues and strong resonance points. Generic circle dynamics [3, 52] may be either quasi-periodic or phase locked, depending on the rotation number ϱ. In particular, the dynamics is quasi-periodic if and only if ϱ is irrational [25, 34]. Circle dynamics is degenerate for the map $\mathcal{P}_{F,G,\epsilon}$, at $\epsilon = 0$, in the sense that it is a rigid rotation. We recall that a $\mathcal{P}_{F,G,0}$-invariant circle $\mathbb{C}_1$ corresponds to the limit cycle $\mathbb{M}$ of the flow $\Phi_{F,G}$ (see table 2). The rotation number on $\mathbb{C}_1$ is $\varrho = T/T_{\mathrm{L}}$, where T_{L} is the period of the limit cycle $\mathbb{M}$. Regions inside $\mathfrak{M}_0$ where an invariant circle occurs are foliated by lines (hairs) upon which the rotation number ϱ is constant. Each hair $\mathfrak{A}_\varrho$ is attached to a point belonging to the Hopf bifurcation curve where the circle has been created. At such a point, the two complex eigenvalues of the derivative $D\mathcal{P}_{F,G,0}$ are equal to $\exp(\pm 2\pi \mathrm{i}\varrho)$. Points where $\varrho = p/q$ with $q = 1, 2, 3, 4$ are called strong resonances. As ϵ increases from zero, hairs on which $\varrho = p/q$ is rational split into resonance tongues $\mathfrak{A}^{p/q}$. The edges of the tongues have infinite order of contact as ϵ goes to zero [14, 18]. If $q \neq 1, \ldots, 4$, the two edges of $\mathfrak{A}^{p/q}$ meet at a tip attached to a Hopf point with rotation number p/q (also see figure 40). In the case of a strong resonance, the local bifurcation diagram is richer, including also homoclinic bifurcations and chaos. Furthermore, a Hopf curve is interrupted by a generic strong resonance. Examples of some gaps produced on the Hopf curves for $\epsilon = 0.5$ are presented in sections 4.2 and 4.1.

Remark 3.3. At $\epsilon = 0$, all strong resonances introduced on the Hopf curves by the forcing are degenerate (non-generic). Consider a generic point $\mathcal{B} \in \mathcal{H}_1$ at $\epsilon = 0$. Two eigenvalues of the linear part of the vector field (1) are purely imaginary, say, $\mu_\pm = \pm \mathrm{i}\alpha$. Therefore, at $\epsilon = 0$ two eigenvalues of $D\mathcal{P}$ at $\mathcal{B}$ are $\exp(\pm \mathrm{i}T\alpha)$. If $T\alpha = p/q$ with $q = 1, \ldots, 4$, then $\mathcal{B}$ turns into a strong resonance for the map $\mathcal{P}$. Since $\mathcal{B}$ is a generic Hopf bifurcation for the flow of the autonomous system, it does not interrupt the Hopf curve. Furthermore, a unique hair emanates from $\mathcal{B}$ and we conclude that $\mathcal{B}$, considered as a strong resonance of $\mathcal{P}$, is degenerate.

Part of the bifurcation diagram of fixed points of $\mathcal{P}_{F,G,\epsilon}$ for $\epsilon = 0.01$ is shown in figure 15. The saddle-node curve, the Hopf curve, the cusp and the point $\mathcal{HSN}$ are all persistent for this value of ϵ. For concreteness the (F, G, x, y, z) values of this point are, approximately, (1.683 903 22, 1.682 439 88, 1.124 744 27, −0.010 573 55, 0.377 429 16). This can be compared with the corresponding values for $\epsilon = 0$: (1.684 051 72, 1.682 968 55, 1.125, −0.010 380 68, 0.373 704 66) to see that the differences are quite small. However, for $\epsilon = 0.5$ the point $\mathcal{HSN}$ does not persist, and the local bifurcation diagram is quite different (see section 4.3).

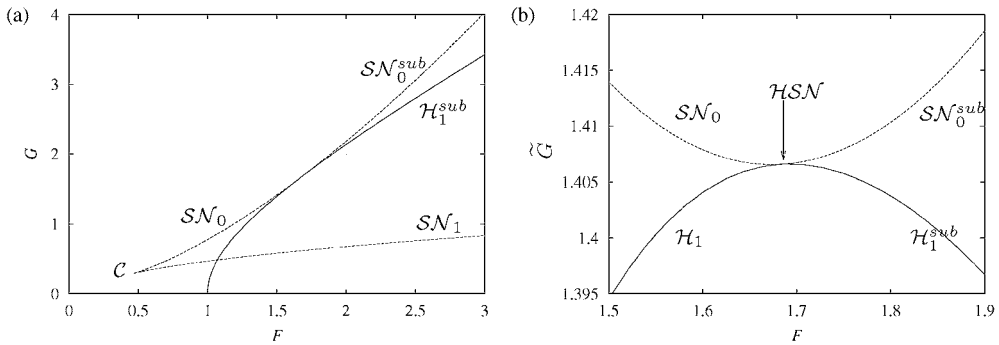

Figure 15. (*a*) Part of the bifurcation diagram of fixed points of $\mathcal{P}_{F,G,0}$, for $\epsilon = 0.01$. (*b*) Magnification of (*a*) of box M around the point $\mathcal{HSN}$. The latter graph has been deformed by an affinity, plotting couples $(F, \tilde{G})$, where $\tilde{G} = G - 1.5 \times (F - 1.5)$).

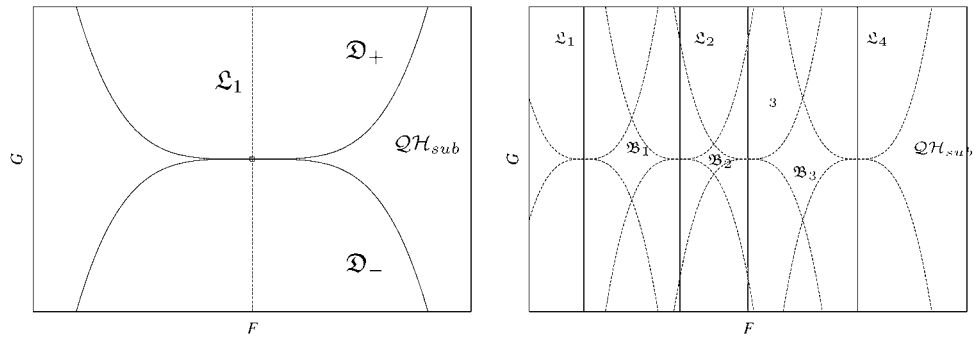

Figure 16. Left: two disks $\mathfrak{D}_+$ and $\mathfrak{D}_-$ are tangent to the curve $\mathcal{QH}_{\text{sub}}$ at the point D. Right: a Cantor subset of the curve $\mathcal{QH}_{\text{sub}}$ persists for $\epsilon > 0$. In the complement of the disks, bubbles (or resonance holes) $\mathfrak{B}_1$, $\mathfrak{B}_2$, and $\mathfrak{B}_3$ appear.

We now turn to homoclinic bifurcations of fixed points. Homoclinic connections of the flow $\Phi_{F,G}$ of system (1) correspond to degenerate homoclinic tangencies for the map $\mathcal{P}_{F,G,0}$. For $\epsilon > 0$, the connections generically break, being replaced by transversal homoclinic intersections and non-degenerate homoclinic tangencies[18]. Special attention must also be payed to the accumulation of transversal homoclinic intersections. Depending on the geometry (e.g. homoclinic orbits in a Shil'nikov-like case) it can be difficult to detect when the first homoclinic tangency is produced.

3.2.2. Bifurcations of invariant circles. We discuss the influence of the forcing on the curves $\mathcal{PD}$, $\mathcal{QH}_{\text{sub}}$ and $\mathcal{QH}_{\text{super}}$ in figure 14. Recall that the first is a curve of period doubling of the limit cycle $\mathbb{M}$, while the second and third are curves of respectively sub- and super-critical Hopf bifurcations of $\mathbb{M}$. For a general presentation of all theory used in this section; see [10, 11] and references therein.

Limit cycles of the flow $\Phi_{F,G}$ of the system (1) turn into $\mathcal{P}_{F,G,0}$-invariant circles, compare table 2 and the previous section. For $\epsilon > 0$, the circles have different bifurcation behaviour, depending on the rotation number ϱ. In brief, the bifurcation diagram is locally persistent in ϵ only when restricting to Diophantine tori. For $\epsilon = 0$ the sets in $\mathfrak{M}_\epsilon$ where Diophantine circles occur locally have the product structure of a curve (of constant rotation number) times a Cantor set (of frequencies). Such local Cantor foliations of the parameter plane intersect the bifurcation curves at Cantor subsets, where the Diophantine circles are normally elliptic. To fix ideas, we briefly describe how the parameter plane $\mathfrak{M}_\epsilon$ looks like for $\epsilon > 0$ close to the curve $\mathcal{QH}_{\text{sub}}$. The circle $\mathbb{C}_1$ is Diophantine on all vertical lines labelled by $\mathfrak{L}_k$ in figure 16 (right). Except at the intersections with $\mathcal{QH}_{\text{sub}}$, the circle $\mathbb{C}_1$ is normally hyperbolic. Then the theory implies that $\mathbb{C}_1$ persists also in two open regions on each side of line $\mathfrak{L}_k$. Two of these regions $\mathfrak{D}_+$ and $\mathfrak{D}_-$, called flat conic discs, are sketched in figure 16 (left). They have an infinite order of tangency with $\mathcal{QH}_{\text{sub}}$. Inside the conic discs $\mathbb{C}_1$ may be resonant and is repelling in $\mathfrak{D}_+$ and attracting in $\mathfrak{D}_-$. The torus repellor $\mathbb{T}$ occurs only in $\mathfrak{D}_-$. Note that the value of ϵ until which a given circle persists, depends strongly on the value of the Diophantine rotation number.

In this way, for $\epsilon > 0$ each of the above curves turns into a frayed boundary as in figure 16 (right). Outside all discs, small resonance regions remain in the parameter plane—the Chenciner 'bubbles', or resonance holes—where the behaviour of $\mathbb{C}_1$ under the perturbation is not predicted by the general theory. On the other hand, the resonance holes might as well

[18] Also called (homoclinic) tangency bifurcations [34, 48].

Table 3. Lyapunov exponents of the repellors in figure 17, see footnote 19.

	λ_1	λ_2	λ_3	e_1	e_2	e_3
A	$-2\cdot$e-6	-0.01867	-0.0187	$1\cdot$e-7	$2\cdot$e-6	$1\cdot$e-6
B	$-2\cdot$e-6	-0.00269	-0.00271	$3\cdot$e-7	$2\cdot$e-6	$1\cdot$e-6
C	$5\cdot$e-5	$4.5\cdot$e-7	-0.01	$6\cdot$e-6	$1\cdot$e-8	$4\cdot$e-6

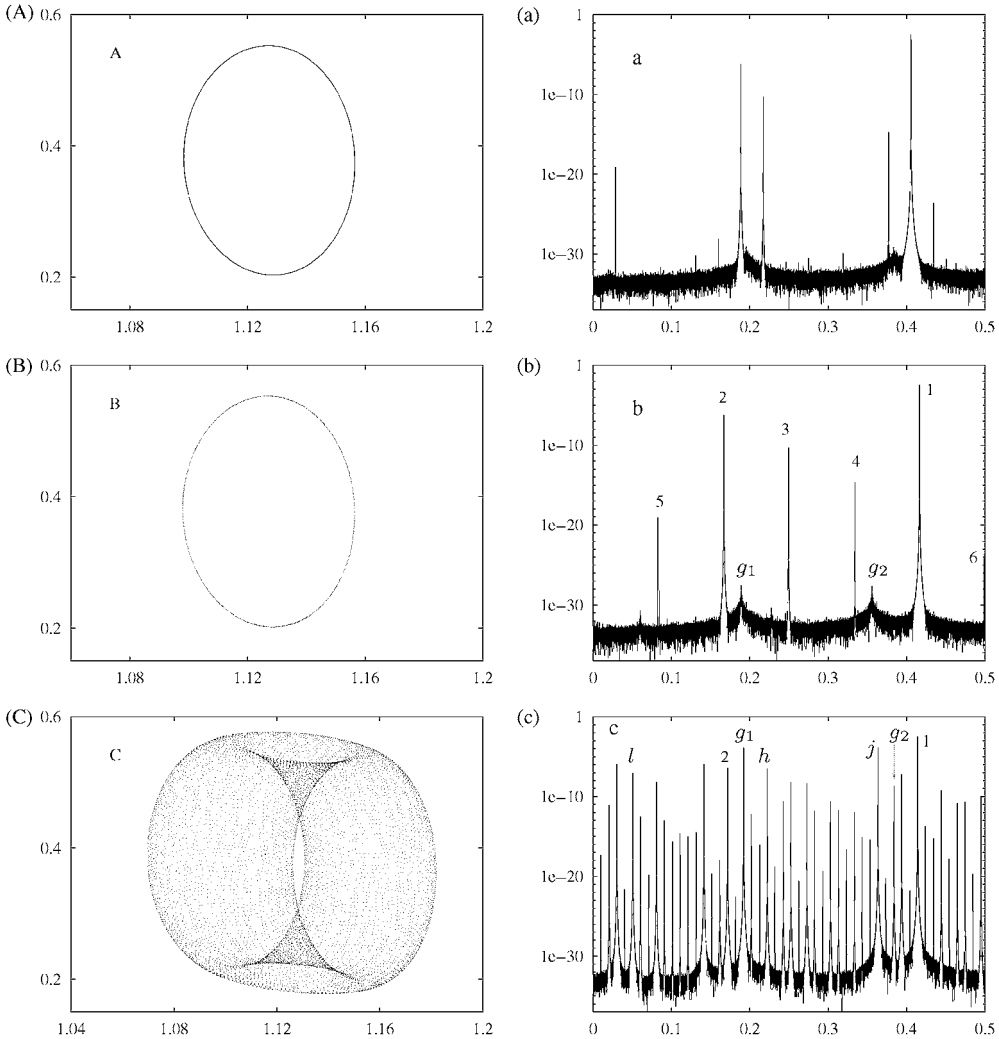

Figure 17. (*A*)–(*C*) Projections on (x, z) of repellors of $\mathcal{P}_{1.8,G,0.01}$, for $G = 1.683$, respectively $G = 1.681$ and $G = 1.68$. The initial point $(x, y, z) = (1.12, -0.17, 0.41)$ has been used in all cases. (*a*)–(*c*) Power spectra of the repellors.

be extremely small in size and, therefore, numerically hard to detect. Apart from these holes, strong resonances locally may destroy the curves.

Persistence of quasi-periodic Hopf bifurcations will be now illustrated by a numerical example. A similar picture for quasi-periodic period doubling is presented in section 4.9.1. For $(F, \epsilon) = (1.8, 0.01)$ fixed, at $G = 1.683$ the circle repellor $\mathbb{C}_1$ occurs (figure 17(*A*)). The

maximal Lyapunov exponent λ_1 (displayed in table 3) is approximately zero, while λ_2 and λ_3 are negative[19], indicating that $\mathbb{C}_1$ is both quasi-periodic and normally hyperbolic. Referring to figure 16 (left), parameter values belong to $\mathfrak{L}_1 \cap \mathfrak{D}_+$.

At $G = 1.681$ (figure 17(*B*)), λ_2 and λ_3 are almost zero and $\mathbb{C}_1$ is normally elliptic. Parameter values are close to $\mathfrak{L}_1 \cap \mathcal{QH}_{\rm sub}$ in figure 16. The power spectrum contains six peaks labelled by k, corresponding to harmonics $f_k = kf_1$ of the fundamental frequency $f_1 = 0.4165$. At $G = 1.68$ the circle has become attracting and coexists with the torus repellor $\mathbb{T}$ (figure 17(*C*)). Parameters belong now to $\mathfrak{L}_1 \cap \mathfrak{D}_-$. Two Lyapunov exponents are zero on $\mathbb{T}$ and the power spectrum confirms the presence of two fundamental frequencies $f_1 = 0.4142$ and $g_1 = 0.191\,95$. Peaks occur at integer combinations of f_1 and g_1. In figure 17(*c*), we labelled peaks on frequencies f_1, $f_2 = 2f_1$, $f_1 - g_1$, $f_1 + g_1$, and $f_3 - g_1$ by 1, 2, h, j, and l, respectively. Notice that very small peaks occur on g_1 and g_1 in figure 17(*b*), before the bifurcation. This is due to intermittency of type II (see [50]).

Similar experiments for other values of F suggest that a large part of $\mathcal{QH}_{\rm sub}$ survives for ϵ small. However, for $\epsilon = 0.5$, no repelling torus is found and therefore the curve $\mathcal{QH}_{\rm sub}$ does not seem to persist. See sections 4.5 and 5.1.3.

4. Dynamical inventory of the map $\mathcal{P}_{F,G}$ for $\epsilon = 0.5$

The structure of the parameter plane $\mathfrak{M}_{0.5}$, sketched in figure 4, is described in the next sections. The bifurcation diagram of fixed points (figure 3) and the scanning for fixed points in figure 2(*b*) will be repeatedly used in mapping out $\mathfrak{M}_{0.5}$. The reader is referred to all the above pictures for the labelling.

The dynamics of the autonomous case $\epsilon = 0$ is preserved in a large part of $\mathfrak{M}_{0.5}$. In region $\mathfrak{F}$, that is either for G large or F small, a fixed point attractor $\mathbb{A}$ exists. Circle dynamics occurs in the two regions $\mathfrak{Q}_1$ and $\mathfrak{Q}_2$. So far, the only changes from the autonomous case are due to resonance phenomena in $\mathfrak{Q}_1$ and $\mathfrak{Q}_2$ and on the boundaries $\mathcal{H}_1$ and $\mathcal{H}_1^{\rm sub}$ (see section 3.2.1). The bifurcation diagram is unchanged also close to curves $\mathcal{SN}_0^{\rm sub}$ and $\mathcal{SN}_0$ for F outside interval $\mathfrak{I} = \{F \mid 1.2 \lessdot F \lessdot 3\}$ (figure 18). However, important modifications occur at $\epsilon = 0.5$:

1. the disappearance of the Hopf-saddle-node point $\mathcal{HSN}$ and the destruction of the Hopf curves inside interval $\mathfrak{I}$ (section 4.3).
2. The disappearance of the frayed curve of quasi-periodic Hopf bifurcations $\mathcal{QH}_{\rm sub}$ (section 4.5).
3. The creation of new families of fixed points close to $\mathcal{SN}_1$, away from the cusp $\mathcal{C}$ (section 4.4). Part of this curve is the boundary between regions $\mathfrak{F}$ and $\mathfrak{U}$, $\mathfrak{U}'$.
4. The growth in size of the chaotic regions $\mathfrak{L}_2$ and $\mathfrak{U}$.
5. The creation of the chaotic ranges $\mathfrak{L}_1$ and $\mathfrak{U}'$.

See section 5.1.3 for comparisons with other values of ϵ. We proceed in order of increasing complexity of the phenomena, starting with region $\mathfrak{Q}_2$, where the situation is fairly well understood.

4.1. Circle dynamics inside region $\mathfrak{Q}_2$

A first indication of circle dynamics is given by the cigar-shaped sequences of attractors in figures 1(*e*) and (*f*). The cigars are projections on the plane (G, y) of one parameter families $\mathbb{C}_2(F_0, G)$ of circles, where F_0 is fixed to 7 and 11, respectively.

[19] Lyapunov exponents of repellors are computed using $\mathcal{P}^{-1}$. All reported values hold for the inverted time.

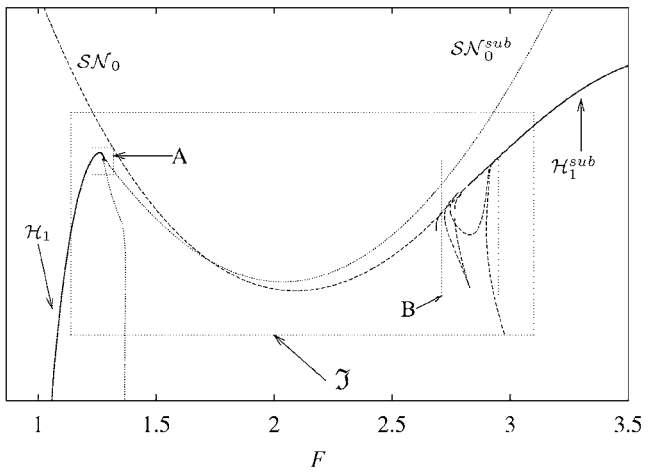

Figure 18. Bifurcation diagram of fixed points of $\mathcal{P}_{F,G}$ for $\epsilon = 0.5$, enlargement of box labelled by A in figure 3. The graph has been affinely deformed, by plotting couples $(F, \tilde{G})$, where $\tilde{G} = (G - 1.3 \times (F - 1))$.

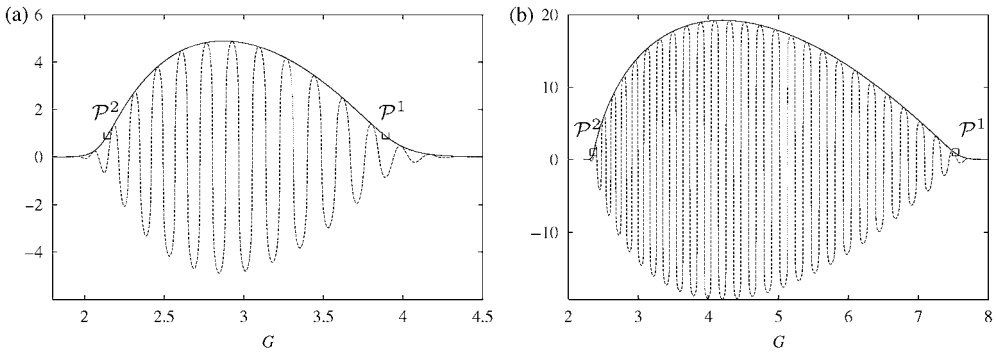

Figure 19. (*a*) Hyperbolic arcsine of the modulus (——) and real part (- - - -) of the eigenvalues of $D\mathcal{P}$ along a curve of continuation of fixed points, for $F = 7$. The two Hopf bifurcations $\mathcal{P}^1$ and $\mathcal{P}^2$ are marked by small boxes, see text for explanation. (*b*) Same as (*a*), for $F = 11$.

The circle $\mathbb{C}_2$ is born at supercritical Hopf bifurcations belonging to curve $\mathcal{H}_2$. To fix ideas, consider figure 1(*e*). The fixed point on the right (G large) is the attractor $\mathbb{A}$. As G decreases, $\mathbb{A}$ loses stability through a supercritical Hopf bifurcation, at a point $\mathcal{P}^1 \in \mathcal{H}_2$. This is illustrated in figure 19(*a*), where we plotted modulus and real part of the complex conjugate eigenvalues μ_1 and μ_2 of $D\mathcal{P}$ along a curve of fixed points. The curve is obtained by numerical continuation, starting from the attractor $\mathbb{A}$ and letting G decrease. The Hopf bifurcation $\mathcal{P}^1$ occurs at $G \simeq 3.89$, where $\mathbb{A}$ turns into a saddle focus $\mathbb{D}$ of type $(1, 2)$. At that moment, $\mathbb{C}_2$ is created and starts expanding off[20]. Then, at $G \simeq 2.14$ the circle $\mathbb{A}$ and the saddle $\mathbb{D}$ collide again, through a Hopf bifurcation $\mathcal{P}^2$, belonging to the inferior branch of $\mathcal{H}_2$. Between $\mathcal{P}^1$ and $\mathcal{P}^2$ the real part of μ_1 on $\mathbb{D}$ changes sign several times, implying that μ_1 and μ_2 rotate around the origin inside the complex plane. The saddle $\mathbb{D}$ does not undergo other bifurcations between $\mathcal{P}^1$ and $\mathcal{P}^2$. For $F = 11$, the G-interval of existence of $\mathbb{C}_2$ and $\mathbb{D}$ is wider, since the

[20] A small scale on the parameter G can be needed to properly visualize this, see remark 4.3.

two Hopf bifurcations occur at $G \simeq 7.53$ and $G \simeq 2.36$. Also notice that $\mathbb{D}$ becomes much more unstable than for $F = 7$, given the larger values of the modulus of the eigenvalues.

We investigated the dynamics on $\mathbb{C}_2$ by computing the Lyapunov exponents. The results for $F = 7$ and $F = 11$ are plotted in figure 20. For all scanned G values between $\mathcal{P}^1$ and $\mathcal{P}^2$, the maximal Lyapunov exponent seems to be zero. Therefore, the dynamics on $\mathbb{C}_2$ is quasi-periodic for most parameter values in the cigars. This is also confirmed by the evolution rotation number of $\mathbb{C}_2$ on the above cigars (figure 21).

For definiteness, consider figure 21(a). Since $F = 7$ is fixed, parameter values belong to a vertical line $\mathfrak{V}$ in the plane $\mathfrak{M}_{0.5}$, intersecting many Arnol'd tongues in $\mathfrak{Q}_2$. The intersections are intervals on $\mathfrak{V}$ where the rotation number ϱ of $\mathbb{C}_2$ is constant. Therefore, each segment of the broken line in figure 21(a) is a devil's staircase [25]. However, all horizontal plateaus, corresponding to intervals of constant rational rotation number, are extremely narrow. For example, intervals where $\varrho = 0$ are intersections of $\mathfrak{V}$ with Arnol'd tongues where $\mathbb{C}_2$ is locked to a fixed point. The first such interval (pointed by an arrow in figure 21(a)) is less than 6×10^{-6} wide. For concreteness, the values of G at the end points of the interval are 2.203 403 047 5 and 2.203 408 996 9, approximately. Similarly, all other Arnol'd tongues are very thin in $\mathfrak{Q}_2$, see below.

We now describe the global organization of the Arnol'd tongues $\mathfrak{A}_k$ with zero rotation number inside $\mathfrak{Q}_2$. The first two tongues, $\mathfrak{A}_{30}$ and $\mathfrak{A}_{31}$, are shown in figure 22(a), together with $\mathcal{H}_2$.

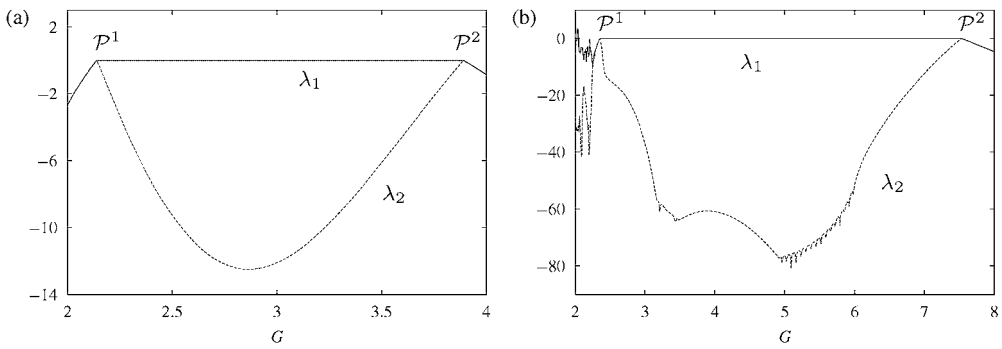

Figure 20. (a) Lyapunov exponents λ_1 and λ_2 in the G interval [2, 4], with $F_0 = 7$. The step in G is 0.01. (b) Same for $G \in [2, 8]$, with $F_0 = 11$.

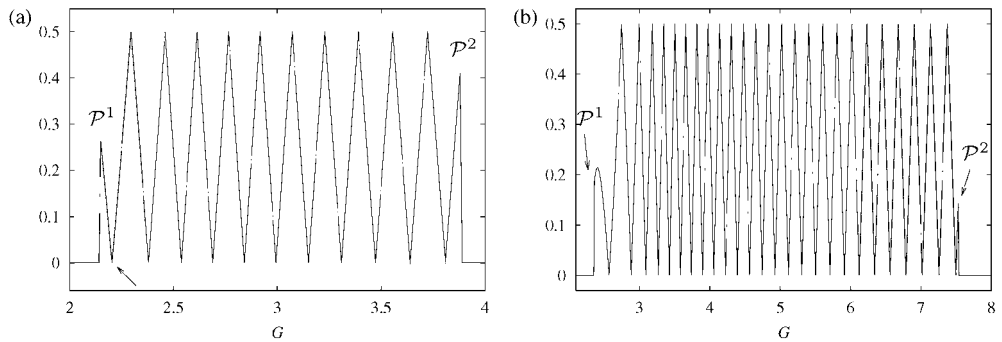

Figure 21. (a), (b) Rotation number ϱ of $\mathbb{C}_2$ on the same G intervals as figure 20(a) and (b), respectively. When the fixed point attractor $\mathbb{A}$ occurs (outside the cigars, thus), we set $\varrho = 0$. The step in G is 0.01.

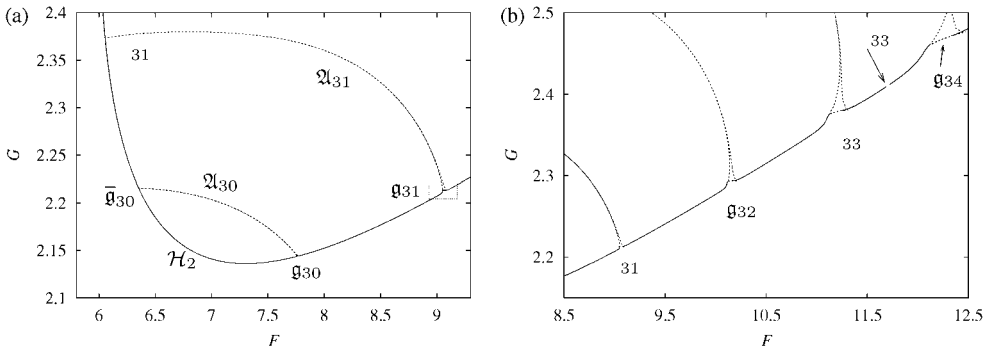

Figure 22. (*a*) Magnification of box C in figure 3. The Hopf curve $\mathcal{H}_2$ is plotted with the first two Arnold tongues of zero rotation number. Magnifications of the boxes around the Bogdanov–Takens gaps $\bar{\mathfrak{g}}_{31}$ and $\mathfrak{g}_{31}$ are given in figure 24(*a*) respectively (*b*). (*b*) Portion of $\mathcal{H}_2$ contained inside box D in figure 3, together with Arnol'd tongues with zero rotation number.

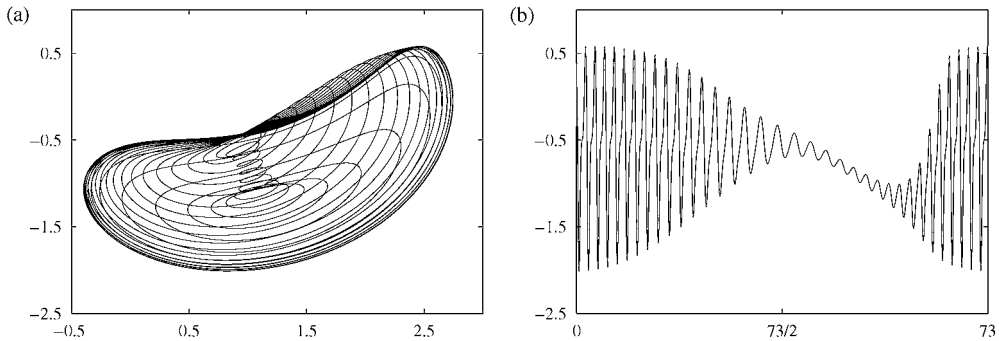

Figure 23. (*a*) Projection on the (y, z) plane of a limit cycle corresponding to a period-one phase-locked circle for parameter values $(F, G) = (9.3, 3.047\,216\,982\,2)$ inside $\mathfrak{A}_{35}$. (*b*) Same as (*a*), projection on the (t, z) plane.

Remark 4.1. The index k in $\mathfrak{A}_k$ is the winding number of the T-periodic limit cycle of $\Phi_{F,G}$ corresponding to the fixed point on the circle inside $\mathfrak{A}_k$. This is illustrated in figure 23(*a*), where a limit cycle with initial condition inside $\mathfrak{A}_{35}$ is shown. An 'inner' and an 'outer' winding can be observed. The time evolution of the z-coordinate is plotted in figure 23(*b*) and the number of maxima in the interval $[0, T]$ gives the winding number 35. The winding number increases by one unit from tongue $\mathfrak{A}_k$ to tongue $\mathfrak{A}_{k+1}$. Furthermore, the size of the inner windings inside tongue $\mathfrak{A}_k$ increases with k: in $\mathfrak{A}_{30}$ it is much smaller than in figure 23(*a*).

Each tongue $\mathfrak{A}_k$ intersects $\mathcal{H}_2$ two times, once at the lower and once at the upper branch. There, the Hopf curve $\mathcal{H}_2$ is interrupted by Bogdanov–Takens gaps, respectively $\mathfrak{g}_k$ and $\bar{\mathfrak{g}}_k$. To fix ideas, we consider the two gaps $\mathfrak{g}_{31}$ and $\bar{\mathfrak{g}}_{31}$ (figures 24(*b*) and (*a*), respectively). The gap $\mathfrak{g}_{31}$ is bounded by two Bogdanov–Takens points $\mathcal{BT}_{31,a}$ and $\mathcal{BT}_{31,b}$ (see figures 24(*c*) and (*d*)). Two saddle-node lines $\mathcal{SN}_{31,a}$ and $\mathcal{SN}_{31,b}$ are tangent to $\mathcal{H}_2$ at respectively $\mathcal{BT}_{31,a}$ and $\mathcal{BT}_{31,b}$. Furthermore, $\mathcal{SN}_{31,a}$ meets $\mathcal{SN}_{31}$ at a cusp $\mathcal{C}_{31,a}$ and $\mathcal{SN}_{31,b}$ meets $\mathcal{SN}_{31}$ at a cusp $\mathcal{C}_{31,b}$. The cusps $\mathcal{C}_{31,a}$ and $\mathcal{C}_{31,b}$ are connected by the saddle-node curve $\mathcal{SN}_{31,ab}$.

This structure is repeated at $\bar{\mathfrak{g}}_{31}$, at the other side of $\mathfrak{A}_{31}$, but the scale is much smaller (figure 24(*a*)). Two Bogdanov–Takens points and two cusps are connected by a fourth branch of saddle-node bifurcations, denoted by $\mathcal{SN}_{31,ba}$. The four saddle-node lines thus bound the tongue $\mathfrak{A}_{31}$.

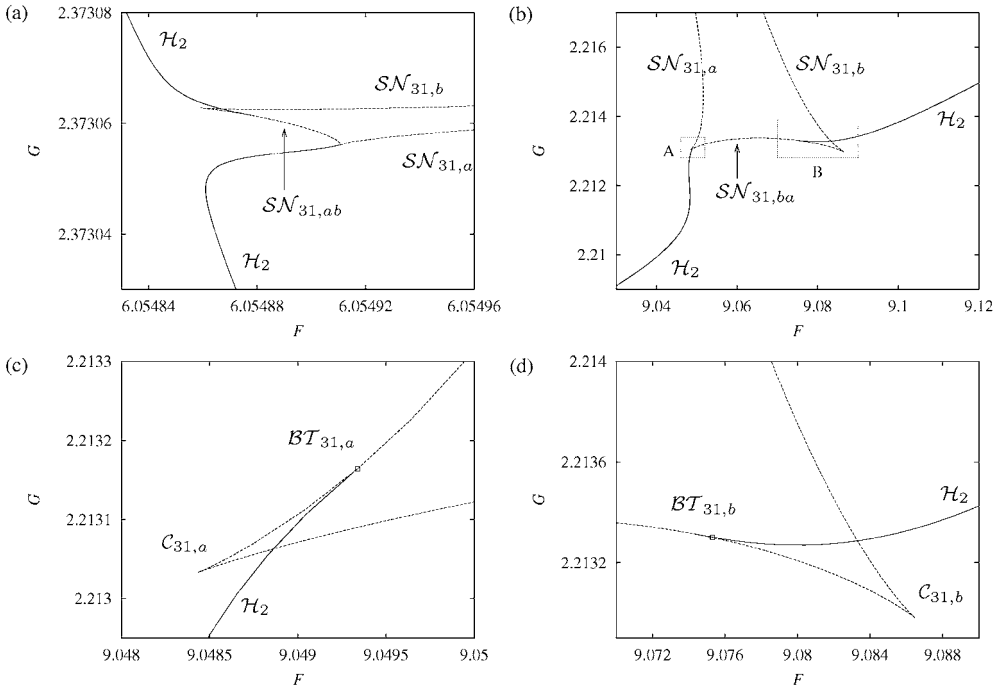

Figure 24. (*a*) Resonance gap $\bar{\mathfrak{g}}_{31}$ in the Hopf line $\mathcal{H}_2$. The dashed lines lines are saddle-node bifurcation curves. (*b*) Resonance gap $\mathfrak{g}_{31}$. (*c*), (*d*) Magnification of boxes L and M in (*b*), at the tangencies between $\mathcal{H}_2$ and the saddle-node curves.

The same global structure seems to exist close to all other Bogdanov–Takens gaps in $\mathcal{H}_2$. Each gap $\mathfrak{g}_k$ on the lower branch of $\mathcal{H}_2$ is connected to a gap $\bar{\mathfrak{g}}_k$ on the upper branch by an Arnol'd tongue $\mathfrak{A}_k$ of rotation number zero. These tongues are plotted in figure 2(*a*), where they appear as lines crossing $\mathfrak{Q}_2$. Indeed, they are extremely narrow for most parameter values in $\mathfrak{Q}_2$. Arnol'd tongues of higher period are even narrower, so that the circle $\mathbb{C}_2$ is found quasi-periodic for most values inside $\mathfrak{Q}_2$. However, the tongues become wider close to the gaps $\mathfrak{g}_{31}$, at the lower branch of $\mathcal{H}_2$. Indeed, $\mathfrak{A}_{32}$ and $\mathfrak{A}_{33}$ form two small black spikes in figure 2(*b*), near the lower boundary of region $\mathfrak{Q}_2$. These spikes become even wider for larger ϵ, so that $\mathcal{H}_2$ is destroyed by strong resonance gaps, see section 5.1.3.

More resonance gaps interrupting the continuity of $\mathcal{H}_2$ are shown in figure 22(*b*). The first three from the left and that at the right are Bogdanov–Takens gaps, while the second from right, labelled $\mathfrak{h}_{33}$, is due to a $1:2$ resonance. The size of the gaps increases with F and on the lower branch of $\mathcal{H}_2$ it is much larger than on the upper one.

Remark 4.2. In the parameter space $\mathfrak{M}$ two curves of Bogdanov–Takens bifurcations pass through the two extremes of each gap. Both curves emanate from the same degenerate Bogdanov–Takens point on the curve $\mathcal{H}$ at $\epsilon = 0$, compare remark 3.3.

As we have shown, plenty of resonance gaps occur on $\mathcal{H}_2$ (the same holds for $\mathcal{H}_1$, see section 4.3). It is known from the theory [34, 40] that the bifurcation diagram in the neighbourhood of such codimension two points is rich, involving global homoclinic bifurcations, regions of chaoticity and homoclinic intersections. Such phenomena have been detected in [39], although using a smaller forcing period T. It is likely that they occur also in the family $\mathcal{P}_{F,G}$, see section 5.2.

4.2. Circle dynamics in $\mathfrak{Q}_1$

The circle $\mathbb{C}_1$ is born at Hopf points on the curve $\mathcal{H}_1$. This is illustrated in figures 25 and 26, produced by a similar algorithm as figure 1, with G fixed. The fixed point attractor $\mathbb{A}$ occurs for small F (left part of the figures). Crossing $\mathcal{H}_1$ from left to right, $\mathbb{A}$ undergoes a supercritical Hopf bifurcation at $F = 1.013$, where $\mathbb{C}_1$ appears.

Remark 4.3. If a Hopf bifurcation occurs at F_0 and the invariant circle exists for $F > F_0$, then the radius of the circle is $\mathcal{O}(\sqrt{F - F_0})$ as F tends to F_0 [34,40]. In the family $\mathcal{P}_{F,G}$, the interval of F usually has to be taken rather small to see this asymptotics, still visible in figure 26(b). On larger intervals, the expansion of the circle may look quite 'explosive' (cf figures 25 (left), 26(a), and 43 later on). The same holds for Hopf bifurcations at the border of $\mathfrak{Q}_2$, compare the extremes of the 'cigars' $\mathbb{C}_2(7, G)$ and $\mathbb{C}_2(11, G)$ in figures 1(e) and (f).

In figures 25 and 26, all attractors occurring for $F > 1.1$ are projections of $\mathbb{C}_1(F, G_0)$, with $G_0 = 0.2$. Also compare figures 1(c)–(f) for G small. Right after the Hopf bifurcation, for $1 \lessdot F \lessdot 2$, the size and form of $\mathbb{C}_1$ are quite sensitive to variations of G, also see figure 26.

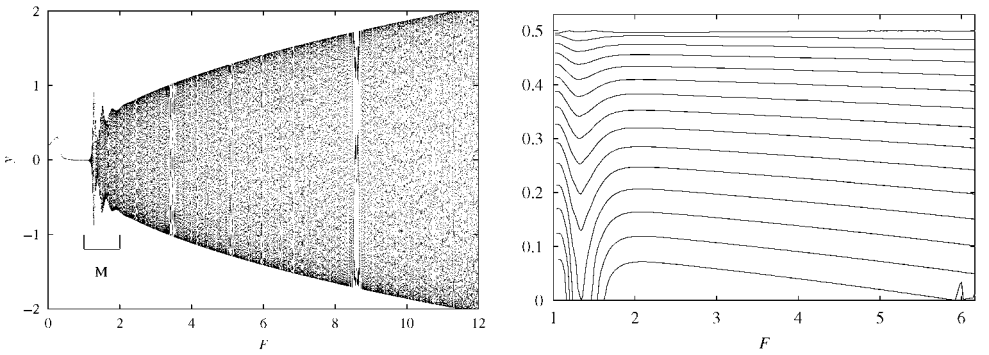

Figure 25. Left: projections on the y-axis of $\mathcal{P}$-attractors as a function of F for $G = 0.2$ fixed. F is increased with a step of 0.02. The last 100 points of each loop are plotted. Interval M is enlarged in figure 26. Right: rotation number (modulo $1/2$, see appendix A.3) as a function of F. Each curve corresponds to a fixed value of G: $G = 0.36$ for the lowest and $G = 0.08$ for the upmost. Between two curves, G differs of 0.02.

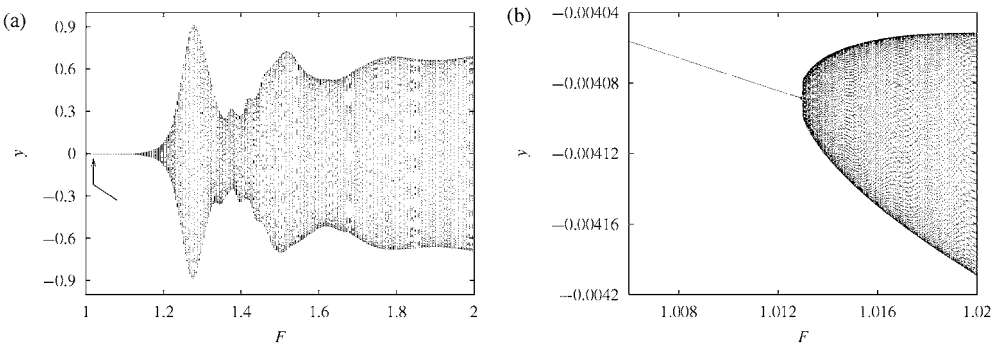

Figure 26. (a) Magnification of interval M in figure 25. Between consecutive loops of iterates, F is increased with a step of 0.004. (b) Magnification of a small interval pointed by an arrow in (a), where F is increased with a step of 3.5×10^{-5}. The last 100 points of each loop are plotted.

For larger G, this phenomenon becomes more evident and, ultimately, inside region $\mathfrak{L}_1$ the circle $\mathbb{C}_1$ breaks (see figure 43).

All Arnol'd tongues emanating from $\mathcal{H}_1$ are very thin and lie more or less parallel to the $G = 0$ axis. This is illustrated by a plot of the rotation number ϱ as a function of F (figure 25, right), computed on sequences of circles such as in figure 25 (left) for a few fixed values of G. The lowest lines $G = 0.36$, 0.34, and 0.32 intersect the large period-one tongue $\mathfrak{A}_1$ in figure 2(b). There ϱ is zero and this also influences the other curves in figure 25 (right). The small peak in ϱ for $G = 0.36$ and F close to 6 is due to a quasi-periodic doubling of $\mathbb{C}_2$, followed by an undoubling. However, far from this peak and away from $\mathfrak{A}_1$ the rotation number changes quite slowly with F.

4.3. Disappearance of the Hopf-saddle-node point $\mathcal{HSN}$

For $\epsilon = 0.01$, the curves $\mathcal{SN}_0$ and $\mathcal{SN}_0^{\text{sub}}$ in fact form one curve, split by the point $\mathcal{HSN}$ (figure 15). On $\mathcal{SN}_0^{\text{sub}}$ a fixed point repellor $\mathbb{R}$ and a saddle $\mathbb{B}_1$ of type (1, 2) are generated. Crossing $\mathcal{H}_1^{\text{sub}}$ from left to right, the fixed point repellor $\mathbb{R}$ turns into a saddle $\mathbb{B}_2$ of type (2, 1), while a circle repellor $\mathbb{C}_1$ is born (also see figures 36 and 35 later on).

For $\epsilon = 0.5$, $\mathcal{SN}_0^{\text{sub}}$ and $\mathcal{SN}_0$ do not meet and the point $\mathcal{HSN}$ has disappeared (figure 18). Most of the changes occur inside interval $\mathfrak{I}$ (this is where $\mathcal{HSN}$ occurs at $\epsilon = 0.01$). The Hopf curves $\mathcal{H}_1$ and $\mathcal{H}_1^{\text{sub}}$ are broken to small fragments by many strong resonance points.

Three 1 : 2 resonance points and one Bogdanov–Takens on $\mathcal{H}_1$ are plotted in figure 27(a). Another Bogdanov–Takens point can be seen in figure 27(b). At these Bogdanov–Takens points, $\mathcal{SN}_0^{\text{sub}}$ is tangent to $\mathcal{H}_1$. For larger F, the resonance gaps increase even more in size and only minuscule segments of $\mathcal{H}_1$ survive inside $\mathfrak{I}$.

Remark 4.4. A Hopf curve in general can be continued across strong resonance gaps. Indeed, curves of fixed points emanate from such points, on which two eigenvalues μ_1 and μ_2 of $D\mathcal{P}$ are real, with $\mu_1\mu_2 = 1$. This is not a bifurcation condition, see [40]. For reference, such curves are plotted by dots in figures 27 and 28.

We also want to stress that the curve $\mathcal{H}_1^{\text{sub}}$ is completely broken by strong resonances inside interval $\mathfrak{I}$. In figure 28, $\mathcal{H}_1^{\text{sub}}$ is interrupted by two 1 : 2 resonance points and three Bogdanov–Takens points, two of which are shown in figure 28(b), the other is not marked. The curve $\mathcal{SN}_0$ meets five cusps (two are shown in figure 28(b), one is not marked) and is tangent to $\mathcal{H}_1^{\text{sub}}$ at the Bogdanov–Takens points.

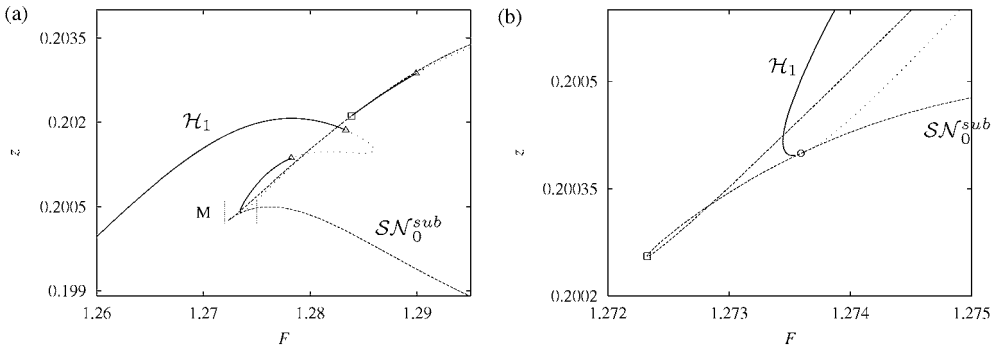

Figure 27. (a) Projection on (F, z) of portions of $\mathcal{H}_1$ (——) and $\mathcal{SN}_0^{\text{sub}}$ (- - - -), enlargement of box A in figure 18. (b) Magnification of box M in (a). Bogdanov–Takens points are marked by small boxes, 1 : 2 resonance points by triangles and cusps by circles.

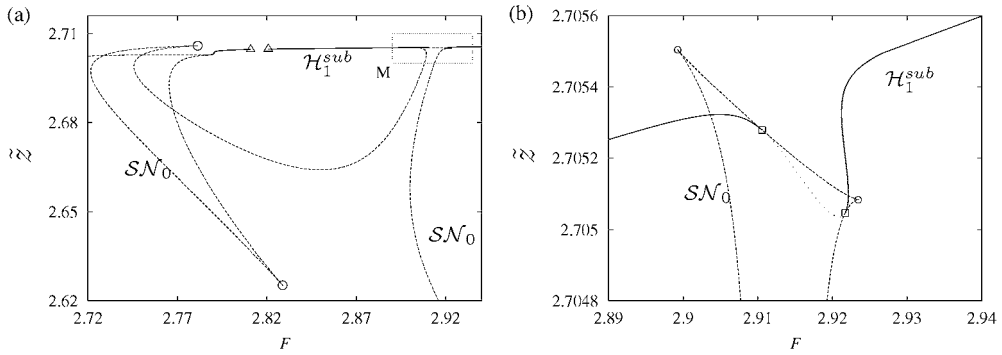

Figure 28. (*a*) Projection on $(F, \tilde{z})$ of portions of $\mathcal{H}_1^{\rm sub}$ (——) and $\mathcal{SN}_0$ (- - - -), enlargement of box B in figure 18. The graph has been affinely deformed by plotting $\tilde{z}(F, z) = (z - 1.46 \times (F - 2.7))$ on the vertical axis. (*b*) Magnification of box M in (*a*). Symbols mean the same as in figure 27.

Since $\mathcal{HSN}$ persists at $\epsilon = 0.01$ (section 3.2.1), it must have disappeared through a higher-codimension bifurcation at some intermediate ϵ before reaching $\epsilon = 0.5$, see section 5.1.3.

4.4. New families of fixed points in the chaotic range $\mathfrak{U}'$

It can be guessed from figures 2(*b*) and 5 (right) that new families of fixed point attractors are created below curve $\mathcal{SN}_1$ in region $\mathfrak{U}'$. In this section we provide an explanation of how these families are connected to the fixed point attractor occurring in region $\mathfrak{F}$.

The curves $\mathcal{SN}_0$ and $\mathcal{SN}_1$ of saddle-node bifurcations meet tangentially at $\mathcal{C}$, forming a tongue-shaped region (see figure 5 (left)). Close to $\mathcal{C}$, the dynamics of $\mathcal{P}$ for $\epsilon = 0.5$ is quite similar to that of the autonomous case $\epsilon = 0$. A fixed point attractor and a saddle are generated on both curves when (F, G) enter the tongue. This is illustrated in figure 29, where a curve K of fixed points is plotted. For G large, the fixed point attractor $\mathbb{A}_1$ is detected by iteration and continued for G decreasing. Arrows indicate the sense in which the curve is described. As G decreases, K becomes almost vertical (see figure 29(*a*), above box M). A magnification of box M (see figure 29(*b*)) shows that K meets a saddle-node point $\mathcal{T}_1$, belonging to $\mathcal{SN}_1$, where $\mathbb{A}_1$ turns into a saddle $\mathbb{B}_1$ of type (2, 1). The branch of saddles makes an excursion at the right and meets a saddle-node point $\mathcal{T}_0$, belonging to $\mathcal{SN}_0$. Here, $\mathbb{B}_1$ collides with the attractor $\mathbb{A}_2$ and the branch of $\mathbb{A}_2$ extends down to $G = 0$. Notice that the latter saddle-node bifurcation clarifies the transition from figure 1(*a*) to figure 1(*b*). To visualize this, the points found in figure 1(*b*) are plotted together with the continuation curve in figure 29(*a*). In figure 1(*b*), G is increased by 0.01 at each step. When G is increased across $\mathcal{T}_0$, the attractor $\mathbb{A}_2$ disappears at $\mathcal{T}_0$, and the $\mathcal{P}$-iterates are attracted to $\mathbb{A}_1$. So $\mathbb{A}_1$ and $\mathbb{A}_2$ coexist in the G-interval between $\mathcal{T}_0$ and $\mathcal{T}_1$. Consequently, a part of the tongue with tip at $\mathcal{C}$ is a region of bistability. For (F, G) at the left of curve $\mathcal{H}_1$, two fixed point attractors $\mathbb{A}_1$ and $\mathbb{A}_2$ coexist with the saddle $\mathbb{B}_2$. In fact, all of them belong to a unique surface of fixed points, partitioned by the saddle-node curves $\mathcal{SN}_0$ and $\mathcal{SN}_1$. Outside the tongue or at the right of $\mathcal{H}_1$, only one fixed point attractor possibly occurs and will be denoted by $\mathbb{A}$. For example, $\mathbb{A}$ is detected for low values of F, see figure 1(*a*). At the right of $\mathcal{H}_1$, the fixed point $\mathbb{A}$ may coexist with the circle attractor $\mathbb{C}_1$, but also with a SA; see section 4.6.

For larger values of F the bifurcation diagram close to $\mathcal{SN}_1$ is more complicated than in the autonomous case. Many more fixed points appear here as F is increased. This is illustrated

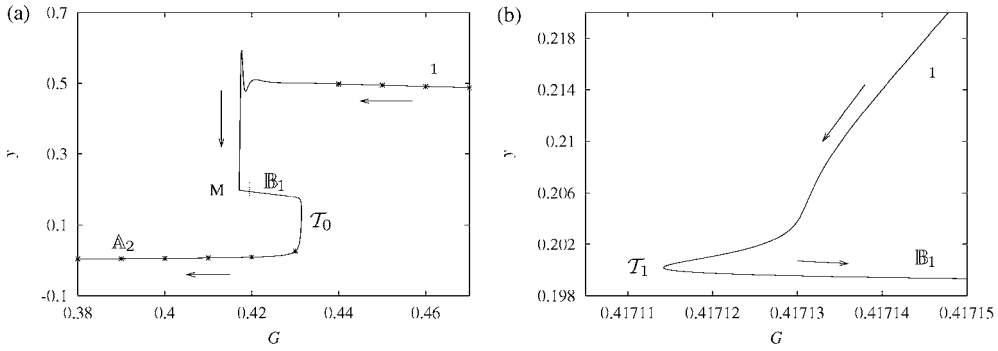

Figure 29. (*a*) Projection on (G, y) of curve of $\mathcal{P}$-fixed points, joining the attractors $\mathbb{A}_1$ and $\mathbb{A}_2$, for $F = 0.7$. The curve is computed by numerical continuation. Crosses mark the fixed points found in figure 1(*b*). (*b*) Magnification of box marked by M in (*a*).

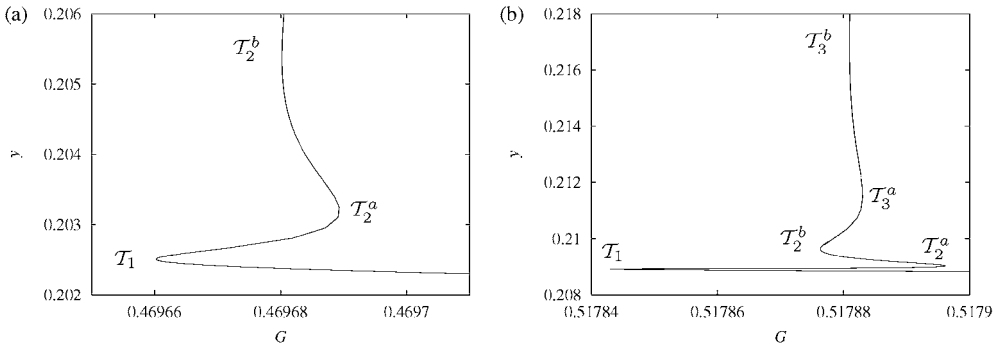

Figure 30. (*a*) Projection on (G, y) of a curve of fixed points of $\mathcal{P}$ obtained by continuation with respect to G, for $F = 0.8$. (*b*) Same as (*a*) for $F = 0.9$.

in figure 30, similar to figure 29(*b*), but with $F = 0.8$. The point $\mathcal{T}_1$ again belongs to $\mathcal{SN}_1$. Two 'new' saddle-node bifurcation points $\mathcal{T}_2^{\mathrm{a}}$ and $\mathcal{T}_2^{\mathrm{b}}$ are detected close to $\mathcal{T}_1$. Denoting by G_a and G_b the values of G at which these two points occur, four fixed points coexist[21] in the interval (G_a, G_b). For $F = 0.9$, four new saddle-node bifurcations occur, denoted by $\mathcal{T}_2^{\mathrm{a}}$, $\mathcal{T}_2^{\mathrm{b}}$, $\mathcal{T}_3^{\mathrm{a}}$, and $\mathcal{T}_3^{\mathrm{b}}$ (figure 30(*b*)). For G in a suitably small interval, $\mathcal{P}$ has up to six coexisting fixed points. The new bifurcations belong to curves emanating from a sequence of cusps, which possibly form a cascade, compare [16]. In figure 31, we plotted the cusp $\mathcal{C}$ and the curves $\mathcal{SN}_0$ and $\mathcal{SN}_1$, together with eight curves $\mathcal{SN}_k^{\mathrm{a}}$ and $\mathcal{SN}_k^{\mathrm{b}}$, $k = 2, \ldots, 5$, of saddle-node bifurcations of fixed points. The points $\mathcal{T}_k^{\mathrm{a}}$ and $\mathcal{T}_k^{\mathrm{b}}$ belong to $\mathcal{SN}_k^{\mathrm{a}}$ and $\mathcal{SN}_k^{\mathrm{b}}$, which in turn emanate from a cusp $\mathcal{C}^k$. The projection on the (F, y) plane has been chosen to better distinguish the curves $\mathcal{SN}^k$. Indeed, in the (F, G) plane they all lie in a very narrow strip above the curve $\mathcal{SN}_1$.

We observe that a Shil'nikov tangency bifurcation might be related to the occurrence of the cusps and the coexistence of the several SN lines. A trace of this can be seen in the spiral-like form of the limit cycles of $\Psi_{F,G,0.5}$ (corresponding to periodic points of $\mathcal{P}$). For the limit cycle in figure 32(*a*), the winding number (see section 4.1) is four (the fourth winding is quite narrow), while it is zero for the limit cycle in figure 32(*b*). At each curve $\mathcal{SN}^{k+1,a}$ or $\mathcal{SN}^{k+1,b}$,

[21] In fact, the vertical line $G = 0.469\,685$ intersects the curve in figure 30(*a*) at four points.

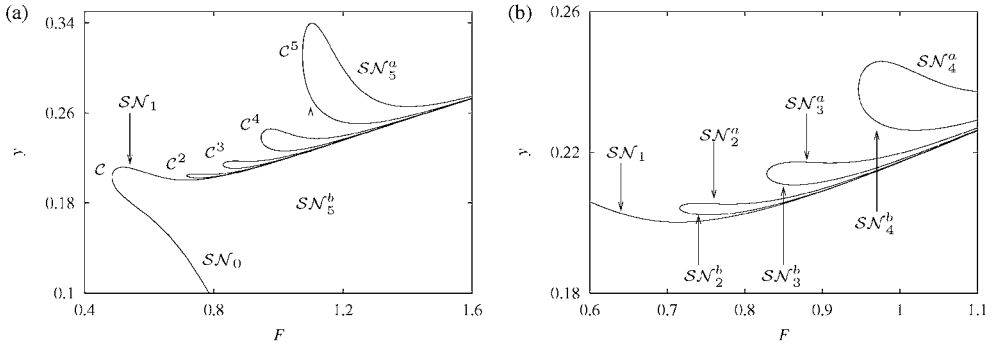

Figure 31. (*a*) Projection on (F, y) of curves of saddle-node bifurcation points. Four cusps are marked by $\mathcal{C}^k$, $k = 2, \ldots, 5$, while $\mathcal{C}$ is the same as in figure 3. (*b*) Enlargement of the previous picture around the first three cusps $\mathcal{C}^k$.

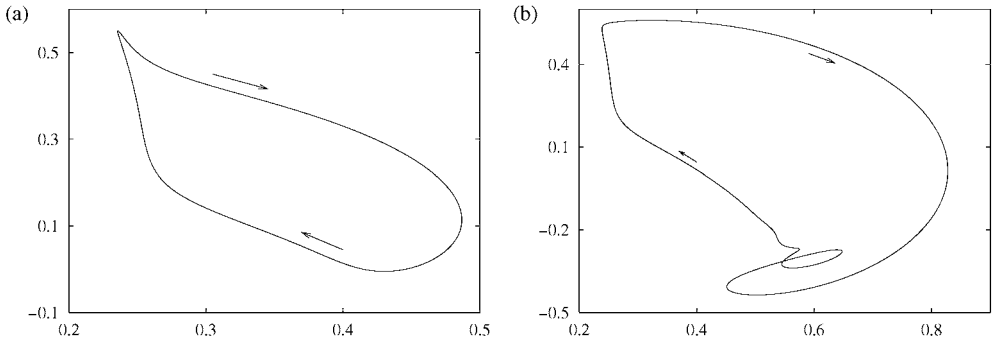

Figure 32. (*a*) Projection on (y, z) of a limit cycle of the flow $\Psi_{F,G,0.5}$ of system (2), for $(F, G) \simeq (1.2, 0.64)$. The corresponding fixed point belongs to curve $\mathcal{SN}^5$. (*b*) Same as (*a*), but the fixed point belongs to $\mathcal{SN}_1$.

a spiral limit cycle is created possessing one more revolution than on $\mathcal{SN}^{k,\mathrm{a}}$ or $\mathcal{SN}^{k,\mathrm{b}}$, thus with winding number increased by one.

For F larger, inside regions $\mathfrak{U}'$ and $\mathfrak{U}$ one finds orbits with an 'inner' and an 'outer' spiralling (figure 11(*a*) in section 1.3), or displaying even more complicated patterns (figure 11(*b*)). Furthermore, new families of fixed point attractors appear in $\mathfrak{U}'$ and $\mathfrak{U}$. We illustrate this in figure 33(*a*), with a plot of a curve K of fixed points in $\mathfrak{U}'$. For better visualization, two parts of K are plotted with different linestyles. A magnification of a horizontal layer marked by L is given in figure 33(*c*). The arrows indicate the direction we are following in the description. The curve K is obtained as figure 29, by taking $\mathbb{A}_1$ and doing continuation for G decreasing (arrow 1 in figures 33(*a*) and (*c*)). The curve begins to oscillate inside a small G-interval M1, magnified in figure 33(*b*). Each turning point is a saddle-node bifurcation (this holds for all pictures). At first the oscillations occur in a very narrow G-interval and can be seen only with a further magnification (box B in figures 33(*b*), where six SN bifurcations occur). Then, as y decreases (arrow 2 in figures 33(*a*)–(*c*)), the oscillations tend to become wider in G and flatter in y, accumulating at the lowest branch of K. After 15 SN bifurcations, K makes a long excursion towards a saddle-node point[22] occurring for larger G, and then turns back (arrow 3 in figures 33(*b*) and (*c*)).

[22] For a clear visualization we exclude the latter point from figures 33(*a*)–(*d*), just focusing on a small interval in G.

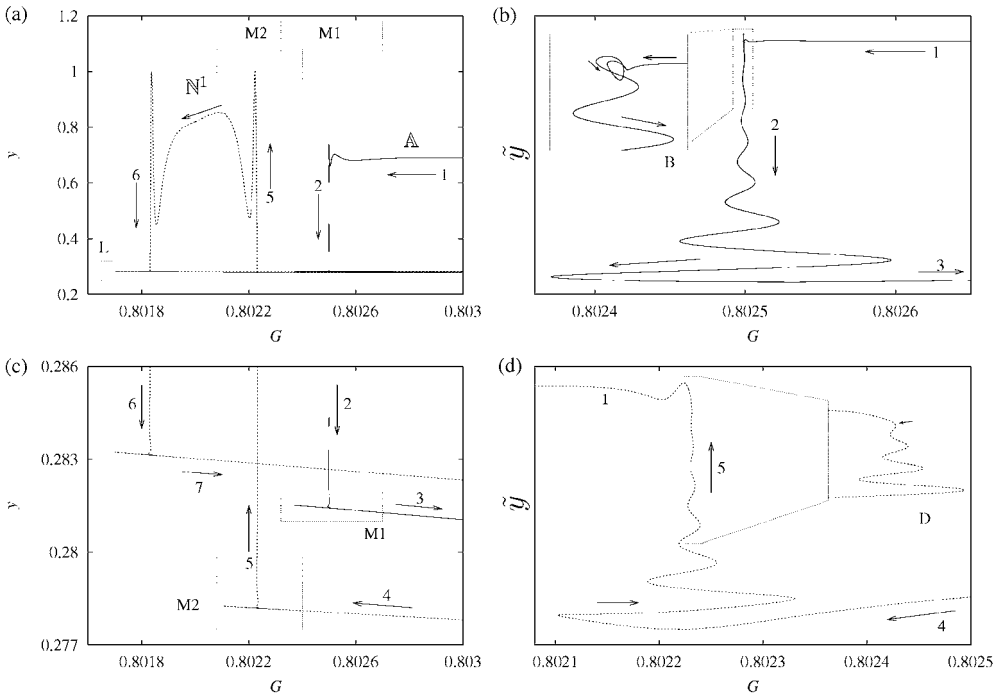

Figure 33. (*a*) A curve K of fixed points, obtained by continuation (see text). (*c*) Magnification of a horizontal layer L of (*a*). (*b*), (*d*) Magnifications of portions of K for G in the intervals M1 and M2, respectively. For better visualization, only one part of K is plotted in each. A nonlinear transformation has been applied to distinguish the oscillations of K, which are not visible in (*a*) nor in (*c*).

On the branch which is coming back (dashed curve under arrow 4 in figures 33(*c*) and (*d*)) the fixed points are saddles. Furthermore, this branch does not reach $G = 0$, but meets another turning point (in box M2 magnified in figure 33(*d*)) and begins to oscillate again. This time, after the first turning point, K goes upwards (arrow 5 in figures 33(*a*), (*c*), and (*d*)). After eleven SN bifurcations (the last is marked by a dashed arrow in box D, figure 33(*d*)), the fixed points on K become attracting. These attractors occur in a small G interval, labelled by $\mathbb{N}^1$ in figure 33(*a*). This interval is roughly bounded by the two 'vertical barriers' close to arrows 5 and 6. As G decreases (arrows 6), the curve K again meets several SN bifurcations. After that, a branch of saddles again makes an excursion to a saddle-node point occurring for larger G (arrow 7 in figure 33(*c*)).

The whole process repeats itself for G smaller. By further continuation of K, we have found eight new branches $\mathbb{N}^k$ of attracting fixed points (figure 34(*a*)). Each of the new branches is bounded by two 'vertical barriers', where several saddle-node bifurcations occur. On each 'vertical barrier' the continuation curve oscillates as in figures 33(*b*) or (*d*). Therefore, for each G value in figure 34(*b*), many fixed points coexist, most of them being saddles. The corresponding T-periodic limit cycles of $\Psi_{F,G,0.5}$ are of spiral type.

It is natural to suspect that Shil'nikov tangency bifurcations may take place here. In fact, narrow Hénon-like SA are found nearby in $\mathfrak{U}'$, see section 4.6. In the autonomous system $\epsilon = 0$ one curve of Shil'nikov bifurcations is tangent to the curve $\mathcal{SN}_1$ at several codimension two points. The organizing centre for the phenomena described in this section could be one of such codimension two bifurcations of fixed points of $\mathcal{P}_{F,G}$.

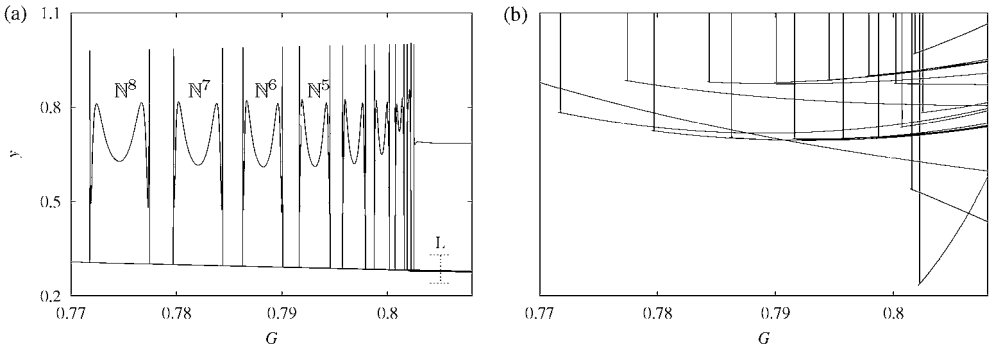

Figure 34. (*a*) A larger portion K (see text). (*b*) Magnification of a thin horizontal layer labelled by L in (*a*), showing coexistence of a lot of different branches of saddle fixed points.

4.5. Disappearance of quasi-periodic Hopf bifurcations

For $\epsilon = 0$ (figure 3), the repelling circle $\mathbb{C}_1$ loses stability at quasi-periodic Hopf bifurcations belonging to the curve $\mathcal{QH}_{\text{sub}}$ (section 3.2.2).

For $\epsilon = 0.5$, numerical experiments reveal that $\mathbb{C}_1$ persists both for G small and for G large and is attracting in the former and repelling in the latter case. We recall that the attractor $\mathbb{C}_1$ is born at the Hopf curve $\mathcal{H}_1$, while the repellor $\mathbb{C}_1$ at the subcritical Hopf curve $\mathcal{H}_1^{\text{sub}}$ (sections 4.2 and 4.3). Thus at $\epsilon = 0.5$ there appear gaps in the parameter plane where $\mathbb{C}_1$ does not persist, being replaced by strange attractors or repellors, or by nothing at all (in the latter case, by iteration only the fixed point $\mathbb{A}$ is detected). These gaps are roughly located around the position where the frayed curve $\mathcal{QH}_{\text{sub}}$ (section 3.2.2) is expected to intersect the current line $F = \text{const}$ inside $\mathfrak{M}_\epsilon$. We illustrate this by means of iteration to an attractor or repellor for $F = 5$ fixed, in figure 35. The left part $G < 1.5$ is just a different projection of figure 1(*d*). The attracting fixed point $\mathbb{A}$, however, is represented also for larger G. In the right upper part ($G > 2$ and $z > -1$), $\mathcal{P}$-repellors are plotted. The algorithm is the same as usual, but this time G is decreased and $\mathcal{P}^{-1}$ is iterated, to detect repellors. This way we perform a rough continuation scheme, for more accurate methods see appendix A.1.

To begin, the fixed point repellor $\mathbb{R}$ is found at $G = 6$. As G decreases, $\mathbb{R}$ undergoes a Hopf bifurcation at $G \simeq 5.71$, at a point belonging to curve $\mathcal{H}_1^{\text{sub}}$ in figure 3. The circle repellor $\mathbb{C}_1$ persists down to $G \simeq 2.13$ (marked by an arrow in figure 35), where it undergoes one quasi-periodic period doubling. A circle repellor $2\mathbb{C}_1$ is created, persisting down to $G \simeq 2.01$. At $G = 2$ one finds a strange repellor, but no repelling invariant set is found for smaller G.

At the other side of figure 35, the circle attractor $\mathbb{C}_1$ is found at $G = 0$. Increasing G, the circle persists up to $G \simeq 0.65$ (marked by an arrow). SAs are detected for $0.66 \lessapprox G \lessapprox 1.3$, now and then replaced by windows of periodicity. For $G \gtrsim 1.3$, the fixed point $\mathbb{A}$ is the unique attractor. No invariant circle (either attracting or repelling) is detected for $G \in (0.66, 2)$. However, an invariant circle of saddle type might persist in this gap (at least for most of the G values), thereby providing the 'link' between circle attractor and repellor.

The size of these gaps is not as large for other values of F. For $F = 4$, the circle $\mathbb{C}_1$ seems to exist for all values of G between 0 and 4.51, thus forming a one parameter family $\mathbb{C}_1(F_0, G)$ with $F_0 = 4$. This is illustrated in figure 36 left, where we plotted attractors and repellors of $\mathcal{P}$. The invariant set projected in the cigar-shaped region is the circle $\mathbb{C}_1$. For $G < 1.615$ (marked by an arrow), $\mathbb{C}_1$ is attracting and has been detected as for figure 1. For $G > 1.615$, $\mathbb{C}_1$ is repelling and has been obtained as for figure 35, using the inverse of $\mathcal{P}$ and letting G

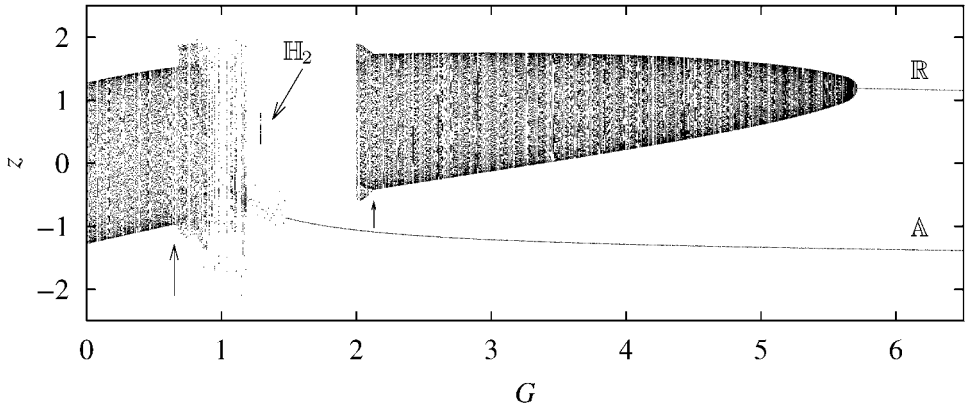

Figure 35. Projection on (G, z) of sequences of repellors and attractors of $\mathcal{P}$ for $F = 5$ and $\epsilon = 0.5$. See text for explanation. The attractor $\mathbb{H}_2$ is plotted in figure 51.

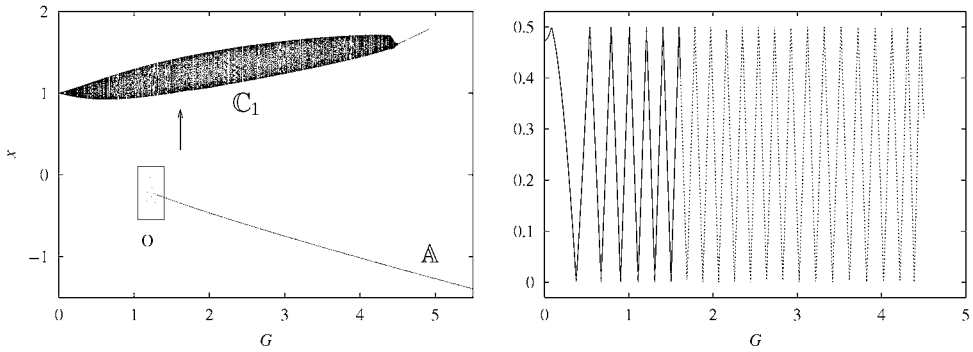

Figure 36. Left: projection on (G, x) of sequences of repellors and attractors for $F = 4$ and $\epsilon = 0.5$. The picture has been obtained as figure 35. Right: rotation number modulo $1/2$ on $\mathbb{C}_1$, along the family plotted in the left picture.

decrease. Although a quasi-periodic Hopf bifurcation might occur at $G > 1.615$ (where $\mathbb{C}_1$ changes stability), no invariant repelling torus could be detected. For all F-values in figure 36 (left), the rotation number (modulo $1/2$) of $\mathbb{C}_1$ is plotted on the right. It repeatedly takes on all values between zero and one, the number of complete oscillations tells how many times. This means that the Arnol'd tongues are crossed transversally, agreeing with the orientation as deduced from figure 25 (right).

4.6. Coexistence of attractors and saddles in $\mathfrak{U}'$

The projection in figure 36 (left) has been chosen to illustrate coexistence of the attractors $\mathbb{C}_1$ and $\mathbb{A}$ in the G-interval (1.17, 1.615). Close to $G = 1.17$ (box indicated by O), the coordinates of $\mathbb{A}$ are sensitive to changes in G. This is illustrated by a magnification of box O (figure 37(a)) obtained as follows. Parameter values are chosen on a short line vertically intersecting region $\mathfrak{U}'$. In particular, F is fixed at 4 and G varies on a grid with spacing 2×10^{-5}. The map $\mathcal{P}_{F,G}$ is iterated starting from the point $(x, y, z) = (-0.24\,661\,261\,2,\ 1.006\,751\,225,\ -0.762\,249\,262)$. If there is convergence to a periodic point within 100 iterations, the (G, y) coordinates of the final point are plotted. We see relatively large G-intervals with an attracting fixed point, where

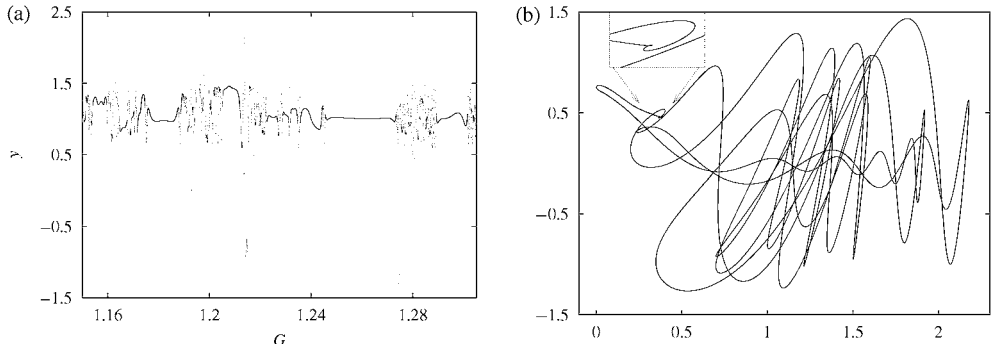

Figure 37. (*a*) Periodic points of $\mathcal{P}$ for $F = 4$ and G on a grid with spacing 2.e−5. For a few, sparse G-values, no periodic point is detected (see text). (*b*) Projection on (x, y) of a period T saddle limit cycle of $\Psi_{F,G,\epsilon}$, corresponding to a saddle fixed point of $\mathcal{P}$ coexisting with the SA in figure 38(*a*) at $G = 1.274\,585$.

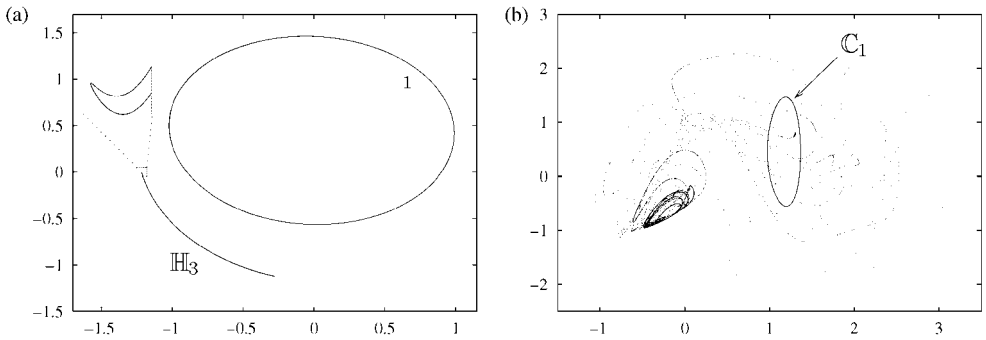

Figure 38. (*a*) Projection on (y, z) of the circle attractor $\mathbb{C}_1$ and of a Hénon-like attractor $\mathbb{H}_3$, coexisting at $(F, G) = (4, 1.274\,585)$. Initial conditions for $\mathbb{C}_1$ are $(x, y, z) = (1.14, -0.28, 1.4)$. (*b*) Projection on (x, z) of a chaotic transient of 69 000 $\mathcal{P}$-iterates at $(F, G) = (4, 1.302\,38)$, followed by convergence to the circle attractor $\mathbb{C}_1$. Initial point $(x, y, z) = (-0.367\,134\,395\,447\,287,\ 0.569\,918\,317\,744\,214,\ -0.883\,182\,668\,387\,643)$.

the evolution of its y-coordinate is rather regular. At the extremes of such intervals, regions occur where the y-coordinate evolves wildly. The limit cycles of $\Psi_{F,G,\epsilon}$ corresponding to these periodic points are of spiral type (section 4.4).

In fact, the distribution of the fixed point attractors figure 37(*a*) is similar to figure 34(*a*). All branches of attracting fixed points are connected by branches of saddle fixed points. The limit cycles of $\Psi_{F,G,\epsilon}$ corresponding to these saddles are also of spiral type (figure 37(*b*)). Several branches of saddle fixed points coexist in a G-interval, compare figure 34(*b*). For some parameter values, no periodic attractor occurs. In this case, the $\mathcal{P}$ iterates converge either to the circle $\mathbb{C}_1$, or to some narrow Hénon-like attractor coexisting with $\mathbb{C}_1$, like $\mathbb{H}_3$ in figure 38(*a*). This explains the sparse white spots in $\mathfrak{U}'$, compare figure 2(*b*) and figure 5 (right). Notice that the same type of Hénon-like attractor and the same structures of fixed point attractors/saddles occur in region $\mathfrak{U}$ (section 4.10). In fact, the only difference is that no Shil'nikov-like attractors seem to occur in $\mathfrak{U}'$. Sometimes, long chaotic transients are often observed (figure 38(*b*)), having the shape of Shil'nikov-like attractors. However they usually converge to the circle $\mathbb{C}_1$ or to a periodic or to a narrow Hénon-like attractor. So, the disappearance of the invariant circle $\mathbb{C}_1$ seems to be a necessary condition for the occurrence of Shil'nikov-like attractors.

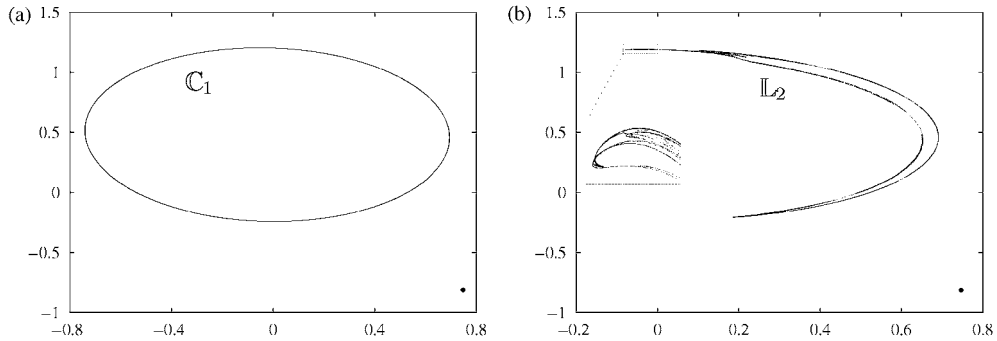

Figure 39. (*a*) Projection on (y, z) of the circle attractor $\mathbb{C}_1$, coexisting with the fixed point $\mathbb{A}$ at $(F, G) = (3, 1.4905)$. Initial conditions are $(x, y, z) = (1.3, 0.35, 1)$ for $\mathbb{C}_1$ and $(1, 2, 3)$ for $\mathbb{A}$. (*b*) Same as (*a*), with the SA $\mathbb{L}_2$ at $G = 1.494$.

Above region $\mathfrak{U}'$, the fixed point $\mathbb{A}$ may coexist with $\mathbb{C}_1$ or with a SA originating from the breakdown of $\mathbb{C}_1$. In both the above regions, the fixed point $\mathbb{A}$ may coexist with a SA as well. This is the case for the attractor $\mathbb{L}_2$ in figure 39(*b*), which is a folded circle (see section 4.8), created in the following way. The circle $\mathbb{C}_1$ is locked to a fixed point in the G-interval $1.462 \lessapprox G \lessapprox 1.508$. The fixed point undergoes a Hopf bifurcation as G decreases through $G \simeq 1.4975$. At this point, $\mathbb{C}_1$ is broken and a new attracting circle $\tilde{\mathbb{C}}$ appears. The latter circle enters an Arnol'd tongue of high period and breaks down inside it because of a homoclinic tangency and $\mathbb{L}_2$ is born.

This and other scenarios for the breakdown of a circle are described in the next section.

4.7. Mathematical intermezzo: breakdown of invariant circles and the creation of strange attractors

A large fraction of the strange attractors of $\mathcal{P}_{F,G}$ at $\epsilon = 0.5$ in regions $\mathfrak{L}_2$ and $\mathfrak{L}_1$ originates from the breakdown of an attracting invariant circle (see figures 6, 7, and 39(*b*)). We devote this section to a summary of the known phenomenology for the destruction of a circle. A detailed description can be found in, for example, [2, 16, 47].

Consider a two-parameter family of diffeomorphisms $\mathcal{D}_{F,G}$ of $\mathbb{R}^n$, having a curve $\mathcal{H}$ of Hopf bifurcations of fixed points. In figure 40 we sketch the 'generic' semi-global structure of the parameter space close to an Arnol'd tongue. Two curves $\mathcal{SN}$ of saddle-node bifurcations emerge from a resonant point $\mathcal{R}$ on $\mathcal{H}$ and form the boundary of an Arnol'd tongue $\mathfrak{A}^q$ of period q. Outside $\mathfrak{A}^q$, and for (F, G) close to $\mathcal{H}$, the map $\mathcal{D}_{F,G}$ has a quasi-periodic attracting circle. We will describe the routes occurring along the dashed paths starting at point $\mathbb{P}$, inside $\mathfrak{A}^q$. There, the circle $\mathbb{C}$ is locked to the periodic attractor $\mathbb{P}$. This means that $\mathbb{C}$ is formed by the union of the unstable manifolds of the saddle periodic point $\mathbb{S}$ born with $\mathbb{P}$ at the curve $\mathcal{SN}$ (for regularity properties of such resonant circle (see, e.g. [16]). Moving along path A, at curve $\mathcal{D}$ the attractor $\mathfrak{P}$ loses stability through a codimension one bifurcation. This might be a period doubling, but also a Hopf bifurcation (cf figure 39). No strange attractors are created at this moment. This only occurs when crossing the critical curve $\mathcal{CR}_1$, which, for example, might be the last of a cascade of period doublings of $\mathbb{P}$.

Along path B, at the curve $\mathcal{T}$ a tangency of the stable and unstable manifold of $\mathbb{S}$ occurs. The circle is destroyed, but no SA appears, since the point $\mathbb{P}$ is always stable between curves $\mathcal{SN}$ and $\mathcal{D}$. SAs appear on path B1, when coming out of the tongue. Here, intermittency

of type I is usually observed close to $\mathcal{SN}$ (this is what happens in figure 6). The 'curve' $\mathcal{CR}_2$ corresponds to the creation of a non-smooth circle from $\mathbb{C}$ and has a complicated fractal structure [1, 16]. Along path C1, there is a sudden transition between a periodic attractor and a non-smooth circle SA. Path C corresponds to the bifurcation from a locked to a quasi-periodic circle. Notice that all kinds of 'composite' routes can be observed. For example, there can be a finite number of period doublings, followed by a homoclinic tangency (path A1; see, e.g. [16, 67]).

Remark 4.5. Our description only covers the main details in the most simple case. For example, along path B, the circle is usually destroyed before the homoclinic tangency on curve $\mathcal{T}$. Indeed, the latter may occur after a cubic and a quadratic tangency of the unstable manifold of the saddle periodic point with the strong stable foliation. For more details, see [16, 47].

We now list some other routes to chaos. In the Díaz–Rocha–Viana scenario [26], the unstable manifold of a saddle-node periodic point has a quadratic tangency with the strong stable foliation. Here, parameter values lie at the border of an Arnol'd tongue. Just outside the tongue, Hénon-like SAs occur, winding around the whole annulus containing the unstable manifold of the saddle-node. Such attractors are called 'large'. Large attractors were also studied in [8], in connection with a Shil'nikov–Hopf bifurcation.

Finally, other dynamical objects could interact with the circle $\mathbb{C}$, for example through heteroclinic tangencies. This is the typical way in which the size of a strange attractor suddenly grows [56].

We have mainly distinguished four regions inside $\mathfrak{M}_{0.5}$ where SAs occur. In $\mathfrak{L}_1$ and $\mathfrak{L}_2$, the appearance of SA is typically due to homoclinic tangencies inside an Arnol'd tongue (routes A1 and B1 in figure 40) or period doubling (route A). Loss of smoothness (route C1) is more difficult to observe, given the ubiquitous occurrence of resonances of high order. In $\mathfrak{L}_2$, interaction with a quasi-periodic period doubling bifurcations leads to attractors of dimension higher than two. A different scenario leads to birth of SA in $\mathfrak{U}$ and $\mathfrak{U}'$, probably due to a Shil'nikov tangency bifurcation. For a classification of the SAs of $\mathcal{P}_{F,G}$, see section 4.11.

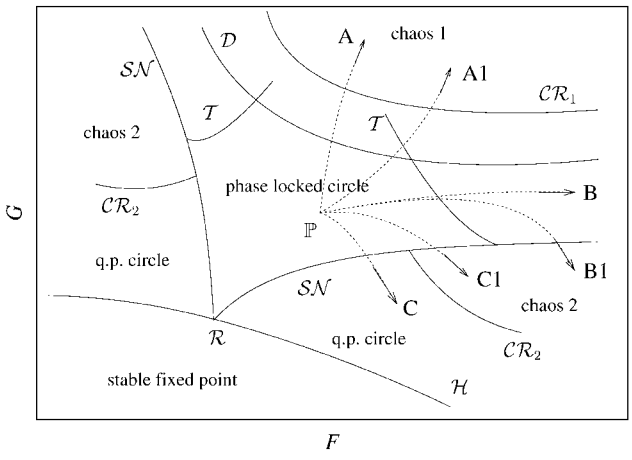

Figure 40. Dashed paths labelled by A, A1, B, B1, C1 indicate several routes to the breakdown of an invariant circle of $\mathcal{D}_{F,G}$, born from a fixed point at a curve $\mathcal{H}$ of Hopf bifurcations (see text for the notation). Figure taken from [1].

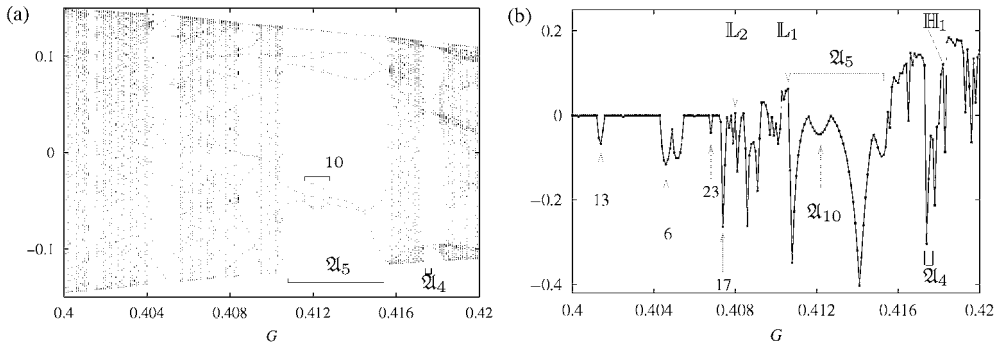

Figure 41. (*a*) Projection on the y-axis of sequences of $\mathcal{P}$-attractors as a function of G, for $F = 1.25$ fixed. The last 100 points of each iteration loop are plotted, the step in G is 10^{-4}. See text for explanation. (*b*) Maximal Lyapunov exponent on the attractors in (*a*).

4.8. The chaotic range $\mathfrak{L}_1$

We consider the region above the tongue $\mathfrak{A}_1$ of period one in figure 5. There the parameter plane is crossed by several, relatively large Arnol'd tongues of higher periods. The circle $\mathbb{C}_1$ often breaks and SAs appear similar to $\mathbb{L}_1$ (figure 6(*B*)), with Lyapunov dimension slightly larger than one. Two views of this chaotic range are given in figures 41 and 43. The intervals where the maximal Lyapunov exponent λ_1 drops to negative values are Arnol'd tongues. In figure 41(*b*), a period k attractor occurs on intervals pointed by an arrow with label k. For small G (left of the picture), $\mathbb{C}_1$ appears to persist, since λ_1 is approximately zero outside the tongues. A large Hénon-like attractor occurs at $G = 0.408$ (label $\mathbb{L}$ in figure 41(*b*)), a folded circle like $\mathbb{L}_1$ (figure 6(*B*)). Periodic points are detected for most parameter values near $G = 0.408$, with period ranging from 28 up to a few hundreds. For G larger, λ_1 increases and SAs are found more frequently. An arrow in figure 41(*b*) indicates the G-value at which $\mathbb{L}_1$ occurs, just outside an Arnol'd tongue $\mathfrak{A}_5$ of period five. A saddle-node bifurcation at the edge of $\mathfrak{A}_5$ destroys $\mathbb{L}_1$, locking it to a period-five attractor. Notice that a period doubling occurs at $G = 0.4116$, followed by a period halving at $G = 0.4128$. The two bifurcations, where $\lambda_1 = 0$, bound a period 10 tongue $\mathfrak{A}_{10}$ inside $\mathfrak{A}_5$ (figure 41(*a*)).

Inside the Arnol'd tongues, period doublings also may occur in entire cascades. The four-piece strange attractor $\mathbb{H}_1$ in figure 42(*a*) is created by this mechanism, which corresponds to route A in figure 40. At $G = 0.4175$ the map $\mathcal{P}$ has a period-four attractor inside the tongue $\mathfrak{A}_4$ (figures 41(*a*) and (*b*)). Then, at $G = 0.4177$ and $G = 0.4179$ period 8 respectively 16 points occur, followed by a whole period-doubling cascade, and $\mathbb{H}_1$ appears. Notice that each of its four components is obviously Hénon-like (component 1 is magnified in figure 42(*b*)). Component k is mapped by $\mathcal{P}$ to $k + 1$ for $k = 1, 2, 3$ and 4 is mapped to 1.

Another four-piece Hénon-like attractor occurs at $G = 0.4182$, but folded circles like $\mathbb{L}_1$ reappear for larger G, from the fusion of the various pieces. The fusion of the parts of a multi-piece attractor is usually due to heteroclinic tangencies, see [56].

So far, the Lyapunov dimension D_L of the attractors is still close to one. However, D_L can grow above two for parameter values further inside $\mathfrak{L}_1$. In figure 43(*a*) sequences of attractors are plotted for $G = 0.5$ fixed and F increasing from 1, where the fixed point $\mathbb{A}$ is detected. Notice that the maximal Lyapunov exponent λ_1 (figure 43(*b*)) increases linearly, until a Hopf bifurcation[23] $\mathcal{H}$ occurs at $F \simeq 1.08$ and the circle attractor $\mathbb{C}_1$ is created. Although $\mathbb{C}_1$ is not

[23] Belonging to the curve $\mathcal{H}_1$ in figure 5 (left), section 1.3.

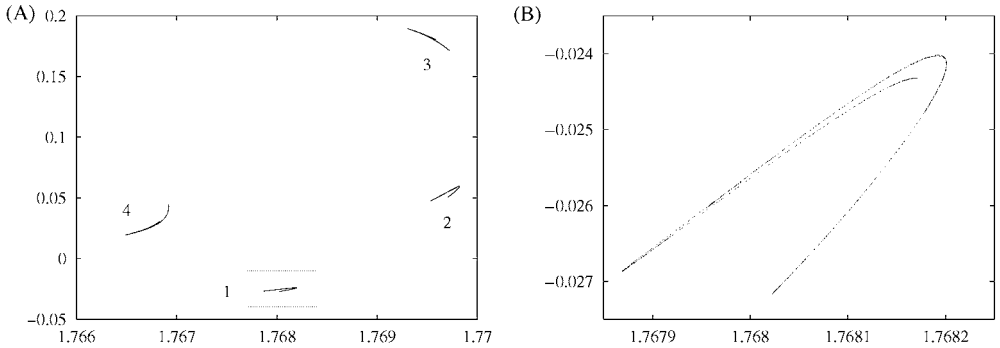

Figure 42. (*A*) Projection on (x, z) of Hénon-like SA $\mathbb{H}_1$ of $\mathcal{P}$ for $(F, G) = (1.25, 0.4181)$. (*B*) Magnification of one component.

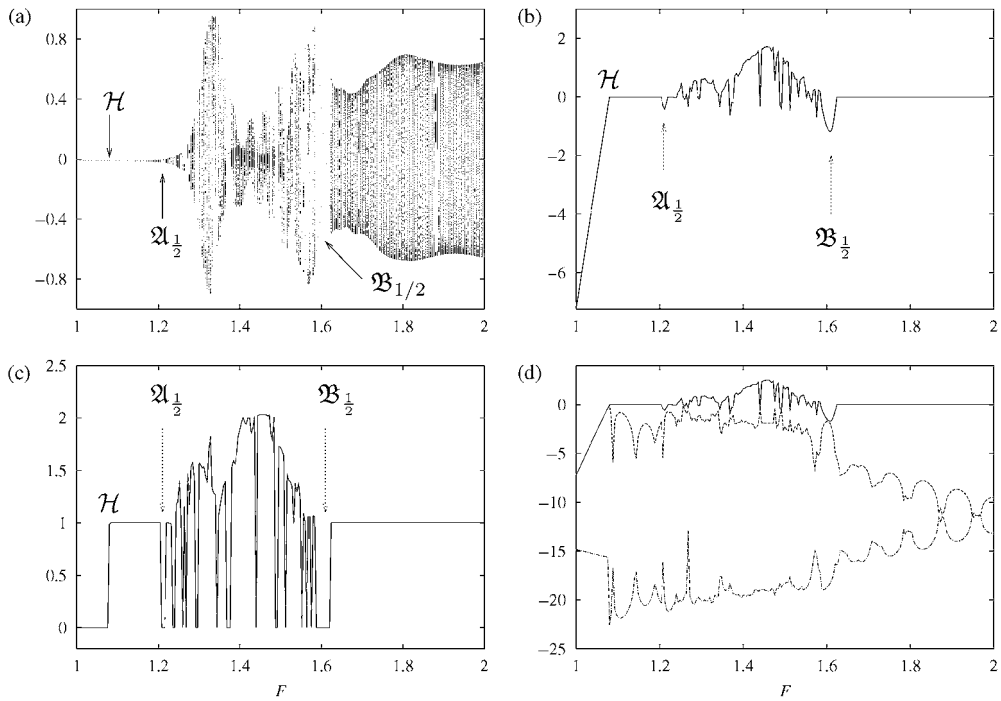

Figure 43. (*a*) Projection on the y-axis of sequences of $\mathcal{P}$-attractors as a function of F for $G = 0.5$ fixed. The step in F is 0.004 and 2×10^5 iterates of $D\mathcal{P}$ were computed for each F. Two Arnol'd tongues $\mathfrak{A}_{1/2}$ and $\mathfrak{B}_{1/2}$ of rotation number $1/2$ are pointed by an arrow. (*b*) Maximal Lyapunov exponent on the attractors in (*a*). (*c*) Lyapunov dimension of the attractors in (*a*). (*d*) The three Lyapunov exponents on the attractors in (*a*).

visible in figure 43(*a*) (because of its small size, compare remark 4.3), its presence is revealed by the Lyapunov dimension (figure 43(*c*)), which jumps to one at $\mathcal{H}$. An Arnol'd tongue of rotation number $1/2$ is labelled by $\mathfrak{A}_{1/2}$. Then $\mathbb{C}_1$ breaks and SAs occur in the interval $1.2 \lessdot F \lessdot 1.7$. Close to the extremes of the interval, the Lyapunov dimension is not much larger than one and the corresponding SAs are folded circles. In the central part, the structure of the attractors is more complicated, displaying interaction with other dynamical objects.

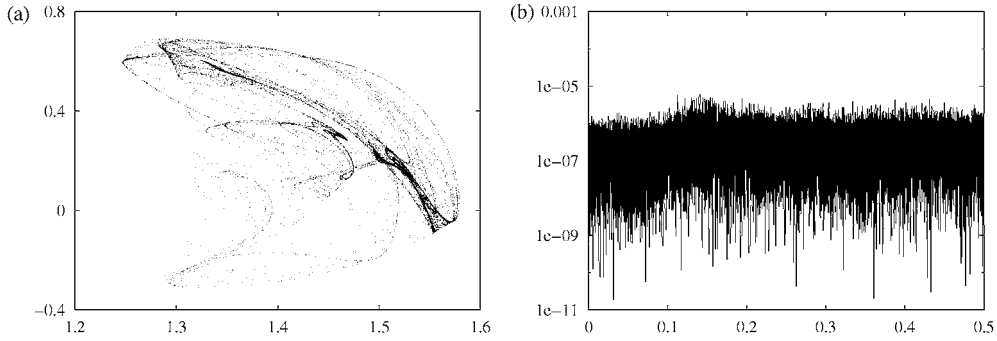

Figure 44. (*a*) Projection on (x, z) of a $\mathcal{P}$-attractor, which we name $\mathbb{X}_1$, occurring in $\mathfrak{L}_1$ at $(F, G) = (1.5, 0.5)$. (*b*) Power spectrum of $\mathbb{X}_1$.

Intermittency phenomena disappear from the power spectra and the Lyapunov dimension is larger. An attractor ($\mathbb{X}_1$) occurring in this parameter range is plotted in figure 44. Some one-dimensional structure is still preserved, in the form of several invariant folded curves crossing $\mathbb{X}_1$. However, the power spectrum indicates uncorrelation of the iterates (remark A.1) and the Lyapunov dimension is $\sim$1.6. At the other extreme of the chaotic interval, a tongue $\mathfrak{B}_{1/2}$ with rotation number $1/2$ occurs, and the circle $\mathbb{C}_1$ reappears for $F \gtrsim 1.7$.

It is well known [56] that the evolution of SAs is a process of birth and death (sometimes called 'crisis' [33]). This is clearly seen in figures 41 and 43. SAs are first created by homoclinic tangencies, then disappear because of the birth of a hyperbolic periodic attractor through a saddle-node bifurcation. They may reappear in multi-piece form due to doubling cascades, then the various pieces melt by heteroclinic tangencies and, eventually, the SA might grow in size due to further heteroclinic tangencies. A perhaps less known scenario is described in the next section.

4.9. The chaotic range $\mathfrak{L}_2$

This chaotic region lies in the half-plane $F \gtrsim 5$ inside $\mathfrak{M}_{0.5}$. Most strange attractors in $\mathfrak{L}_2$ originate at the breakdown of a doubled circle $2\mathbb{C}_1$, the latter created through one quasi-periodic period doubling of $\mathbb{C}_1$. For this reason, we begin by describing this bifurcation.

4.9.1. Quasi-periodic period doubling. The quasi-periodic period doubling of an invariant curve can occur in two different ways [20] and both have been found in the family $\mathcal{P}_{F,G}$. The first is illustrated in figure 45, for $F = 11$ fixed. At $G = 0.4972$ the circle attractor $\mathbb{C}_1$ is detected. Here $\mathbb{C}_1$ is still normally hyperbolic, with quasi-periodic dynamics, but it is close to loss of normal hyperbolicity. Indeed, the maximal Lyapunov exponent λ_1 is zero, while λ_2 is negative and close to zero (table 4). The peak at the fundamental frequency $f_1 = 0.377$ of $\mathbb{C}_1$ is labelled by 2 in figure 45(*a*). Peaks marked by $2k$ occur at harmonics $f_k = kf_1$ of the fundamental frequency[24]. When λ_2 goes through zero, $\mathbb{C}_1$ undergoes a quasi-periodic period-doubling. A circle attractor $2\mathbb{C}_1$ is created, of roughly double length and half the rotation number of $\mathbb{C}_1$ (figure 45(*B*)). In this bifurcation, only λ_2 crosses zero: the lowest Lyapunov exponent λ_3 of both $\mathbb{C}_1$ and $2\mathbb{C}_1$ is less than -14 (table 4). After the doubling, $\mathbb{C}_1$ still coexists with $2\mathbb{C}_1$, but it is unstable. The power spectrum of $2\mathbb{C}_1$ inherits all harmonics of a frequency

[24] In particular, f_k is obtained modulo 1 for $k = 6, 10, 12, 16, 18, 20, 22$, whereas for the remaining harmonics one gets $f_k \mathrm{mir}\,\frac{1}{2}$.

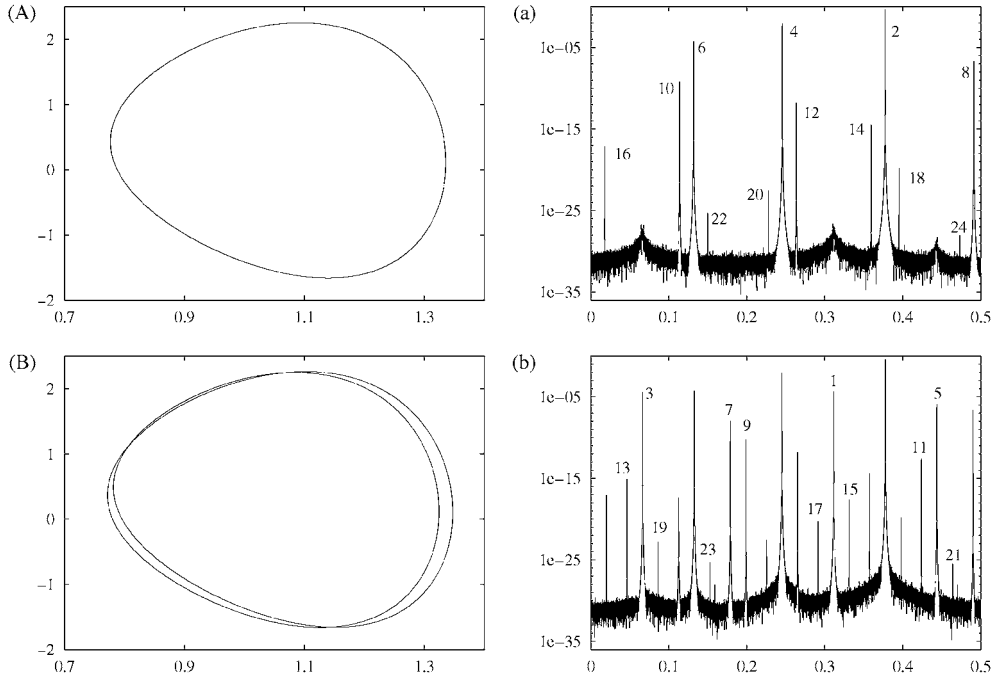

Figure 45. (*A*), (*B*) Projections on (x, z) of circle attractors of $\mathcal{P}_{11,G,0.5}$ for $G = 0.4872$ and $G = 0.4874$, respectively. (*a*), (*b*) Power spectra of the attractors.

Table 4. Lyapunov exponents of the circle attractors in figures 45(*A*) and (*B*).

	D_L	λ_1	λ_2	λ_3	e_1	e_2	e_3
A	1	$-5 \cdot e{-}6$	-0.0066	-14.8	$6 \cdot e{-}7$	$2 \cdot e{-}6$	$1 \cdot e{-}6$
B	1	$4 \cdot e{-}5$	-0.08	-14.7	$5 \cdot e{-}6$	$5 \cdot e{-}6$	$1 \cdot e{-}6$

close to f_1. Furthermore, new peaks appear at uneven multiples $g_k = kg_1$ of the fundamental frequency $g_1 \approx f_1/2$ of $2\mathbb{C}_1$ (each harmonic g_k is labelled by k in figure 45(*b*)). Again, because of the mirroring one has $g_1 = 1/2(f_1 \mathrm{mir}\frac{1}{2}) = 0.3115$. It is also possible to identify small peaks corresponding to g_1, g_2 and g_3 in figure 45(*a*). This is due to intermittency of type III.

For the family $\mathcal{P}_{F,G,0.5}$, the circle $\mathbb{C}_1$ often undergoes similar doublings in the interval $5 \lessapprox F < 12$. Each of these bifurcation points belongs to a frayed curve as described in section 3.2.2. For some F values, $2\mathbb{C}_1$ may undergo a doubling as well, but a different type of bifurcation occurs. This is illustrated in figure 46, again for $F = 11$ fixed. At $G = 0.4958$ the circle $2\mathbb{C}_1$ is detected (figure 46(*A*)). All peaks in the power spectrum occur on harmonics of the fundamental frequency $g_1 = 0.325\,79$. The first five harmonics $g_k = kg_1$ are labelled by k in figure 46(*a*). Between $G = 0.4958$ and 0.4959, $2\mathbb{C}_1$ turns into a saddle invariant curve and two curves are created, each of them attracting and invariant under $\mathcal{P}^2$. The union of these two curves is the $\mathcal{P}$-attractor $4\mathbb{C}_1$, plotted in figure 46(*B*) (also see figure 7 in section 1.3). The dynamics of $\mathcal{P}$ on $4\mathbb{C}_1$ is the skew product of an invariant curve and a period-two point. In other words, the $\mathcal{P}$-iterates jump from one curve to the other and back, so we call $4\mathbb{C}_1$ a period-two curve. Therefore, the dynamics has two fundamental frequencies, one of which is

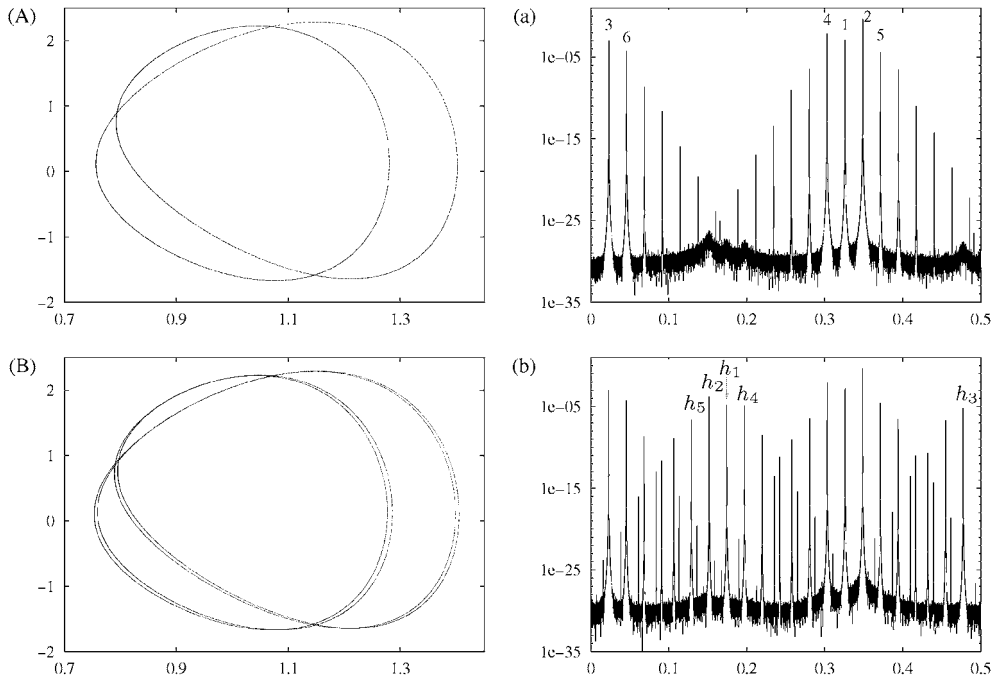

Figure 46. (*A*), (*B*) Projections on (x, z) of attractors of $\mathcal{P}_{11,G,0.5}$ for $G = 0.4958$ and $G = 0.4959$, respectively. (*a*), (*b*) Power spectra of the attractors.

0.5, the other is close to the frequency of $2\mathbb{C}_1$ and is again called g_1. In fact, all harmonics of g_1 are found in the power spectrum of $4\mathbb{C}_1$, while the 'new' harmonics h_k correspond to $0.5 - g_k$ (figure 46(*b*)).

For other values of $F < 12$, at most two consecutive doublings were observed, just as above, so no entire cascade (see next section).

We note that the centre manifold of the period doubling is a two-dimensional Möbius strip [19, 52]. As a result, the breakdown of a doubled circle is almost invariably followed by the creation of a SA with a two-dimensional Möbius-like structure. Examples of this are presented in section 4.9.3.

4.9.2. Arnol'd tongues and breakdown of circles in $\mathfrak{L}_2$. The structure of region $\mathfrak{L}_2$ is in fact rather similar to that of $\mathfrak{L}_1$. In both regions, fixed and periodic points are organized in intricate structures of Arnol'd tongues. This is illustrated in figure 47 (left) (compare with figure 5 (right)), where we plot a magnification of figure 2(*b*), obtained by taking a smaller window and a finer spacing of the grid. A few edges of tongues (saddle-node bifurcation curves) of low period are plotted in figure 47 (right). Several cusps are found on most saddle-node curves. A Hopf bifurcation curve $\mathcal{H}$ was detected, interrupted by three Bogdanov–Takens and three $1:2$ strong resonance points. At the Bogdanov–Takens points, a saddle-node curve $\mathcal{S}$ is tangent to $\mathcal{H}$, whereas a period doubling curve $\mathcal{D}$ is tangent to $\mathcal{H}$ at the $1:2$ points. Furthermore, $\mathcal{D}$ and $\mathcal{S}$ are tangent to each other at the codimension-two saddle-node-period-doubling point $\mathcal{SPD}$. The occurrence of the Arnol'd tongues is quite similar to that found in the fattened Arnol'd family [16]. One sees that the edges of the bifurcation curves accumulate on each other as G increases. This is probably due to the same mechanism as described in [16], which may possibly be a route for the creation of infinitely many sinks (the Newhouse phenomenon [45, 49]).

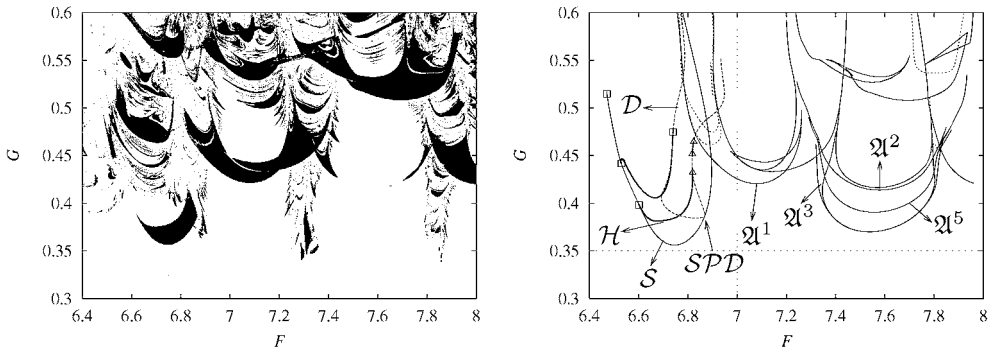

Figure 47. Left: Magnification of figure 2(*b*), obtained with a grid of spacing 2×10^{-3} in F and 5×10^{-4} in G. A maximum of 150 iterates of $\mathcal{P}$ were executed, starting from $(x, y, z) = (1, 2, 3)$. Right: Arnol'd tongues of period k are labelled by $\mathfrak{A}^k$ for $k = 1, 2, 3, 5$. The other solid curves are saddle-node bifurcations of fixed points. Dashed curves are period doublings of a fixed point. A Hopf curve $\mathcal{H}$ is plotted with a thick solid line. On $\mathcal{H}$, Bogdanov–Takens and 1 : 2 strong resonance points are marked by small boxes respectively triangles.

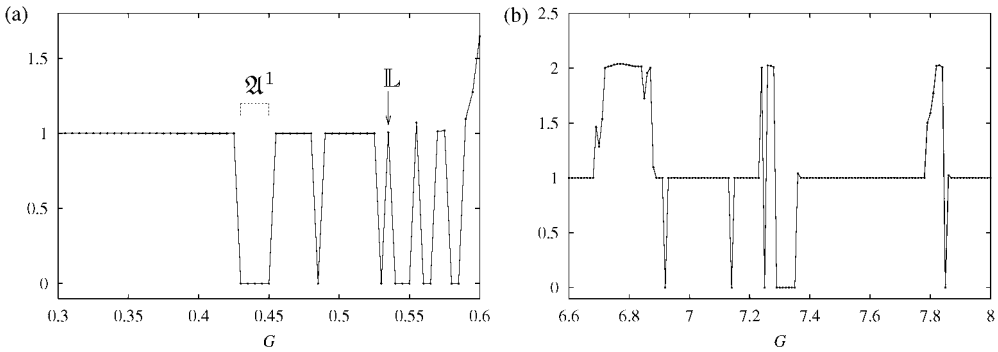

Figure 48. (*a*) Lyapunov dimension of the $\mathcal{P}$ attractors for parameter values on the vertical line $F = 7$ in figure 47 (right). (*b*) Same as (*a*), for the horizontal line $G = 0.35$. The step is 0.01 in both plots.

The resonant circle inside the tongues in figure 47 is $2\mathbb{C}_1$. In fact $\mathbb{C}_1$ has undergone a doubling at lower values of G and possibly persists as saddle circle. The breakdown of $2\mathbb{C}_1$ happens according to what discussed in section 4.7. Therefore, the 'curve' of breakdown of $2\mathbb{C}_1$ (which we sketched by curve $\mathcal{B}$ in figure 4) has a complicated fine structure (compare [16]). This is illustrated by a plot of the Lyapunov exponents λ_1 and λ_2 (figure 48) along the two dashed lines in figure 47 (right).

For $F = 7$ (figure 48(*a*)), the circle $2\mathbb{C}_1$ persists beyond the tongue $\mathfrak{A}^1$ in figure 47 (right). The first SA found increasing G is labelled by $\mathbb{L}$ and is a folded circle. However, for $G = 0.35$ (figure 48(*b*)) three intervals appear where the Lyapunov dimension is larger than one, while $2\mathbb{C}_1$ still exists outside them. This implies that curve $\mathcal{B}$ is in reality much more complicated than what is sketched in figure 4.

4.9.3. Quasi-periodic Hénon-like strange attractors. In region $\mathfrak{L}_2$, at most two consecutive quasi-periodic period doublings occur as G increases, depending on the value of F. A whole cascade has not been observed, because the attractors $2\mathbb{C}_1$ or $4\mathbb{C}_1$ are eventually destroyed by a homoclinic tangency inside an Arnol'd tongue (as in section 4.7).

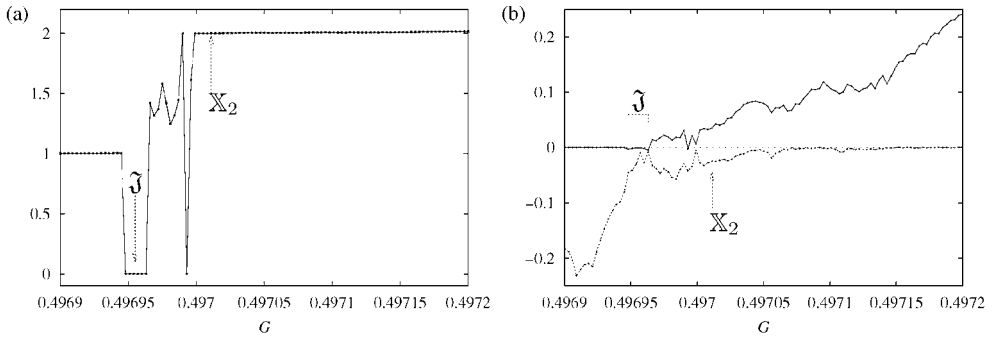

Figure 49. (*a*) Lyapunov dimension of $\mathcal{P}$-attractors as a function of G for $F = 11$ fixed. The step in G is 3×10^{-6}. For these estimates 2×10^5 iterates of $D\mathcal{P}$ were computed. An arrow points at the G value where the attractor $\mathfrak{X}_2$ occurs (figure 50(*d*)). (*b*) Lyapunov exponents λ_1 and λ_2 on the attractors in (*a*).

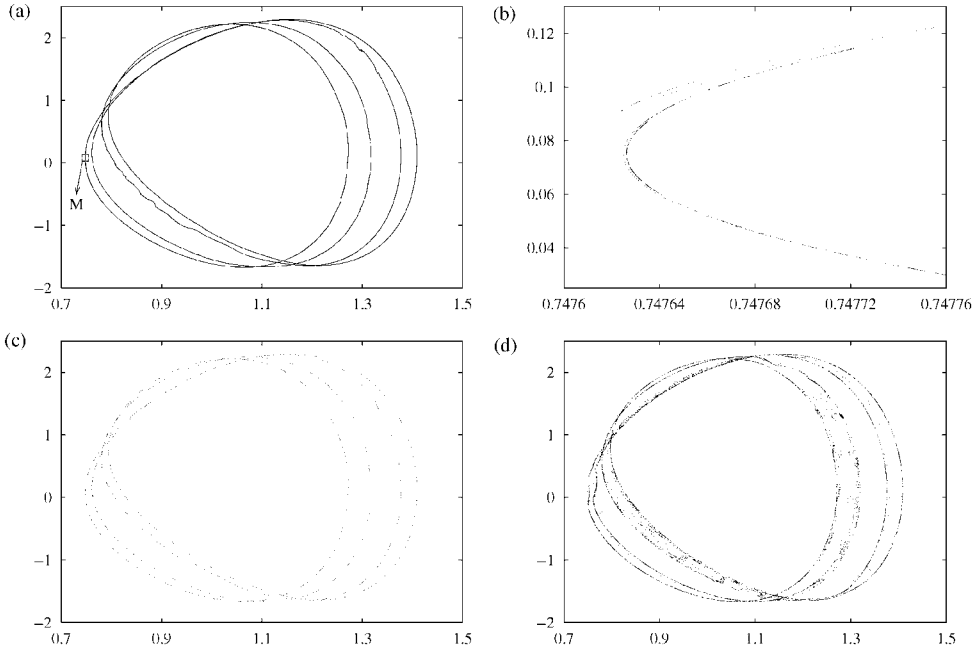

Figure 50. (*a*) Projection on (x, z) of the SA $\mathbb{L}_3$ of $\mathcal{P}$ at $(F, G) = (11, 0.496\,953\,2)$. (*b*) Magnification of box M in (a). (*c*) Same as (*a*) for the period 1098 point of $\mathcal{P}$ at $G = 0.496951$. (*d*) Same as (*a*) for the strange $\mathcal{P}$-attractor $\mathbb{X}_2$ at $G = 0.497011$.

We illustrate this route for the period-two circle attractor $4\mathbb{C}_1$ (figure 7(*A*)) by means of a plot of the Lyapunov dimension figure 49(*a*). For G close to 0.4969, the period-two circle $4\mathbb{C}_1$ persists and it is quasi-periodic since $D_L \simeq 1$. At this moment, the saddle invariant circle $2\mathbb{C}_1$ still coexists with $4\mathbb{C}_1$. Moreover, $2\mathbb{C}_1$ has a two-dimensional Möbius strip unstable manifold, whose edge is $4\mathbb{C}_1$. Then $4\mathbb{C}_1$ enters some Arnol'd tongue, where λ_1 becomes negative. In the G-interval $\mathfrak{J} = \{G \,|\, 0.496\,948 < G < 0.496\,963\}$ only periodic points are detected ($D_L = 0$ in figure 49(*b*)). In reality, SA occur in $\mathfrak{J}$ as well[25]. One of these is the 'large' SA $\mathbb{L}_3$ occurring at $G = 0.496\,953\,2$, figure 50(*a*). In figure 50(*b*) a small piece of $\mathbb{L}_3$ is enlarged, illustrating

[25] They are not revealed in figure 49 because of the step size in G.

the folded circle structure. The maximal Lyapunov exponent on $\mathbb{L}_3$ is $\lambda_1 \simeq 0.0025$. However, attracting periodic points of high period are prevalent in the neighbourhood, like the period 1098 point in figure 50(*c*).

For G larger the $\mathcal{P}$-iterates begin to wander in the transversal unstable manifold of the saddle circle $2\mathbb{C}_1$. This is reflected in the Lyapunov dimension, which grows up to two. For the attractor $\mathbb{X}_2$ in figure 50(*d*) the Lyapunov dimension is almost two, but λ_2 is still negative. This identifies it as an intermediate stage between a broken-circle and a quasi-periodic Hénon-like attractor. For G larger λ_2 approaches zero and the $\mathcal{P}$-iterates spread even more in the transversal manifold. Notice that $\lambda_2 \simeq 0$ near $G = 0.4972$, where the attractor $\mathbb{Q}_1$ occurs (figure 7(*B*)). This means that quasi-periodic Hénon-like attractors seem to have a certain degree of persistence under perturbations.

However, for (F, G) farther inside $\mathfrak{L}_2$ more complicated types of attractors are found, with no intermittency in the power spectra. An example is the attractor in figure 53(*a*).

4.10. The chaotic range $\mathfrak{U}$

We now turn to the attractors in the chaotic region $\mathfrak{U}$. No invariant circles occur here, and periodic point attractors are prevalent. SAs appear suddenly where the periodic points lose stability. To describe this, consider figure 12. At $G = 2$, the fixed point $\mathbb{A}$ is detected. Parameter values lie inside the narrow black strip below region $\mathfrak{Q}_2$ (figure 2(*b*)) where $\mathbb{A}$ is the unique attractor. As G is decreased, $\mathbb{A}$ is suddenly replaced by the Shil'nikov-like SA $\mathbb{S}_1$ (figure 9, left). The dynamics on $\mathbb{S}_1$ is quite sensitive with respect to initial conditions, due to the size of the maximal Lyapunov exponent (table 5). Indeed, the fact that the power spectrum of $\mathbb{S}_1$ (figure 9(*b*)) looks like white noise confirms that the iterates of $\mathcal{P}$ are almost uncorrelated. However, $\mathbb{S}_1$ has a rather one-dimensional character, since $\mathrm{D_L}(\mathbb{S}_1) \simeq 1.05$. Most Shil'nikov-like SAs inside $\mathfrak{U}$ have richer structure than $\mathbb{S}_1$ (cf figure 10(*a*)). This corresponds to a larger maximal Lyapunov exponent and larger Lyapunov dimension.

Among Shil'nikov-like, also Hénon-like attractors may occur, of course. The SA $\mathbb{H}_2$ in figure 51(*A*) is found at $(F, G) = (5, 1.29)$. A projection of $\mathbb{H}_2$ also can be seen as a small segment in figure 35. A magnification of a portion of $\mathbb{H}_2$ suggests that $\mathbb{H}_2$ is a quite narrow Hénon-like attractor. Similar attractors also exist in $\mathfrak{U}'$ (figure 38(*a*)). Shil'nikov-like attractors like $\mathbb{S}_3$ (figure 51(*B*)) occur for nearby parameter values. The transition from $\mathbb{H}_2$ to $\mathbb{S}_3$ corresponds to a jump in the largest Lyapunov exponent, although both attractors have dimension just slightly larger than one (see table 6). Notice that a portion of $\mathbb{S}_3$ (singled out by box N) approximately agrees with $\mathbb{H}_2$, while the small spiral part (magnified in figure 51(*B1*)) looks like the Shil'nikov attractors found in [8]. A magnification of a tiny piece of the spiral is plotted in figure 51(*B2*). Some parts of $\mathbb{S}_3$ are visited by a small fraction of the total number of iterates. This is not a transient effect: $\mathbb{S}_3$ has low density at such parts. For instance, the domain $(y, z) \in [0.69, 1.48] \times [-0.91, 1.39]$ contains 97.9% of the points in $\mathbb{S}_3$. Among them 99.8% are on $x \in [-0.35, 0.61]$.

The ranges of existence of Shil'nikov–like SAs are interspersed by relatively large windows of fixed points, where the corresponding T-periodic limit cycles of system (2) are of spiral type (compare figure 12). However, SAs become prevalent close to the value (F_0, G_0)

Table 5. Lyapunov exponents of the SAs $\mathbb{S}_1$ (a) and $\mathbb{S}_2$ (b) in figures 9 and 10.

	$\mathrm{D_L}$	λ_1	λ_2	λ_3	e_1	e_2	e_3
a	1.05	1.72	−33.6	−128.4	4 · e−4	6 · e−4	7 · e−4
b	1.27	4.8	−18.1	−100.5	1 · e−3	6 · e−4	2 · e−3

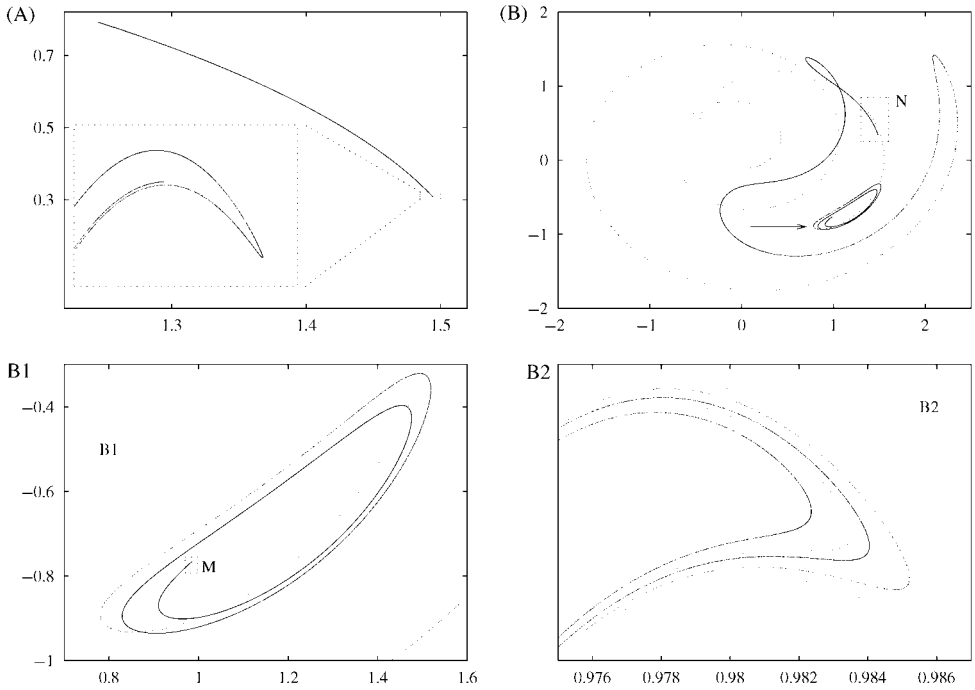

Figure 51. (*A*) Projection on (y, z) of the Hénon-like attractor $\mathbb{H}_2$ for $(F, G) = (5, 1.29)$. A small piece of $\mathbb{H}_2$ is magnified in the box. There, the graph has been affinely deformed by plotting $(y, \tilde{z})$, with $\tilde{z} = z + 3.81 \times (y - 1.49)$. (*B*) Same as (*A*) for the Shil'nikov-like attractor $\mathbb{S}_3$ at $G = 1.290\,05$. The portion of $\mathbb{S}_3$ inside box N approximately coincides with $\mathbb{H}_2$. (*B1*) Magnification of the spiral part of $\mathbb{S}_3$. (*B2*) Magnification of box M around the tip of the spiral part in (*B1*). The graph has been affinely deformed by plotting $(y, \tilde{z})$, with $\tilde{z} = z - 0.965 \times (y - 0.975)$. The width of the vertical window in (*B2*) is 1.4×10^{-4}.

Table 6. Lyapunov exponents of the SAs $\mathbb{H}_2$ (A) and $\mathbb{S}_3$ (B) in figure 51.

	D_L	λ_1	λ_2	λ_3	e_1	e_2	e_3
A	1.046	0.58	−12.6	−77.9	1 · e−5	4 · e−4	4 · e−4
B	1.097	1.13	−11.7	−87.1	1 · e−3	2 · e−4	1 · e−3

where a Shil'nikov-like attractor occurs. To be more precise, given an open ball $\mathfrak{B}_\delta \in \mathfrak{M}_{0.5}$ of radius δ, centred at (F_0, G_0), denote by $\mathfrak{S}_\delta$ the set of parameter values in $\in \mathfrak{B}_\delta$ for which a SA occurs. Some numerical results seem to suggest that

$$\frac{\text{meas}\,\mathfrak{S}_\delta}{\text{meas}\,\mathfrak{B}_\delta} \to C \quad \text{as } \delta \to 0, \qquad \text{with } C > 0, \tag{14}$$

where meas denotes the Lebesgue measure in $\mathfrak{M}_{0.5}$. This is illustrated in figure 52, where we plotted the Lyapunov dimension of $\mathcal{P}$-attractors against parameter values. On a larger scale (figure 52, left), periodic points are prevalent, since they occur in open parameter sets of large relative measure. On the other hand, in a small neighbourhood of $G = 1.211\,24$ (where a SA occurs), SAs are prevalent (figure 52, right).

Abundance of SAs, expressed by (14), is typical for parameters near a homoclinic tangency (see [26, 44, 48]). The results in figure 52 (right) give further evidence that Shil'nikov-like attractors are created by Shil'nikov tangency bifurcations of a saddle-focus fixed point, see section 5.

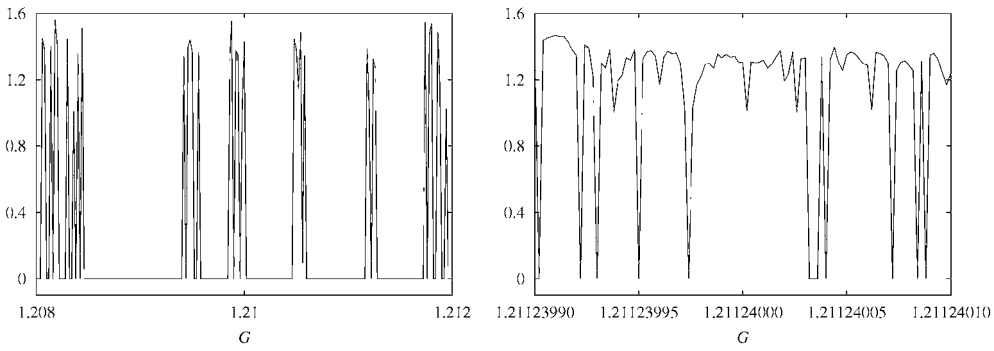

Figure 52. Left: Lyapunov dimension of $\mathcal{P}$-attractors as a function of G for $F = 8$ fixed. The step in G is 0.01. Right: same as left part with G-step 2×10^{-9}, displaying the magnification of a small interval around $G = 1.21124$.

4.11. Summary on the strange attractors of $\mathcal{P}$

We now sketch a classification of the SAs found in the family $\mathcal{P}_{F,G,\epsilon}$.

Hénon-like attractors of two types are found in both $\mathfrak{L}_1$ and $\mathfrak{L}_2$: folded circles and 'small' attractors. Both types of attractors have a local Hénon-like structure and occur close (in the parameter space) to an invariant circle, at the boundary of $\mathfrak{L}_1$ and $\mathfrak{L}_2$. Folded circles, like $\mathbb{L}_1$ (figure 6), $\mathbb{L}_2$ (figure 38(*b*)) and $\mathbb{L}_3$ in figure 50(*a*), are also called 'large' [8, 16], since they wind inside a whole annulus containing the unstable manifold of some saddle periodic point (see section 4.7). This does not hold for 'small' Hénon-like attractors, like $\mathbb{H}_1$ in figure 42. Deeper inside $\mathfrak{L}_1$ and $\mathfrak{L}_2$, strange attractors of other types are detected, like $\mathbb{X}_1$ (figure 44), $\mathbb{X}_2$ (figure 50(*d*)) or figure 53(*a*).

Some narrow Hénon-like attractors occur in both $\mathfrak{U}'$ (figure 38(*a*)) and $\mathfrak{U}$ (figure 51(*A*)). Furthermore, in $\mathfrak{U}$ also Shil'nikov-like attractors exist, like in figures 9, 10, and 51(*B*).

5. Discussion and outlook

In this paper, we present an inventory of the dynamics in the driven Lorenz-84 system, giving, whenever possible, an explanation of the changes occurring as the (F, G) vary in the plane $\mathfrak{M}_\epsilon$, for $\epsilon = 0.5$, and as ϵ is increased from zero. Several phenomena are discussed at the level of guesses or possibilities. It was not possible, indeed, to focus on all open problems in the course of this large-scale investigation.

In the next section we first summarize our findings for $\epsilon = 0.5$ with a rough subdivision of $\mathfrak{M}_{0.5}$, sketched in figure 4(*b*). Our exploration of the parameter raises several questions of both theoretical and applied nature. These are discussed in section 5.2.

5.1. Summary of achievements

The parameter plane $\mathfrak{M}_\epsilon$ at $\epsilon = 0.5$ can be divided into several regions, each with different dynamical phenomena. Three regions inside $\mathfrak{M}_{0.5}$, denoted by $\mathfrak{Q}_1$, $\mathfrak{Q}_2$, and $\mathfrak{F}$, have a rather simple dynamics (see next section). Four regions are characterized by occurrence of strange attractors (section 5.1.2). Then we describe results obtained for other values of ϵ.

5.1.1. Regular dynamics. A fixed point attractor $\mathbb{A}$ exists in the connected component $\mathfrak{F}$ of figure 4(*b*) containing the upper left corner. This corresponds to small F (see figures 1(*a*)

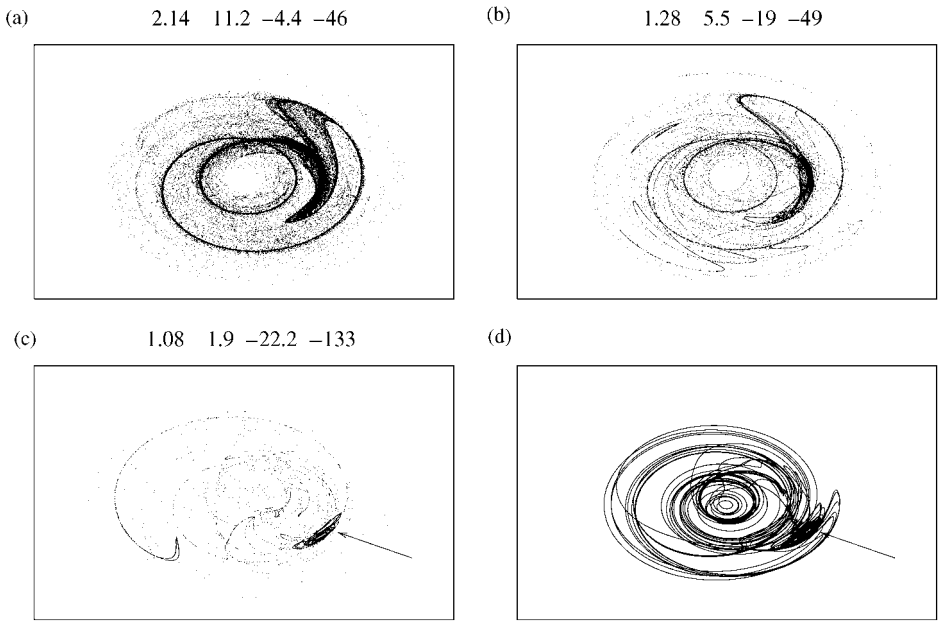

Figure 53. (*a*)–(*c*): Projection on (y, z) of SAs of $\mathcal{P}$ for $\epsilon = 0.5$ and $F = 7$. (*d*) Same projection of an attracting period $5T$ limit cycle of system (2). G is fixed at: (*a*) 1, (*b*) 1.08, (*c*) 1.4, (*d*) 1.400 000 037. The (y, z) window is $[-4, 4] \times [-3, 4]$ for all pictures. A spiral structure is pointed to by an arrow in (*c*) and (*d*).

and (*b*)), large G (compare the fixed points at the right of all pictures in figure 1) and to a thin strip between region $\mathfrak{Q}_2$ and $\mathfrak{U}, \mathfrak{U}'$.

A circle attractor $\mathbb{C}_2$ occurs in region $\mathfrak{Q}_2$. Sections of $\mathfrak{Q}_2$ by a vertical line $F = F_0$ give one-parameter families $\mathbb{C}_2 = \mathbb{C}_2(F_0, G)$ of circles. The cigar-shaped sequences of attractors in figures 1(*e*) and (*f*) are projections of such families. Region $\mathfrak{Q}_2$ is bounded by the Hopf curve $\mathcal{H}_2$; see section 4.1. Arnol'd tongues inside $\mathfrak{Q}_2$ are very thin and the prevalent behaviour seems to be quasi-periodicity. Although the dynamics in $\mathfrak{Q}_2$ is rather simple, the role played by the several strong resonance points on $\mathcal{H}_2$ should be studied in more detail.

Circle dynamics characterizes region $\mathfrak{Q}_1$ as well. The circle attractor $\mathbb{C}_1$ occurs at $G = 0$ for $F > 1$ and persists at least up to $G = 0.28$ (dotted horizontal line in figure 4 (left)). In fact, for some values of F this circle persists up to a larger value of G (see sections 4.5 and 4.9.2). Curve $\mathcal{B}$ in figure 4(*b*) roughly indicates the G-value up to which $\mathbb{C}_1$ seems to persist. Some thick dots indicate the occurrence of a quasi-periodic period doubling, where $\mathbb{C}_1$ loses stability and a doubled circle attractor $2\mathbb{C}_1$ appears (see section 4.9.1). It would be interesting to study this bifurcation, to detect the role played by strong resonances and 'bubbles' (cf section 3.2.2).

5.1.2. Chaotic dynamics. We turn to the description of the domains in $\mathfrak{M}_{0.5}$ where strange attractors occur. We have distinguished four regions $\mathfrak{L}_1$, $\mathfrak{L}_2$, $\mathfrak{U}'$ and $\mathfrak{U}$ (figure 4(*b*)). In all of them, SAs occur in regions of seemingly positive measure, interrupted by open windows of periodicity (Arnol'd tongues). In $\mathfrak{L}_2$ there is prevalence of SAs, while the typical behaviour in $\mathfrak{U}$ is periodicity (compare figure 12).

The creation of SAs in $\mathfrak{L}_2$ and $\mathfrak{L}_1$ is mostly due to homoclinic tangencies of a saddle periodic point inside an Arnol'd tongue (compare figure 50). Cascades of period doublings of periodic attractors are also observed (see figure 41). At the border of $\mathfrak{L}_2$ or $\mathfrak{L}_1$, the dynamics on

the attractors tends to follow the unstable manifold of a saddle periodic point, which for close parameter values still forms an invariant circle (figures 6 and 50). Therefore, most attractors have dimension close to one (figure 41). Intermittency is often observed in the power spectra. Marked peaks persist, close to the corresponding harmonics before the breakdown of the circle, and broad band has low power. As the parameters are shifted further inside $\mathfrak{L}_2$ or $\mathfrak{L}_1$, the dimension of the SAs grows above two (figures 43 and 49) and broad band arises in the power spectra (figure 44). In $\mathfrak{L}_2$, quasi-periodic Hénon-like SAs may appear (section 4.9.3). The mechanism for the birth of SA could not be so well clarified for region $\mathfrak{U}$. Most strange attractors have dimension between 1.1 and 1.4, the first case usually corresponding to narrow Hénon-like attractors. Shil'nikov like attractors (figures 9 and 10) of different type are found (see section 4.10). The transition between $\mathfrak{L}_2$ and $\mathfrak{U}$ is quite sudden (figure 12). It seems reasonable that this transition (on 'curve' $\mathcal{SH}$, figure 4(*b*)) and the birth of Shil'nikov–like SAs are due to three-dimensional homoclinic tangencies of a saddle-focus fixed point (Shil'nikov tangency bifurcation). Indeed, a spiral structure like in figure 51(*B1*) appears in the SAs when passing from $\mathfrak{L}_2$ to $\mathfrak{U}$, across 'curve' $\mathcal{SH}$. In particular, an increasing fraction of the points is contained in the spiral part (figure 53). Furthermore, the Lyapunov dimension and the maximal Lyapunov exponents decrease.

A high number of saddle spiral limit cycles coexists with the Shil'nikov SAs, and attracting spiral limit cycles occur for nearby parameter values. The spiral portion of the SAs roughly corresponds to that of the above limit cycles; see figures 53(*c*) and (*d*). Compare also figures 9(*A*) and 10(*A*) to figures 11(*A*) and (*B*), respectively. Attractors similar to the spiral portion were found in [8] (see figure 9), their occurrence being caused by a Shil'nikov tangency.

It is known that close (in the $\mathcal{C}^1$ topology) to a three-dimensional diffeomorphism having a Shil'nikov homoclinic tangency, diffeomorphisms with strange attractors [64] or displaying the Newhouse phenomenon occur [31, 49]. However, more detailed numerical and analytical studies are needed both to establish a relation with the occurrence of attractors like in figures 9 and 10(*A*), to determine the effect on the bifurcation set of a map and to establish the relative abundance of such attractors.

5.1.3. Overview of the plane $\mathfrak{M}_\epsilon$ for other values of ϵ. To quickly get information on the changes occurring for different values of ϵ, we performed other large-scale explorations of $\mathfrak{M}_\epsilon$ like in figure 2. The results, displayed in figure 54, suggest the following remarks. As ϵ increases:

1. Arnol'd tongues inside region $\mathfrak{Q}_2$ become wider, especially close to the strong resonance gaps on the lower branch of $\mathcal{H}_2$. As ϵ grows these gaps become larger as well and, eventually, 'eat up' the whole lower branch of $\mathcal{H}_2$ (compare also section 4.1). At $\epsilon = 0.9$, $\mathfrak{Q}_2$ is also shifted to larger F, which suggests that it may completely disappear for $\epsilon \geqslant 1$. This is supported by the following data: up to $\epsilon = 0.7$ the $\mathfrak{Q}_2$ region can be seen to appear around $F = 6$. For $\epsilon = 0.9$, 0.93, 0.95, 0.97, 0.98, and 0.99 the first invariant curves have been detected around $F = 14$, 20, 30, 58, 95, and 250, respectively.
2. Region $\mathfrak{Q}_1$ shrinks. As ϵ grows, the circle $\mathbb{C}_1(F_0, G)$ is destroyed at smaller values of G. Consequently, the chaotic range $\mathfrak{L}_2$ increases in size.
3. The fraction of periodicity increases inside $\mathfrak{L}_2$. In particular, the structures of Arnol'd tongues, which occupy a minor fraction of $\mathfrak{L}_2$ for small ϵ (figure 54(*a*)), invade most of $\mathfrak{L}_2$ at $\epsilon = 0.9$.
4. The chaotic range $\mathfrak{U}$, almost invisible for $\epsilon = 0.1$ grows in size.

Several dynamical phenomena of the autonomous system persist only for ϵ small enough. For example, the repelling invariant torus $\mathbb{T}$ occurring at $\epsilon = 0.01$ (section 3.2.2) seems to have completely disappeared for $\epsilon = 0.5$ (see section 4.5). One of the various ways in

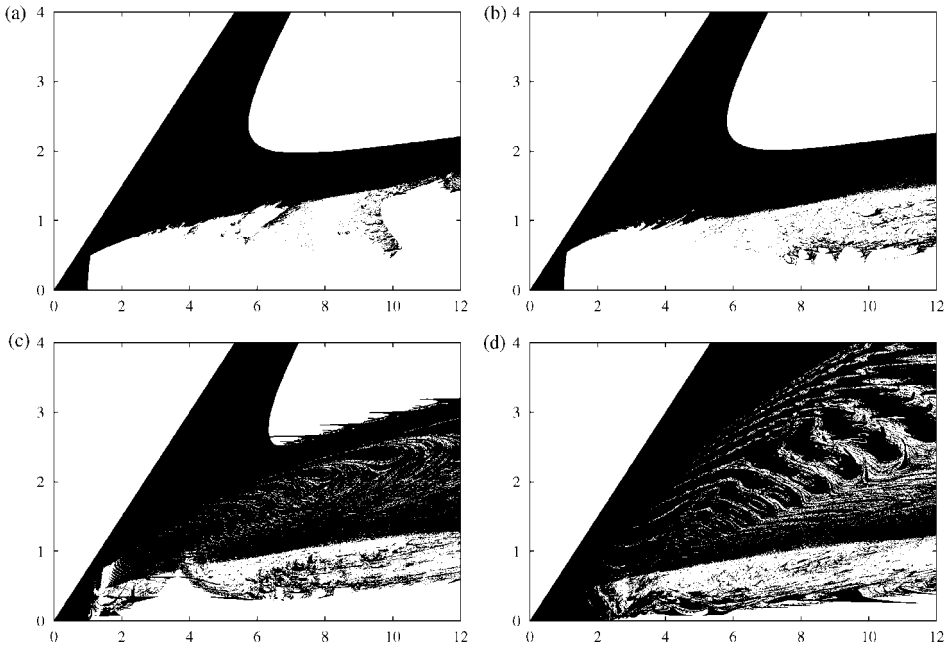

Figure 54. Same as figure 2(*b*). Parameter planes $\mathfrak{M}_\epsilon$ were scanned looking for periodic points, for the following values of ϵ: (*a*) 0.1, (*b*) 0.3, (*c*) 0.7, (*d*) 0.9.

which $\mathbb{T}$ is destroyed is illustrated in figure 55. The torus repellor $\mathbb{T}$ at $\epsilon = 0.01$ is plotted in figure 55(*A*). Since the two largest Lyapunov exponents λ_1 and λ_2 are approximately zero (table 7), it seems reasonable that the two fundamental frequencies f_1 and g_1 of $\mathbb{T}$ satisfy a Diophantine condition[26]. At $\epsilon = 0.066$, $\mathbb{T}$ is locked to a period 16 invariant curve. One of the frequencies of $\mathbb{T}$ is of course $f_1 = 16^{-1}$, since each of the 16 circles in figure 55(*B*) is invariant under $\mathcal{P}^{16}$, quasi-periodic and normally hyperbolic. This is confirmed by the fact that λ_1 is zero and λ_2 slightly negative. The other fundamental frequency $g_1 = 0.0116$ is equal to $j/16$, where j is the frequency under $\mathcal{P}^{16}$ of any of the 16. In figure 55(*b*) we indicated f_1 and g_1, together with their combinations $h_k = g_1 + kf_1$ with $k = 1,\ 2,\ 3$.

The same situation seems to persist for an interval of values of ϵ, but beyond $\epsilon = 0.0665$ the exponent λ_1 becomes slightly positive. In this case, the circles in figure 55(*B*) have lost smoothness. A strange repellor $\mathbb{U}$ is created, see figure 55(*C*), with $\mathrm{D_L}(\mathbb{U}) \simeq 2.083$. Several properties of $\mathbb{U}$ and of the SA $\mathbb{Q}_1$ (figure 7) are analogous. The fact that $\lambda_2 \simeq 0$ indicates that a quasi-periodic component persists in the dynamics on $\mathbb{U}$. The power spectrum of $\mathbb{U}$ has some broad band, but several harmonics of the resonant torus still persist. In figure 55(*c*), $f_2 = 0.25$, $f_3 = 0.5$ and g_1 are identified, but the h_k's persist as well. This is also due to intermittency, although of an unconventional type. It seems here that the dynamics is still driven by the ghost of the quasi-periodic circles in figure 55(*B*). Notice that $\mathbb{U}$ is made up of eight strips, each invariant under $\mathcal{P}^8$. The destruction of the 16 circles corresponds to the degeneration of frequency f_1 into broad band.

For ϵ even larger (figure 55(*D*)), the strips of figure 55(*D*) have melted into a global one-piece repellor. Although the Lyapunov dimension and λ_1 have increased further, the second Lyapunov exponent is still zero, and a peak around h_3 can still be distinguished. However, all harmonics of f_1 have merged into broad band in the power spectrum. A similar merging occurs

[26] This could be numerically checked up to some order of resonance by using refined Fourier analysis, see [30].

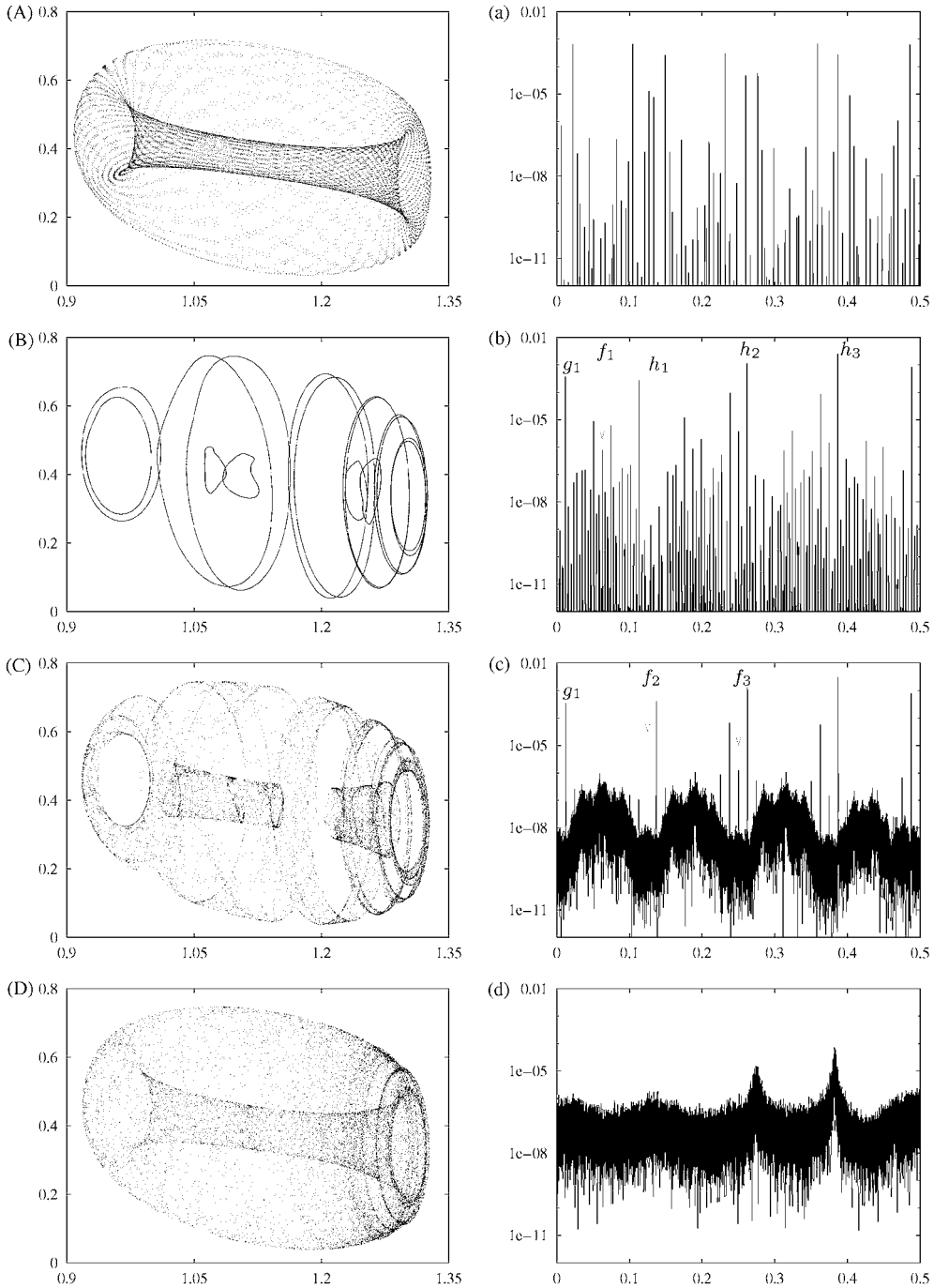

Figure 55. (*A*)–(*D*) Projections on the plane (x, z) of repellors of $\mathcal{P}_{F,G,\epsilon}$ for $(F, G, \epsilon) = (1.8, 1.65, 0.01)$, respectively, $\epsilon = 0.066$, $\epsilon = 0.0665$, $\epsilon = 0.0685$. (*a*)–(*d*) Power spectra of the repellors in (*A*)–(*D*). The same initial point as for figure 17 has been used.

Table 7. Lyapunov exponents (in the reversed time) and dimension of the repellors in figure 55.

	D_L	λ_1	λ_2	λ_3	e_1	e_2	e_3
A	2	$4.5 \cdot e{-5}$	$2 \cdot e{-5}$	-0.47	$6 \cdot e{-6}$	$3 \cdot e{-6}$	$4 \cdot e{-6}$
B	1	$2 \cdot e{-5}$	-0.041	-0.35	$2 \cdot e{-6}$	$2 \cdot e{-5}$	$3 \cdot e{-5}$
C	2.083	0.035	$-2 \cdot e{-4}$	-0.42	$1 \cdot e{-4}$	$2 \cdot e{-6}$	$1 \cdot e{-4}$
D	2.37	0.2	$6.7 \cdot e{-5}$	-0.56	$5 \cdot e{-4}$	$1 \cdot e{-6}$	$6 \cdot e{-4}$

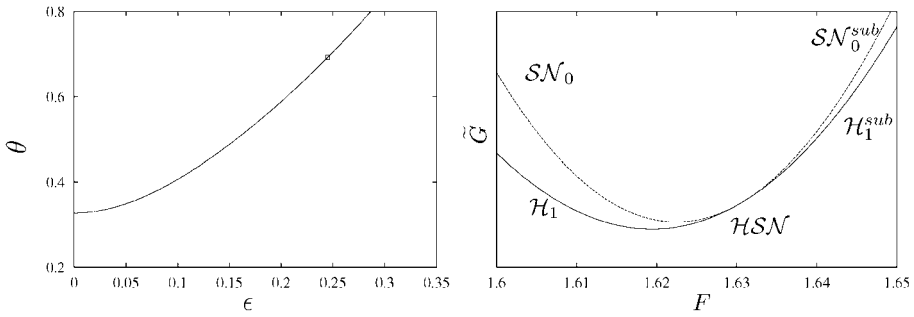

Figure 56. Left: argument θ of the complex conjugate eigenvalues of $D\mathcal{P}$ on the fixed points belonging to the curve of $\mathcal{HSN}$ points, in the parameter space $\mathfrak{M} = \{F, G, \epsilon\}$. Right: local bifurcation diagram of $\mathcal{P}$ close to the point $\mathcal{HSN}$ at $\epsilon = 0.245$ (plotted at the left with a small box), inside the plane $\mathfrak{M}_{0.245} = \{\epsilon = 0.245\}$. The graph has been affinely transformed by plotting $\tilde{G} = G - 1.36 \times (F - 1.5)$. The vertical width is 2×10^{-4}.

in the creation of the quasi-periodic attractor $\mathbb{Q}_1$ from the period-two curve $4\mathbb{C}_1$ (figure 7). Indeed, by the analogies between $\mathbb{Q}_1$ and $\mathbb{U}$ we call the latter a quasi-periodic Hénon-like repellor.

Seemingly, for all (F, G) the torus repellor $\mathbb{T}$ is destroyed long before ϵ reaches 0.5. As a consequence, the frayed boundary $\mathcal{QH}_{\text{sub}}$ may possibly persist only for small values of ϵ. Furthermore, the torus repellor is the boundary between the basins of two different attractors, the circle $\mathbb{C}_1$ and the point $\mathbb{A}$. Probably, the strange repellors born at the destruction of $\mathbb{T}$ still are basin boundaries, although of fractal dimension. However, for some values of (F, G) inside $\mathfrak{M}_{0.5}$, both the circle attractor $\mathbb{C}_1$ and the torus have disappeared (section 4.5), and the fixed point attractor $\mathbb{A}$ is the unique invariant object. This might be due to the fact that the basin of $\mathbb{A}$ swallows the other.

We return to the disappearence of the $\mathcal{HSN}$ between $\epsilon = 0$ and $\epsilon = 0.5$. It is possible to continue the codimension two point $\mathcal{HSN}$ as a function of ϵ. In figure 56 a plot of the evolution of the (positive) argument of an eigenvalue of modulus 1 is displayed. The same figure shows also the Hopf and saddle-node bifurcation curves, tangent to each other at the $\mathcal{HSN}$ point, for $\epsilon = 0.245$. The curves are rather close for this value of ϵ. Guided by these results, we see that a codimension three bifurcation takes place between $\epsilon = 0.277$ and $\epsilon = 0.5$. A better understanding of this is object of further investigation.

5.2. Bifurcations of codimension two and higher

The disappearance of the torus repellors implies that the frayed curve of quasi-periodic Hopf bifurcations $\mathcal{QH}_{\text{sub}}$ is destroyed by some higher codimension bifurcation. Strong resonances could take place on $\mathcal{QH}_{\text{sub}}$, similarly to what occurs for the Hopf curves $\mathcal{H}_1$ and $\mathcal{H}_2$ (section 4.3). In fact, several strong resonance points were found there at $\epsilon = 0.5$ (sections 4.2 and 4.1). These points occur in couples delimiting gaps in the Hopf curves. The first open question is to determine the bifurcation diagram close to these strong resonance

points and the implications for the breakdown of circles and tori. Although no strange attractors were found in the neighbourhood of the strong resonances, the theory prescribes their occurrence, perhaps confined in exponentially small regions in the parameter plane (cf [13, 14, 59]).

Secondly, the two endpoints of such resonance gaps merge into one degenerate strong resonance at $\epsilon = 0$ (since no gaps occur on the Hopf curves). From this degenerate point, two curves of strong resonance points come out in the parameter space $\mathfrak{M} = \{F, G, \epsilon\}$; bounding, at each ϵ fixed, a gap on a Hopf curve contained inside parameter plane $\mathfrak{M}_\epsilon$. Then, how do these curves of Bogdanov–Takens bifurcations evolve inside $\mathfrak{M}$?

This discussion leads naturally to take codimension three bifurcations into account. Such phenomena can only be individuated by using three control parameters in system (2). We have proved the occurrence of a Hopf-saddle-node bifurcation of higher codimension inside the parameter space $\mathfrak{M} = \{F, G, \epsilon\}$; section 4.3. This follows indeed by a continuity argument: at $\epsilon = 0.277$ there is a Hopf saddle node point (see figure 15), while at $\epsilon = 0.5$ it has disappeared. A bifurcation causing $\mathcal{HSN}$ to disappear could be a codimension three Hopf-saddle-node strong resonance, where the three eigenvalues of $\mathcal{P}$ are $\mu_1 = 1, \mu_2 = \exp(2\pi \mathrm{i} p/q)$ and $\mu_2 = \exp(-2\pi \mathrm{i} p/q)$, with $q = 1, \ldots, 4$.

All the previous questions can be dealt with from an experimental point of view, namely by studying the driven Lorenz-84 model in deeper detail. This requires careful numerical tools, due to the large period and to the tiny size of the domains where some phenomena occur. Furthermore, some of the codimension two and three bifurcations found in the model, like the codimension two and the degenerate Hopf-saddle-node, have yet to be studied even from a theoretical viewpoint. For this it is of help to construct of suitable local model maps. This will be object of future research.

5.3. Global bifurcations and model maps

Beyond the questions discussed in the previous section, some global bifurcations taking place in the Lorenz-84 system have to be better understood, like the three-dimensional Shil'nikov homoclinic tangency of a saddle focus fixed point. Evidence for the occurrence of such bifurcations was presented in section 4.4, but the relationship with the creation of Shil'nikov-like attractors (sections 4.10 and 5.1.2) is not yet clear. This could be investigated by constructing appropriate model maps.

Model maps could also be used to investigate the creation of quasi-periodic Hénon-like attractors (section 4.9.3) and repellors (section 5.1.3). In particular, one might also consider cascades of quasi-periodic period doublings of invariant circles. Research is in progress in these directions.

Appendix A. On the numerical methods

Appendix A.1. Integration and continuation

The numerical computation of the trajectories of system (2) is performed using a Taylor expansion of the solutions around time t (cf [15]). We use the polynomial approximation

$$(x(t+h), y(t+h), z(t+h)) \simeq \sum_{k=0}^{N} (x_k(t), y_k(t), z_k(t)) h^k,$$

where

$$x_k(t) = \frac{1}{k!}\frac{\mathrm{d}^k}{\mathrm{d}t^k}x(t), \qquad y_k(t) = \frac{1}{k!}\frac{\mathrm{d}^k}{\mathrm{d}t^k}y(t), \qquad z_k(t) = \frac{1}{k!}\frac{\mathrm{d}^k}{\mathrm{d}t^k}z(t). \tag{15}$$

Given an initial point (x_0, y_0, z_0), the coefficients (15) for $k \geqslant 1$ are computed recursively using the Leibnitz rule. One has, for example,

$$\frac{\mathrm{d}^k}{\mathrm{d}t^k} y^2 = \sum_{m=0}^{k} \frac{k!}{m!(k-m)!} \mathrm{d}^m y \mathrm{d}^{k-m} y = k! \sum_{m=0}^{k} y_m y_{k-m}$$

For $k \geqslant 1$, substituting expressions like above in (2), one gets

$$x_{k+1} = \frac{(-ax_k - \sum_{m=0}^{k}(y_m y_{k-m} + z_m z_{k-m}) + aF\epsilon c_k)}{k+1},$$

$$y_{k+1} = \frac{(-y_k + \sum_{j=0}^{k}(x_j y_{k-j} - bx_j z_{k-j}) + G\epsilon s_k)}{k+1},$$

$$z_{k+1} = \frac{(-z_k + \sum_{j=0}^{k}(bx_j y_{k-j} + x_j z_{k-j}))}{k+1},$$

where $c_k(t) = (1/k!)\mathrm{d}^k/\mathrm{d}t^k \cos(\omega t)$ and $s_k(t) = (1/k!)\mathrm{d}^k/\mathrm{d}t^k \sin(\omega t)$. We usually fixed the order of the Taylor polynomial to $N = 24$, since this showed good convergence in the testing. On the other hand, a variable step size option is adopted. After computing all coefficients (x_k, y_k, z_k), the step size h is determined by

$$h = \min\left\{ \left(\frac{\eta}{a_N}\right)^{1/N}, \left(\frac{\eta}{a_{N-1}}\right)^{1/(N-1)} \right\},$$

where $a_k = \max(|x_k|, |y_k|, |z_k|)$ and $\eta = 10^{-16}$. The first variational equations of system (2) are handled in a similar way. For a specific treatment of the Taylor method, see [37].

We briefly describe the method used to compute curves of (bifurcations of) fixed points, based on [57]. For other strategies, see [40, 54]. For many other related problems, like continuation of cusp points or homoclinic tangencies, see [16]. Let (x_0, y_0, z_0) be a fixed point of $\mathcal{P}$ at parameter values F_0, G_0, ϵ_0 and suppose F_0 and ϵ_0 are kept fixed. It is convenient to consider G as a fourth variable. We look for zeroes of the function $\mathcal{H}$, defined by

$$\mathcal{H} : \mathbb{R}^4 \times I \to \mathbb{R}^3, \quad \mathcal{H}(q, G) \stackrel{\text{def}}{=} \mathcal{P}(q) - q, \qquad q = (x, y, z), \tag{16}$$

knowing that $q_0 = (x_0, y_0, z_0)$ is a solution for $G = G_0$. Under the condition that the derivative $\mathcal{D}_{q,G}\mathcal{H} = \mathcal{D}_{q,G}\mathcal{P} - I$ has maximal rank, the implicit function theorem guarantees the existence of a curve $\alpha(s) \in \mathbb{R}^4$ of solutions of passing through (q_0, G_0). A point $(\tilde{q}_1, \tilde{G}_1)$ on $\alpha(s)$ is predicted using interpolation and used as initial seed for a Newton corrector. The point (q_1, G_1) obtained after this refinement lies on the curve $q(s)$.

There exist procedures to do continuation of invariant circles. Some are based on the continuation of the Fourier coefficients [22], other on a derivation of the graph transform [12] and on fixed points of a synthesized return map using non-integer powers of a map [58].

Appendix A.2. Estimates of Lyapunov exponents

The Lyapunov exponents are estimated according to the algorithm described by Galgani *et al* [7]. The first variational equations of system (2) are integrated during a period T, with the identity matrix as initial condition. The canonical orthonormal basis is thereby mapped onto a new set of vectors $(\boldsymbol{v}_1^1, \boldsymbol{v}_2^1, \boldsymbol{v}_3^1)$. Each vector tends to align itself along the direction of maximal expansion (or of minimal compression). Thus all $\boldsymbol{v}_1^1$, $\boldsymbol{v}_2^1$, and $\boldsymbol{v}_3^1$ tend to collapse onto one direction. To prevent this, the Gramm–Schmidt process is applied to $(\boldsymbol{v}_1^1, \boldsymbol{v}_2^1, \boldsymbol{v}_3^1)$ after a few steps of the numerical integrator, yielding a set $(\tilde{\boldsymbol{v}}_1^1, \tilde{\boldsymbol{v}}_2^1, \tilde{\boldsymbol{v}}_3^1)$ of orthogonal vectors. Define $\boldsymbol{w}_j^1 = \tilde{\boldsymbol{v}}_j^1 / \|\boldsymbol{v}_j^1\|$ for $j = 1, 2, 3$. Then a new frame of vectors $(\boldsymbol{v}_1^2, \boldsymbol{v}_2^2, \boldsymbol{v}_3^2)$ is computed

by integrating the first variational equations taking as initial condition the orthonormal vectors $(\boldsymbol{w}_1^1, \boldsymbol{w}_2^1, \boldsymbol{w}_3^1)$ from the previous step. At iteration step k, define

$$c_j^k = \prod_{i=1}^{k} \|\tilde{\boldsymbol{v}}_j^k\| \quad \text{and} \quad \boldsymbol{w}_j^k = \frac{\tilde{\boldsymbol{v}}_j^k}{\|\tilde{\boldsymbol{v}}_j^k\|} \qquad \text{for } j = 1, 2, 3.$$

The orthonormalization process does not change the direction of $\boldsymbol{v}_1^k$, so that $\boldsymbol{w}_1^k$ still points to the direction of maximal stretch. Denoting by λ_1, λ_2, and λ_3 the Lyapunov exponents, in decreasing order, the length c_1^k of $\boldsymbol{v}_1^k$ is approximately proportional to $\mathrm{e}^{k\lambda_1}$. The plane spanned by $\boldsymbol{v}_1^k$ and $\boldsymbol{v}_2^k$ is not changed by the Gramm–Schmidt process and tends to adjust to the subspace of maximal growth of surfaces. The rate of growth of areas is proportional to $\mathrm{e}^{k(\lambda_1+\lambda_2)}$. In particular, since $\boldsymbol{v}_1^k = \boldsymbol{w}_1^k$ and $\boldsymbol{w}_2^k$ are orthonormal, the length of the projection of $\boldsymbol{v}_2^k$ upon $\boldsymbol{w}_2^k$ is proportional to $\mathrm{e}^{k\lambda_2}$. A similar argument for growth of volumes yields that c_j^k is proportional to $\mathrm{e}^{k\lambda_j}$. Therefore, the Lyapunov exponent λ_j is estimated by the averages

$$\lambda_j \approx \frac{1}{k} \log(c_j^k), \qquad \text{with } k = 1, 2, \ldots, N. \tag{17}$$

For the computation of the Lyapunov spectrum of a single attractor, a total of $N = 10^5$ iterates of $D\mathcal{P}$ is carried out. After a transient of 10^4 iterations, only the maxima of c_j^k over consecutive blocks of 100 iterations of $D\mathcal{P}$ are used. This idea goes back to [15]. After computing a number of blocks, say 150, we compute the average of the c_j^k as in (17). Then a new set of 50 blocks is computed and the c_j^k are averaged over the last 150 blocks. The maximum of the differences between the last three averages is used as an estimation for the error in the Lyapunov exponent. Results of a test with 10^5 iterates of $D\mathcal{P}$ are shown in figure 57(*a*). The solid line joins the maxima of c_1^k on blocks of 100 iterates. The small black boxes are the estimates obtained by averaging over 150 blocks.

Because of the high computational cost of integrating variational equations for a long period $T = 73$, when scanning for Lyapunov exponents for several parameter values (like in figures 12(*b*)–(*d*)), a quicker procedure has been adopted. For each parameter value, 10^4 iterates of $D\mathcal{P}$ are in total computed (sometimes 2×10^4), preceded by a transient of 500 iterates of $\mathcal{P}$. When detecting a periodic point $\mathbb{D}$, the iteration is stopped and the Lyapunov spectrum is at once computed from the eigenvalues of $\mathbb{D}$. The last 1000 approximations obtained by (17) are averaged. This provides the desired estimate.

For more precise methods of estimation of the Lyapunov exponents, see [24].

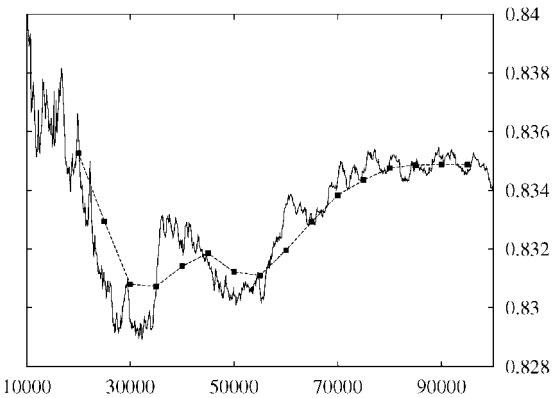

Figure 57. (*a*) Test on the computation of Lyapunov exponents, for $F = 5$ and $G = 1.29$. See text for explanation.

Appendix A.3. Power spectrum estimation

For the technical terminology and the definitions of several concepts used in this section, we refer the reader to [9, 51]. The power spectra are estimated by using the discrete fourier transform (DFT). Given an array $\boldsymbol{c}$ of complex values (called time series [17]) its DFT is the array:

$$\hat{\boldsymbol{c}} = (\hat{c}_0, \hat{c}_1, \ldots, \hat{c}_{N-1}), \qquad \text{where} \quad \hat{c}_k \stackrel{\text{def}}{=} \frac{1}{N} \sum_{n=0}^{N-1} c_n \exp\left(-2\pi \mathrm{i} \frac{nk}{N}\right). \tag{18}$$

In practice, the DFT of an array is computed using a fast fourier transform (FFT) algorithm. The power spectrum is a plot of the square moduli of the coefficients c_k against so-called Fourier frequency $f_k = k/N$.

Given a $\mathcal{P}$-invariant set $\mathbb{W}$, a (real) time series is constructed in the following way. An orbit of $\mathcal{P}$ with N points on $\mathbb{W}$ is first determined by iteration. We mostly fix $N = 2^{16}$ and compute N points q_k starting from $q_0 \in \mathbb{W}$, where $q_k = \mathcal{P}(q_{k-1}) \in \mathbb{R}^3$. To produce a time series, this orbit has to be 'measured' by means of an observable $\Omega : \mathbb{R}^3 \to \mathbb{R}$ (cf [17]). In most cases, we chose Ω as the projection onto the coordinate y, yielding the time series $\boldsymbol{y} = (y_0, \ldots, y_{N-1})$, with $y_k = \Omega(q_k)$. Then an estimate of the power spectrum of $\mathbb{W}$ is obtained by plotting the square modulus $|\hat{y}_k|^2$ against the Fourier frequency f_k, for $k = 0, \ldots, N/2$. If the attractor $\mathbb{W}$ is an invariant curve, the fundamental frequency is the rotation number modulo $1/2$. In the case of the circle $\mathbb{C}_1$ (figures 45(a) and (b)) the fundamental frequency is close to the Fourier frequency with the highest peak. For $2\mathbb{C}_1$, one has to take a Fourier frequency corresponding to one half of that with the highest peak. Pictures such as figure 36 left are produced by computing power spectra on circle attractors, usually with a low number of iterates, e.g. 4096 points. A few comments of technical nature have to be added.

Remarks

1. Each power spectrum is computed from a single time series inside $\mathbb{W}$. Another possibility is to compute a number m time series' in $\mathbb{W}$—all with the same length N and with distinct initial points—and then to average the m spectra (cf [1]).
2. Before computing a power spectrum, the array $\boldsymbol{y}$ is brought to zero average. Furthermore, a Hanning windowing of order two is applied in order to reduce frequency leakage. In particular, we first apply the translation

$$\boldsymbol{y} \mapsto \boldsymbol{u} = (u_0, \ldots, u_{N-1}), \qquad \text{with } u_j = y_j - \frac{1}{N} \sum_{k=0}^{N-1} y_k.$$

   FFT is performed on a second array $\boldsymbol{v}$, defined by

$$v_k = H_2^k \, u_k, \qquad \text{where } H_2^k = \frac{2}{3} \cos\left(1 - 2\pi \frac{k}{N}\right)^2$$

   (Hanning windowing, see again [9, 51]). After that, the resulting coefficients, denoted again by $\hat{y}_k$ for simplicity, are normalized by dividing for the norm of the array $\boldsymbol{H} = (H_2^0, \ldots, H_2^{N-1})$.
3. We note that frequencies are computed modulo 1, since all frequencies lying outside the interval $[0, 1)$ are shifted inside this interval. This phenomenon, called aliasing, is unavoidable when dealing with discrete time evolutions. Indeed, since no sampling of a continuous time evolution is performed, the Nyquist frequency is always fixed at $1/2$.

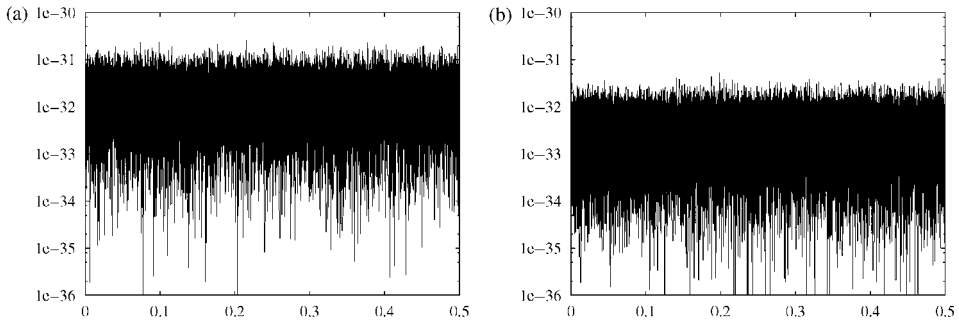

Figure 58. (*a*), (*b*) Tests on the propagation of errors in the DFT algorithm. See text for explanation.

The frequency range is further restricted to $[0, 1/2]$, since the power spectrum of a real sequence $\boldsymbol{r}$ is symmetric with respect to $1/2$. One indeed has $\hat{r}_{N-k} = \bar{\hat{r}}_k$, since

$$\hat{r}_{N-k} = \frac{1}{N}\sum_{n=0}^{N-1} r_n \exp\left(-2\pi \mathrm{i}\frac{(N-k)n}{N}\right) = \frac{1}{N}\sum_{n=0}^{N-1} r_n \exp\left(2\pi \mathrm{i}\frac{kn}{N}\right).$$

The last remark provides motivation to introduce the following notation:

$$f \operatorname{mir}\tfrac{1}{2} \stackrel{\text{def}}{=} 1 - (f \bmod 1) = (-f) \bmod 1.$$

For example, $0.28 \operatorname{mir}\frac{1}{2} = 0.72$ and $1.91 \operatorname{mir}\frac{1}{2} = 0.09$. Given the above symmetry, the power spectrum has the same value at f and at $f \operatorname{mir}\frac{1}{2}$.

A simple test has been performed to estimate the propagation of random errors in the FFT algorithm. Given a time series $\boldsymbol{a}$, a 'random' perturbation $\boldsymbol{b}$ is prepared as follows. We generate a sequence of random numbers r_k with uniform probability distribution in $[0, 1]$ and define $b_k = m_k y_k$, where

$$m_k = \begin{cases} 1 - 10^{-14} & \text{if } r_k < 0.5, \\ 1 + 10^{-14} & \text{otherwise.} \end{cases}$$

The DFTs $\hat{\boldsymbol{a}}$ and $\hat{\boldsymbol{b}}$ are computed and the second is subtracted from the first, yielding an array $\boldsymbol{c}$. The square moduli of the coefficients c_k are plotted against k/N. For the two tests in figures 58(*a*) and (*b*), an orbit on the circle attractor in figure 7(*B*) respectively on the SA in figure 10 have been used. The size of the sample has been kept to $N = 2^{16}$. In the first case, the propagated error $|c_k|^2$ varies between order 10^{-35} and 10^{-31}. Therefore, we have that $0.001 \lessapprox |c_k|/10^{-14} \lessapprox 0.1$, and the same holds for the second case. Since the size of the sample is of order 1, we conclude that the random error propagates to the amplitudes divided by a factor ranging between 0.1 and 0.001.

Remark A.1. The power spectrum is often used as an estimator of the spectral density of a stationary stochastic process. Given a stationary, zero-average, discrete time stochastic process $\{X_n\}_{n\in\mathbb{Z}}$ on a probability space (Ω, ν), the autocorrelation function is defined by

$$\gamma_X : \mathbb{Z} \to \mathbb{C}, \qquad \gamma_X(n) = E[X_n X_0],$$

where E denotes the expected value with respect to ν. A white noise stochastic process is characterized by $\gamma_X(n) = 0$ except at $n = 0$, where $\gamma_X(0)$=1. Furthermore, the spectral density [17] is constant.

Consider a $\mathcal{P}$-attractor $\mathbb{W} \subset \mathbb{R}^3$ and suppose that it has a unique Sinai–Ruelle–Bowen measure[27] ν. This allows us to define a process $\{X_n\}_{n\in\mathbb{Z}}$ on the probability space $(\mathbb{W}, \nu)$, where

[27] In fact, this is a rather strong assumption, (see, e.g. [66]).

$X_n = Y \circ \mathcal{P}^n$ is the nth iterate of $\mathcal{P}$ on $\mathbb{W}$, measured by the observable $Y : \mathbb{W} \to \mathbb{R}$. Then power spectra like in figure 9(A) indicate a practically constant spectral density. This implies that the random variables X_n and X_m are uncorrelated when $m \neq n$.

Acknowledgments

The authors thank B L J Braaksma, Alejandra González, Ángel Jorba, Franz Naselli, Andrey Shil'nikov and Floris Takens for helpful discussions and Josep Maria Mondelo for technical help concerning frequency analysis. They also thank Lennaert van Veen and Ferdinand Verhulst for the links with the meteorological literature. The authors are indebted to each other's institution for hospitality. The research of the second author has been partially supported by grants BFM2000-805 (Spain), 2000SGR-27 and 2001SGR-70 (Catalonia) and INTAS00-221. The third author acknowledges support from Socrates grant IC29015.

References

[1] Anishchenko V S 1995 *Dynamical Chaos—Models and Experiments* (Singapore: World Scientific)
[2] Anishchenko V S, Safonova M A, Feudel U and Kurths J 1994 Bifurcations and transition to chaos through three-dimensional tori *Int. J. Bifur. Chaos* **4** 595–607
[3] Arnol'd V I 1965 Small denominators, I: Mappings of the circumference into itself *AMS Transl. Ser. 2* **46** 213–84
[4] Arnol'd V I 1980 *Mathematical Methods of Classical Mechanics* (Berlin: Springer)
[5] Arnol'd V I 1983 *Geometrical Methods in the Theory of Ordinary Differential Equations* (Berlin: Springer)
[6] Benedicks M and Carleson L 1991 The dynamics of the Hénon map *Ann. Math.* **133** 73–169
[7] Benettin G, Galgani L, Giorgilli A and Strelcyn J-M 1980 Lyapunov characteristic exponents for smooth dynamical systems: a method for computing all of them *Meccanica* **15** 9
[8] Bosch M and Simó C 1993 Attractors in a Shil'nikov–Hopf scenario and a related one-dimensional map *Physica* D **62** 217–29
[9] Briggs W L and Henson V E *The DFT: An Owner's Manual for the Discrete Fourier Transform* (Philadelphia: SIAM)
[10] Broer H W, Huitema G B and Sevryuk M B 1996 Quasi-periodic motions in families of dynamical systems *Springer LNM* **1645**
[11] Broer H W, Huitema G B, Takens F and Braaksma B L J 1990 Unfoldings and bifurcations of quasi-periodic tori *Mem. AMS* **83** 421
[12] Broer H W, Osinga H M and Vegter G 1997 Algorithms for computing normally hyperbolic invariant manifolds *Z. Angew. Math. Phys.* **48** 480–524
[13] Broer H W and Roussarie R 2001 Exponential confinement of chaos in the bifurcation sets of real analytic diffeomorphisms *Global Analysis of Dynamical Systems, Festschrift dedicated to Floris Takens for his 60th birthday* ed H W Broer, B Krauskopf and G Vegter (Bristol: Institute of Physics Publishing)
[14] Broer H W, Roussarie R and Simó C 1996 Invariant circles in the Bogdanov–Takens bifurcation for diffeomorphisms *ETDS* **16** 1147–72
[15] Broer H W and Simó C 1998 Hill's equation with quasi-periodic forcing: resonance tongues, instability pockets and global phenomena *Bol. Soc. Bras. Mat.* **29** 253–93
[16] Broer H W, Simó C and Tatjer J C 1998 Towards global models near homoclinic tangencies of dissipative diffeomorphisms *Nonlinearity* **11** 667–770
[17] Broer H W and Takens F 1993 Mixed spectrum and rotational symmetry *Archive Rat. Mech. An.* **124** 13–42
[18] Broer H W and Takens F 1989 Formally symmetric normal forms and genericity *Dynamics Reported* **2** 36–60
[19] Broer H W and Vegter G 1984 Subordinate Shil'nikov bifurcations near some singularities of vector fields having low codimension *ETDS* **4** 509–25
[20] Broer H W and Vegter G 1992 Bifurcational aspects of parametric resonance *Dynamics Reported* **1** 1–53
[21] Carcassès J P, Mira C, Bosch M, Simó C and Tatjer J C 1991 'Crossroad area–spring area' transition (II) Parameter plane representation *Int. J. Bifur. Chaos Appl. Sci. Eng.* **1** 183–96
[22] Castellà E and Jorba À 2000 On the vertical families of two-dimensional tori near the triangular points of the Bicircular problem *Celestial Mechanics* **76** 35–54
[23] Chow S N and Hale J K 1982 *Methods of Bifurcation Theory* (Berlin: Springer)

[24] Cincotta P M and Simó C 2000 Simple tools to study global dynamics in non-axisymmetric galactic potentials-I. *Astron. Astrophys. Supp.* **147** 205–28
[25] Devaney R L 1989 *An Introduction to Chaotic Dynamical Systems* 2nd edn (Reading, MA: Addison–Wesley)
[26] Díaz L, Rocha J and Viana M 1996 Strange attractors in saddle cycles: prevalence and globality *Inv. Math.* **125** 37–74
[27] Eckmann J-P and Ruelle D 1985 Ergodic theory of chaos and strange attractors *Rev. Mod. Phys.* **57** 617–55
[28] Feigenbaum M 1978 Qualitative universality for a class of nonlinear transformations *J. Stat. Phys.* **21** 25–52
[29] Flatto M and Levinson N 1955 Periodic solutions of singularly perturbed systems *J. Rat. Mech. Anal.* **4** 943–50
[30] Gomez G, Mondelo J M and Simó C 2001 Refined Fourier analysis procedures *UB Preprint*
[31] Gonchenko S V, Shil'nikov L P and Turaev D V 1996 Dynamical phenomena in systems with structurally unstable Poincaré homoclinic orbits *Chaos* **6** 15–31
[32] Grassberger P and Procaccia I 1983 Measuring the strangeness of strange attractors *Physica* D **9** 189–208
[33] Grebogi C, Ott E and Yorke J 1982 Chaotic attractors in crisis *Phys. Rev. Lett.* **48** 1507–10
[34] Guckenheimer J and Holmes P 1983 *Nonlinear Oscillations, Dynamical Systems, and Bifurcations of Vector Fields* (New York: Springer)
[35] Hirsch M W, Pugh C C and Shub M 1977 Invariant manifolds *Springer LNM* **583**
[36] Homan K 1998 Routes to chaos in the Lorenz-84 atmospheric model *Masters Thesis* Department of Mathematics, University of Groningen
[37] Jorba À and Zou M 2001 On the numerical integration of ODE by means of high-order Taylor methods *Preprint*
[38] Kaplan J and Yorke J 1979 Chaotic behaviour of multidimensional difference equations *Functional Differential Equations and Approximations of Fixed Points, Springer LNM* 204–27
[39] Kock R 1998 Routes to chaos in the periodically driven Lorenz-84 system *Masters Thesis* Department of mathematics, University of Groningen
[40] Kuznetsov Y 1995 *Elements of Applied Bifurcation Theory* (New York: Springer)
[41] Lorenz E N 1984 Irregularity: a fundamental property of the atmosphere *Tellus* **36A** 98–110
[42] Lorenz E N 1990 Can chaos and intransitivity lead to interannual variability? *Tellus* **42A** 378–89
[43] Masoller C, Sicardi Schifino A C and Romanelli L 1992 Regular and chaotic behaviour in the new Lorenz system *Phys. Lett.* A **167** 185–90
[44] Mora L and Viana M 1993 Abundance of strange attractors *Acta Math.* **171** 1–71
[45] Newhouse S 1974 Diffeomorphisms with infinitely many sinks *Topology* **13** 9–18
[46] Newhouse S, Ruelle D and Takens F 1978 Occurrence of strange Axiom A attractors near quasiperiodic flows on $\mathbb{T}^m$, $m \geqslant 3$ *Commun. Math. Phys.* **64** 35–40
[47] Östlund S, Rand D, Sethna J and Siggia E 1983 Universal properties of the transition from quasiperiodicity to chaos in dissipative systems *Physica* D **8** 303–42
[48] Palis J and Takens F 1993 Hyperbolicity and sensitive chaotic dynamics at homoclinic bifurcations *Cambridge Studies in Advanced Mathematics* vol 35 (Cambridge: Cambridge University Press)
[49] Palis J and Viana M 1994 High dimension diffeomorphisms displaying infinitely many sinks *Ann. Math.* **140** 91–136
[50] Pomeau Y and Manneville P 1980 Intermittent transition to turbulence in dissipative dynamical systems *Commun. Math. Phys.* **74** 189–97
[51] Press W, Teukolsky S, Vetterling W and Flannery B 1992 *Numerical Recipies in C: the Art of Scientific Computing* 2nd edn (New York: Cambridge University Press)
[52] Ruelle D 1988 *Elements of Differentiable Dynamics and Bifurcation Theory* (New York: Academic)
[53] Ruelle D and Takens F 1971 On the nature of turbulence *Comm. Math. Phys.* **20** 167–92
[54] Seydel R 1994 *Practical Bifurcation and Stability Analysis* (New York: Springer)
[55] Shil'nikov A, Nicolis G and Nicolis C 1995 Bifurcation and predictability analysis of a low-order atmospheric circulation model *Int. J. Bifur. Chaos* **5** 1701–11
[56] Simó C 1979 On the Hénon–Pomeau attractor *J. Stat. Phys.* **21** 465–94
[57] Simó C 1990 On the analytical and numerical computation of invariant manifolds *Modern Methods in Celestial Mechanics* ed D Benest and C Froeschlé (Paris: Frontières) pp 285–330
[58] Simó C 1996 Effective Computations in Hamiltonian Dynamics *Cent ans après les Méthodes Nouvelles de H. Poincaré* (Frarvi Société Mathématique de) pp 1–23
[59] Simó C, Broer H and Roussarie R 1991 A numerical exploration of the Takens-Bogdanov bifurcation for diffeomorphisms *Eur. Conf. Iteration Theory (ECIT 89)* (Batschuns, Austria) ed C Mira, N Netzer, C Simó and G Targonski (Singapore: World Scientific) pp 320–34
[60] Simó C and Tatjer J C 1994 Basins of attraction near homoclinic tangencies *ETDS* **14** 351–90
[61] Swinney H L and Gollub J P 1986 Characterization of hydrodynamic strange attractors *Physica* D **18** 448–54

[62] Tatjer J C 2001 Three dimensional dissipative diffeomorphisms with homoclinic tangencies *ETDS* **21** 249–302
[63] van Veen L, Opsteegh T and Verhulst F The dynamics of a low order coupled ocean-atmosphere model *J. Nonlin. Sci.* submitted
van Veen L, Opsteegh T and Verhulst F *Preprint* arXiv:chao-dyn/9812024
[64] Viana M 1993 Strange attractors in higher dimensions *Bull. Braz. Math. Soc.* **24** 13–62
[65] Viana M 1997 Multidimensional nonhyperbolic attractors *Inst. Hautes Études Sci. Publ. Math.* **85** 63–96
[66] Viana M 1997 Stochastic dynamics of deterministic systems *Braz. Math. Colloquium (IMPA)*
Viana M 1997 *Preprint* http://www.impa.br/∼viana/
[67] Wieckzorek S, Krauskopf B and Lenstra D 2002 Mechanisms for multistability in a semiconductor laser with optical injection *Opt. Commun.* **183** 215–26
[68] Yorke J and Alligood K 1983 Cascades of period-doubling bifurcations: a prerequisite for horseshoes *Bull. AMS* **9** 319–22